Politecnico di Milano
Department of Civil, Environmental and Land Management Engineering

Master of Science in Civil Engineering for Risk Mitigation

"Extrusion Tests on Triaxial Specimens: Numerical Investigation and Theoretical Interpretation"

A thesis by:
ing. Budiwan Adi Tirta

Supervisor:
Prof. ing. Claudio Giulio di Prisco
Co-supervisor:
ing. Luca Flessati

Academic Year:
2014/2015

Supervisor:

Prof.ing. Claudio Giulio di Prisco
(DICA Politecnico di Milano)

Co-supervisor:

ing. Luca Flessati
(DICA Politecnico di Milano)

Author:

ing. Budiwan Adi Tirta

Permanent Address: Jalan Kucica block JF/XII no.9
Bintaro sector 9, Tanggerang, Indonesia
E-Mail: budi_adi_tirta@yahoo.com

Acknowledgements

In the name of God, most Gracious, most Compassionate.

Lecco, September 2015

Ing. Budiwan Adi Tirta

"I produced my theories and made my experiments for the purpose of establishing an aid in forming a correct opinion and I realized with dismay that they are still considered by the majority as a substitute for common sense and experience." (Terzaghi, 1957)

Abstract

Tunnelling has become a preferred construction as urbanization increases and available land decreases in all over the world. One method that is commonly used in tunneling is so called conventional tunnel method (CTM); despite tunnel boring machines are becoming more popular. One of the main consideration concerning construction of tunnel is the stability of tunnel face during excavation. Scientist and engineer depend on physical modelling to understand different phenomena such as deformation patterns and failure mechanism. Since full-scale physical model is expensive and hard to repeat, it is preferable to use reduced model. There are three categories of reduced physical model: centrifuge, 1-g scale and extrusion tests. The main aim of the present research is to study stability of the deep underground opening of CTM by adapting results of extrusion tests which are obtained numerically thanks to the use of the commercial code Midas GTS NX 2014. The study focuses on rocks or soils whose viscous effect are negligible and behave under undrained condition. Static analyses using an elasto-plastic Tresca constitutive model with axisymmetric model are used to obtain relationship between stresses and displacements or characteristic curve and the development of platic zone surrounding the face. Interpretation of the results is done by considering real behaviour of phenomena which are three-dimensional problems. Therefore, the results have been always compared with those of a 3D tunnel as a reference model.

Although the past experiments on extrusion furnished a guide that is sufficiently reliable for qualitative predictions of the phenomena, however, problems that are typical of studies performed in the laboratory do exists. One of the problems associates with an effect of small scale due to geometry. This leads us to investigate any possible effect on boundaries in extrusion tests considering different specimen dimensions. The study indicates that the numerical results of extrusion tests show a strong dependency of the geometry of specimen and the ratio between initial stress and shear strength. For instance, the results reveal that the effect of small scale is less significant when the ratio between the initial stress and the undrained shear strength is equal or lower than 8.5, and is applied in the standard triaxial specimens whose ratio between diameter of extrusion and specimen is 5.4.

Another problem of extrusion tests is difficulty in reproducing *in situ* conditions: distribution of initial stresses and boundary conditions. As consequence, the results give different outcomes with respect to those of the 3D tunnel. The major concern is the evidence of stress evolution stresses in the boundaries close to the face during excavation or reduction of the face pressure. The reduction of stresses in one of the boundaries is evidence in the extrusion tests. In the other hand, the stress evolution is negligible in all the boundaries in the 3D tunnel. This reduction causes, therefore, reduction in destabilizing loads and, hence, reduction of displacement at the face. This is the main reason why the characteristic curve produced by the model extrusion tests is more stable than that of the 3D tunnel.

The present study implies also some conclusions that are valid for both models. (i) Pincers effect occurs and is quantified as the stress migrates around the face. (ii) By means of a suitable dimensionless plane, all of the numerical results are collapse into a unique curve (so called front mother curve (FMC)) even though the soil parameters are varied. (iii) Although, the FMC of the extrusion tests is different than that of obtained by the 3D tunnel (due to different boundary conditions), both models give similar responses.

Keywords: Extrusion tests; Deep tunnel; clays; Finite-Element Modeling (FEM); 2D-axisymmetric; Elasticity and plasticity.

Sommario

La costruzione di opere sotterranee sta acquisendo una sempre maggiore diffusione per via della sempre crescente urbanizzazione ed occupazione del suolo. Nonostante la sempre crescente popolarità dello scavo meccanizzato, lo scavo in tradizionale è ad oggi ancora molto utilizzato. Un aspetto importante nello scavo di gallerie è l'aspetto della stabilità del cavo. Per valutare il comportamento del sistema, prestando particolare attenzione allo sviluppo di deformazioni e di meccanismi di rottura, la ricerca ha fatto uso di modellazione fisica, in piccola scala: in particolare è possibile eseguire prove in centrifuga, prove a 1g o utilizzare prove di estrusione. Lo scopo principale del presente elaborato è studiare la stabilità di scavi di gallerie profonde adattando i risultati di analisi numeriche, eseguite mediante il codice di calcolo Midas GTS NX 2014, che riproducono prove di estrusione su campioni triassiali. Lo studio si concentra su terreni in condizioni non drenate che hanno un comportamento, in prima approssimazione, indipendente dal tempo. Si sono eseguite analisi statiche in assialsimmetria, utilizzando un legame costitutivo elastico-perfettamente plastico con legge di rottura alla Tresca, per ottenere la relazione fra sforzi e spostamenti del fronte (curva caratteristica) e lo sviluppo di plasticizzazioni intorno al fronte. L'interpretazione dei risultati è stata guidata dall'analisi della risposta di fronti di scavo di gallerie.

Nel passato si sono utilizzate le prove di estrusione triassiali per prevedere qualitativamente la risposta di tunnel, tuttavia queste prove sono affette dai problemi legati alla sperimentazione in scala. Questo ha portato alla ricerca dell'influenza delle condizioni al contorno, in particolare la geometria del dominio, sui risultati delle prove di estrusione. Questo studio mostra che c'è una forte dipendenza fra la geometria del sistema e il rapporto fra io stato di sforzo iniziale e la resistenza al taglio. Ad esempio i risultati numerici mostrano che nel caso in cui il rapporto fra sforzo iniziale e coesione non drenata è inferiore a 8.5 è possibile considerare un campione il cui rapporto fra diametro esterno e diametro della camera di estruzsione è pari a 5.4. Un altro problema è riprodurre le condizioni in sito in termini di stato di sforzo e condizioni al contorno. In particolare si nota che per effetto dello scavo (visto come progressiva riduzione della pressione al fronte) nelle prove di estrusione sulla base del campione opposta alla camera di estrusione si assiste ad una progressiva diminuzione dello stato di sforzo, mentre nel caso di scavi di gallerie lo sforzo corrispondente rimane costante. Per tale ragione si ottiene che nel sistema riprodotto da prove di estrusione triassiale la forza instabilizzante si riduce progressivamente e dunque la risposta del sistema sarà più stabile rispetto alla risposta che avrebbe una galleria nelle stesse conclusioni.

Nello studio sono presenti delle conclusioni che sonovalide sia per le prove di estrusione sia per lo scavo di gallerie: (i) avviene una migrazione di sforzi definita "effetto tenaglia". (ii) Definendo un opportuno piano adimensionale tutti i risultati delle analisi numeriche collassano su un'unica curva definita Curva Caratteristica Madre per il Fronte (FMC). (iii) Nonostante le curve madri ottenute dai diversi modelli siano diverse (per effetto delle condizioni al contorno) i modelli forniscono una risposta simile.

Keywords: *Prove di estrusione; Tunnel profondi; argilla; Analisi a Elementi Finiti; Assialsimmetria; Elasticità e plasticità*

Table of contents

List of figure

List of table

Symbols

Symbols

a	Radius of the uniform load, p, considering an elastic problem
ALSR	The absolute load sharing ratio
b	Axis between a and z which its inclination is 45 degree considering elastic problem
c	The cohesion of soil
c′	The effective cohesion of soil
CU	The consolidated and undrained test in standard triaxial test
C^{ep}	The consistent tangent stiffness matrix
D	Internal diameter of extrusion chamber or the equivalent tunnel diameter
D	Material stiffness matrix
D_{ep}	Continuum tangent stiffness matrix
E	The Young modulus of soil
f	The failure function
g	The plastic potential
el.	Index for 'elastic'
E_u	The Young modulus of soil in undrained condition
FMC	Front Mother Characteristic
H	The tunnel cover
H_1	Height of the extrusion chamber of extrusion test
H_2	Height of the symmetry of axis of axisymmetrical model of extrusion test
I and J	Scalar invariance of stress
K_0	The coefficient of lateral earth pressure. In standard triaxial test it can be defined as ratio between radial and axial pressure
$K_{0;lower}$	Lowest value of K_0 that can be applied in the extrusion test
$K_{0;upper}$	Highest value of K_0 that can be applied in the extrusion test
K_{el}	The elastic slope on the $RLSR$-Ω_f plane for non-rigid lining
$K_{el,r}$	The elastic slope on the $RLSR$-Ω_f plane for rigid lining
N	Stability ratio proposed by Broms and Bennemark (1967)
N^*	Normalised stability ratio by considering the coefficient of lateral earth pressure
n_j	Direction vector
s	The dimensionless average displacement of the front
S_u	The undrained strength of cohesive soil
s_{ij}	The deviatoric stress
u_σ	the dimensionless average displacement of the front
p	An uniform load considering an elastic problem
pl	Index for 'plastic'
q	An uniform terrain load
Q	Coefficient matrix as hardening variable
r	Residual vector
RLSR	the relative load sharing ratio
t_r	Thickness of circular steel plate being extruded to extrusion test's sample
U_f	Average of radial displacement of the face of the tunnel or extrusion chamber
$U_{r;el}$	Average of radial displacement of the face of the tunnel or extrusion chamber for perfectly elastic condition

UU	The unconsolidated and undrained test in standard triaxial test
u_z	Displacement at elevation z below the ground, considering elastic problem
U_σ	The normalized radial displacement, $U_f/U_{f;el}$
x_f	Horizontal distance from the tunnel face
z	Elevation

Greek's symbols

α	Parameter of a function used for interpolation
β	Parameter of a function used for interpolation
δ_{ij}	Kronecker delta
$\dot{\lambda}_\iota$	Plastic multiplier
$\boldsymbol{\varepsilon}^{el}$	Elastic strain
$\boldsymbol{\varepsilon}^{pl}$	Plastic strain
γ	Parameter of a function used for interpolation or unit weight of soil
γ_{sat}	The saturated weightper unit volume of the soil
$\boldsymbol{\kappa}$	The hardening parameter
$\varnothing$	External diameter of sample of extrusion test
$\boldsymbol{\sigma}$	Stress vector
σ_a	Axial pressure
σ_f	The pressure in front of the face of the tunnel or extrusion chamber
σ_m	The average stress
σ_r	Radial pressure
σ_s	The overburden total soil pressure located at the centre of the tunnel
σ_{xx}	Total stress in x axis
σ_0	Initial horizontal stress at face or initial pressure in extrusion tests
σ_1 and σ_3	Principle stresses in axial and horizontal or radial directions
θ_0	Lode's angle
ψ	Dilatancy angle of soil
$\Omega_{f;r}$	The dimensionless average displacement of the front for rigid lining
v	The Poisson's ratio of soils

1. Introduction

1.1 General

Tunnelling has become a preferred construction as urbanization increases and available land decreases in all over the world. In many cases, tunnels are constructed for easier access for new transportation or underground lifelines (**Figure 1-1a**). The inherent problem associated with underground construction in soft soil is that underground excavation alters the stress field in the surrounding. Since soil cannot bear superimposed external stress, therefore ground deformation occurs. One of the main considerations concerning construction of tunnel is the stability of tunnel face during excavation. (**Figure 1-1b**).

(a)

(b)
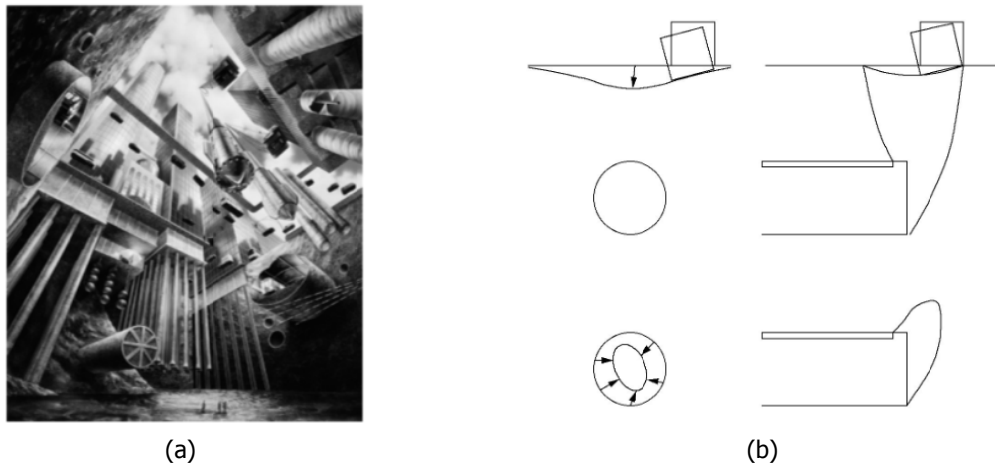
Figure 1-1 (a) Underground congestion in the urban environment (courtesy Keller) and (b) alteration in stresses due to undergound excavations. Top: for a shallow tunnel. Bottom: for a deep tunnel (Anagnostou, 2007).

One method that is commonly used nowadays in tunneling is so called conventional tunnel method (CTM) as shown in **Figure 1-2**; despite tunnel boring machines are becoming every year more popular in urban and extra-urban territories. CTM is preferred because it is convenient for the irregularity of both the trajectory and the shape of the tunnel. One of excavation method for CTM is mechanically supported excavation mainly used in soft ground and in weak rocks. In some cases it is also necessary to have a primary support, such as rock bolts or *shotcrete* with or without fiber reinforced or wire mesh, to stabilize the underground opening until the final lining is installed (ITA, 2009).

(a)

(b)
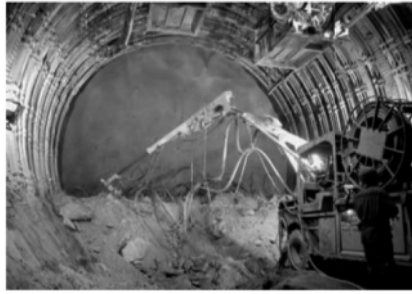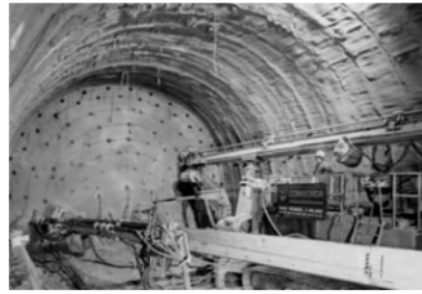
(c)   (d)

Figure 1-2 Conventional Tunneling Method (CTM) with different mechanically supported excavations using (a) shovel, (b) road header, (c) in combination with primary support using shortcete and (d) face anchors (ITA, 2009).

The main aim is to study profoundly stability of the underground opening of CTM in clay soil by adopting results of extrusion tests by means of numerical analyses thanks to a commercial finite element code, Midas GTS NX 2014. The focus is on the relationship between the extrusion and stress, and plastic deformation around the extrusion chamber. The present study considers similar extrusion tests which were already developed by Lunardi (1999), but with some improvement considering procedure of the tests. The results of the present study are also compared with those of the 3D finite element model of real tunnel (di prisco, *et al.*, 2015) in order to better interpreting the results. Therefore, this 3D model is considered as a reference model of the study.

The present study is part of a project titled: "An experimental/numerical program aimed at defining innovative design solutions for the front reinforcements by means of fibreglass tubes considering numerical, theortical and experimental analysis" funded by the Italian Ministry of University and Scientific Research (MIUR), Rocksoil S.P.A. and Maccaferri S.P.A.

1.2 Framework within risk mitigation

One of popular definition of risk is that it can be described as the convolution among hazard, vulnerability, exposure and sometimes resilience. Hazard relates to characteristics of the dangerous agent or phenomena which causes an event. Vulnerability corresponds to propensity to any kind of damage. Exposure relates to number and dimension of living things within a dangerous area. Resilience means capacity of bouncing back after given stress and even more to transfer damage into better opportunity. In general, implementation of any strategy aimed at reducing level of vulnerability, exposure and hazard, and increasing resilience may reduce risk.

Main source of risk associated with CTM tunnel project can be either found during the design and or construction phase. If we focus on the risk associated with the design process, one of the main considerations is the tunnel support system at the face tunnelling. The key feature of the CTM design philosophy is that the initial support system on the face tunnelling must have stress-deformation characteristics suitable for ground conditions and its installation must be timed with respect to the deformation of the ground (Sousa, 2010). Müller and Fecker (1978) proposed a schematic of ground-support interaction curves (relationship between stress and deformation) as shown in **Figure 1-3**. If a stiffer support (c) is used it will carry more load than a more flexible one (d) because the ground won't be able to deform as much until the equilibrium (convergence) is reached. As important as the rigidity of the support is the time when it is applied. If the same support is applied after some deformation occurs, it will reach the equilibrium with a lower load on the support. Therefore the support should not be too stiff (c) nor too flexible (d) and it should not be applied too early (a), in order to take advantage of the reduction in load in the support, nor too late (b) in order not to increase the deformation drastically and not to have instability.
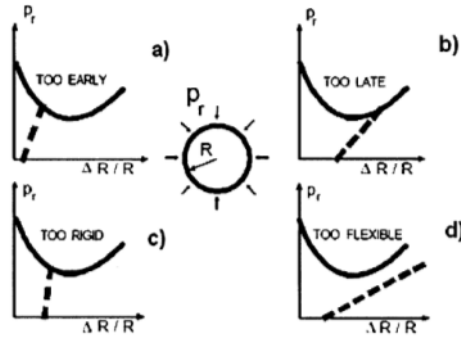
Figure 1-3 The basic princple design philoshopy of conventional tunneling method (CTM), after Müller and Fecker, 1978.

Considering the framework of risk that already described, the scope of this study can be included within the framework of hazard, e.g. stability faces tunnelling. The use of this type of analysis could be useful to improve the theoretical knowledge considering possible instability of the face tunnelling in order to avoid such of hazard, therefore reducing risk.

1.3 Outline

Chapter 2 describes the general overview of the research. This includes the questions that are addressed and its research objective. Chapter 3 discusses the constitutive model that has been implemented to the present study. A brief introduction of analysis of the software has been also included. Chapter 4 focuses on about how to set up 2D FEM model of triaxial extrusion test considering different discretization and geometry. Idealization with respect to the real and complex behaviour of face tunnelling has been assumed. The final model has been validated with a 3D FEM model of extrusion test and has been chosen for further analysis. Chapter 5 concerns the analysis and starts with a parametric study. Elastic and elasto-plastic solutions of the 2D FEM extrusion test have been discussed. Moreover, the results are compared with those of the 3D FEM real tunnel as a reference model (di Prisco *et al.*, 2015). The differences are critically discussed. In the last chapter the study is summarized. Moreover, recommendations for any future development have been discussed.

2. Literature review, research methodology and objective

2.1 Extrusion triaxial test

A comprehensive understanding of the tunnelling is important because it induces displacements and stresses and impacts on surrounding the face tunnel. Geotechnical engineering researchers depend on physical modelling to understand the process. Full-scale experiments are very expensive and hard to repeat. Therefore, reduced physical modelling of face tunnel on soft ground is preferred in order to understand different phenomena such as deformation patterns and failure mechanism. In general, we can have three different categories of reduced physical model: centrifuge, 1g scale and extrusion tests. The application of extrusion tests to study the stability around the opening face had already been implemented by Broms and Bennemark (1967). Moreover, they also developed similar test by modifying standard triaxial tests. Similar apparatus had been also examined by Attewel and Boden (1968). Lunardi (1990) continued to develop a dynamic experimental device with the same principle (extrusion test). The results of this test are typically carried out during preliminary phase of tunnel construction (Lunardi, 1995) in order to make prediction of the deformation response of the face in term of the characteristic lines.

In this section, we describe in detail about the extrusion tests developed by different researches as listed in the previous paragraph. Any limitation of the tests developed by each developer is also discussed.

2.1.1 Broms and Bennemark, 1967 (Load controlled test)

Broms & Bennemark (1967) developed the extrusion experiment for homogenous clay. This test was originally intended for studying the stability of clay mass located behind a circular vertical opening. The hypothesis was analogous to that proposed to predict failure by bottom heave (Bjerrum and Eide, 1956) having centres deeper than four hole-diameters from the ground surface. It has been shown that failure by bottom heave takes place when the total overburden pressure at the level of bottom of an excavation exceeds about nine times the undrained strength of the clay (**Figure 2-1**).
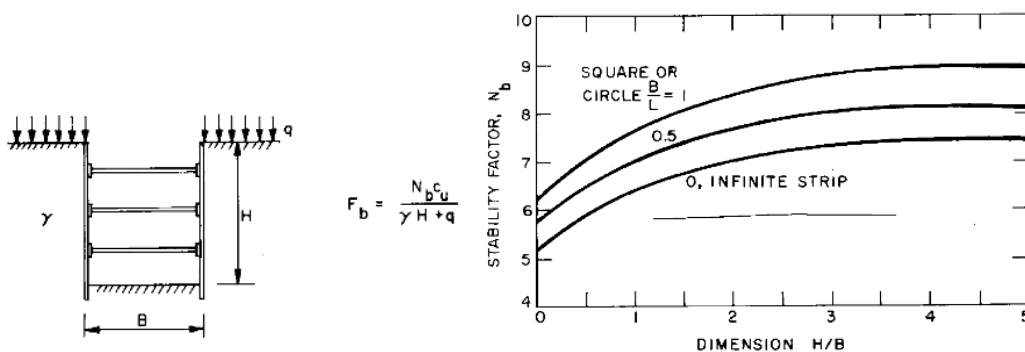
Figure 2-1 Base heave stability in supported retaining wall (Bjerrum and Eide, 1956)

In the case of a vertical circular hole, this type of failure, assumed that the failure surface is cylindrical, is expected at a lower overburden pressure than that causing bottom heave, as, which is $6.28\,S_u$. This critical overburden pressure is independent of the diameter of the hole. While the value of this coefficient (ratio between the overburden pressure and undrained shear strength) will depend on the assumed boundary conditions, e.g. the roughness of the wall and the shape of the hole.
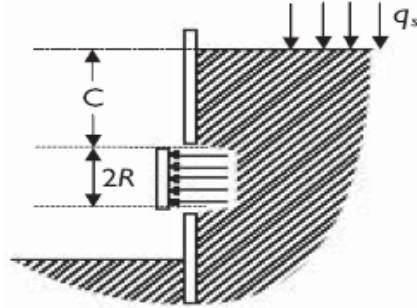
Figure 2-2 A circular opening in a thin retaining wall that supports soft soil to study face stability of tunnel (Broms & Bennemark, 1971)

The undisturbed soil samples were extruded from the sampler into a thin walled brass cylinder with a length of 6 cm and the same inside diameter as the sampler, 5 cm. The brass cylinder was provided at mid-height with circular holes having either 1 or 2 cm diameter (**Figure 2-3**). They modelled overburden pressure by applying an axial surcharge over a clay sample that pushed the clay through a circular hole on the wall of a vertical tube. Confining pressure was used to investigate stability condition or effect of compression pressure to prevent a cohesive material from flowing into a tunnel.
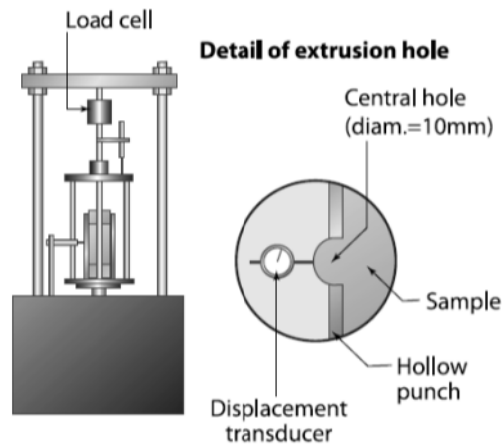
Figure 2-3 Extrusion test and extrusion hole cavity (Broms and Bennemark, 1967. Courtesy: Lunardi, 2008).

The stability conditions of the extrusion test were defined as follows:

$$N = \frac{\sigma_s - \sigma_f}{S_u}$$

Equation 2-1

where σ_s refers to the overburden total soil pressure located at the centre of the tunnel for field cases in their study,

$$\sigma_s = \gamma \left(H + \frac{D}{2} \right) + q$$

Equation 2-2

which H is the tunnel cover, D is the equivalent tunnel diameter, γ is unit weight of soil and q is an uniform terrain load and σ_f is the horizontal pressure in front of the face of the tunnel. Moreover, they compared the laboratory tests and field measurements. They concluded that the stability ratio should be lesser than 6 to 8 for the opening to remain stable and that this condition only applies to openings having centres deeper than four hole-diameters from the ground surface.

2.1.2 Attewel and Boden, 1971 (Displacement controlled test)

Attewell and Boden (1971) conducted similar studies with those of Broms and Bennemark (1967). They concluded that the stability ratio at collapse is 4.0. This differed from that found in Broms and Bennermark's tests because displacements of the extruding clay plug instead of the piston that pushed the clay were used to determine the collapse pressure (**Figure 2-4**).
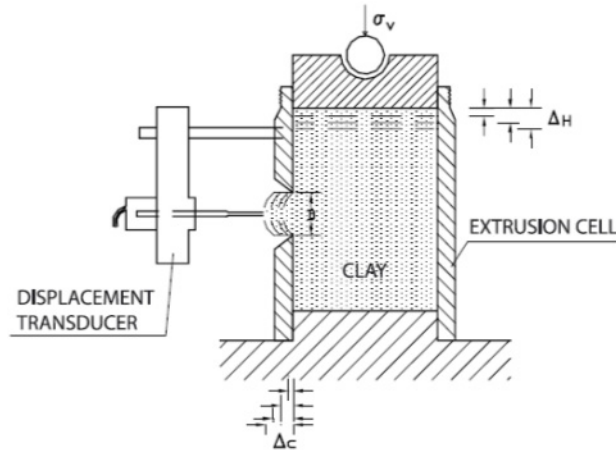
Figure 2-4 Extrusion test (Attewel and Boden, 1971. Courtesy: Lunardi, 2008).

Some limitations of these tests (for Broms and Bennemark, 1967 and Attewel and Boden, 1971):
- The experiments were conducted in 1-g and so the effects of gravity were excluded. Thus, the influences of soil self-weight and ground cover thickness cannot be studied;
- Their tests were originally intended to study the stability of an opening in a thin retaining wall that supports soft soil and therefore the tests involve the extrusion of soft soil through a hole in a vertical cylinder. When this is applied to a tunnel heading stability analysis, this assumes a vertical plane of stress acting on the tunnel face that might be oversimplification;
- The field observations were mostly base tunnels having centres deeper than four hole-diameters from the ground surface;
- The results showed only the behaviour of the tunnel stability at failure.

2.1.3 Lunardi, 1990 (Load controlled test)

A cylindrical specimen with a diameter of 50 mm and a height of 10 mm is used having similar dimension for a triaxial test. Hollow steel, with an outer diameter of 22 mm, inner diameter of 16 mm and height of about 32 mm, is axially driven into the top part of the undisturbed specimen. By using a special die, at the end of the penetration, a cavity is formed having dimensions coinciding with the diameter of the extrusion chamber. On its end it is fixed with a thin latex membrane that separates the interior of the cavity and the specimen. Water is filled in the cavity and is connected to an external burette to measure the pressure within the interior. By letting the water to be drained it is possible to have decreasing in pressure within the cavity.
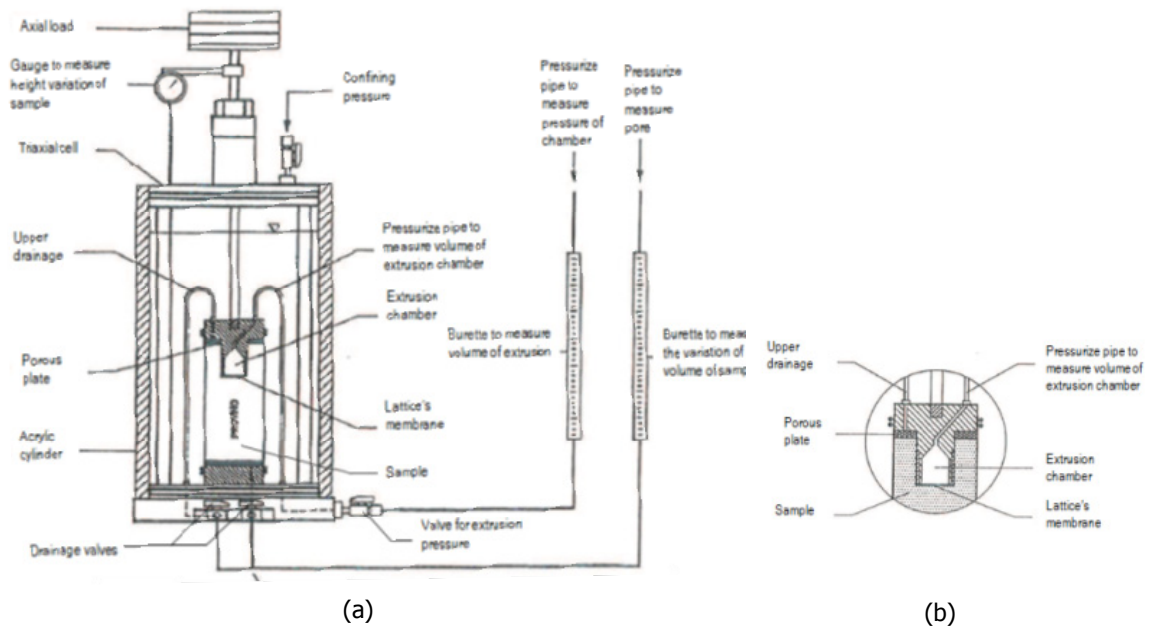
Figure 2-5 (a) The extrusion test on triaxial specimen and (b) extrusion chamber or cavity (Lunardi, 1990).

Equipment shown in **Figure 2-5** is similar to the triaxial used for undrained consolidated anisotropic test.

The specimen is prepared in saturated condition against back-pressure and subsequently consolidated isotropic or anisotropic in conditions K_0. During this phase, the pressure inside the extrusion chamber is maintained equal to the total isotropic stress (in the case of isotropic consolidation) or only the vertical stress (in the case of anisotropic consolidation) acting on the specimen.

Having consolidation condition during the test, the extrusion step is started decreasing, in several steps. Of each step the pressure inside the chamber and the variation of height of the test specimens are measured. Every step has been continued until the stabilization of the extrusion or otherwise until his defection tube being corrected.

There are some remarks considering this type of extrusion tests:

- The test is performed in the drained condition in the consolidation phase, while in the real case the face stability of the tunnel is in undrained behavior, since the rate of the excavation is adequate fast in such that no consolidation process would develop significantly;
- Another issue is regarding possible boundary effect considering dimension of the sample.

2.2 Three-dimensional problems of stability around face tunnelling

Empirical formula have been established to roughly estimate the load acting on the support structure (e.g. Terzaghi, 1943; Bjerrum & Eide, 1956, Brom & Bennemark, 1971) to justify only in the case of shallow tunnelling according to mass material above the tunnel. See **Figure 2-1**, **Figure 2-2** and **Figure 2-6.**
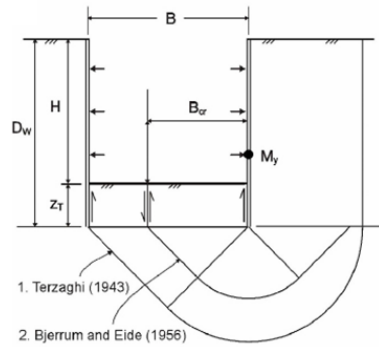
Figure 2-6 Analgous model of base heave stability on the support structure (Terzaghi, 1943; Bjerrum & Eide, 1951)

In more advance approach, the attempt tried to construct limit equilibrium (Horn, 1961 in **Figure 2-7**) and kinematic analysis based on arbitrarily defining certain failure mechanism around face tunnelling (Mair, 1979; Davis, *et al.,* 1980; Casarin & Mair, 1981; Leca & Dormieux, 1990; Klar *et.al.*, 2007; Molen *et.al.*, 2009 in **Figure 2-8**).
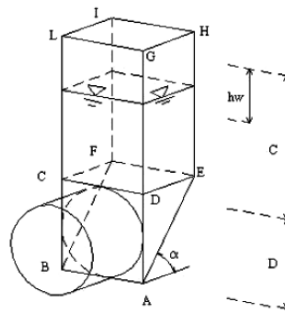
Figure 2-7 Limit equilibrium model for tunnel face (Horn, 1961)

In fact these methods involve the construction of rupture figures and defining possible critical equilibrium from the point of view of the equilibrium of forces.

(a)

(b)

(c)

(d)

(e)

(f)
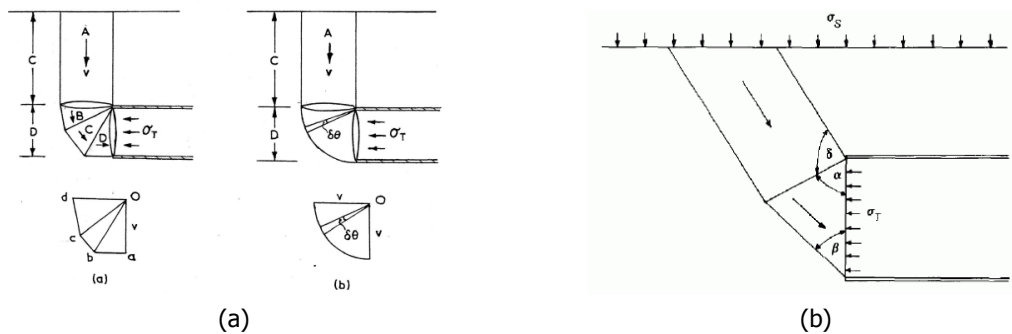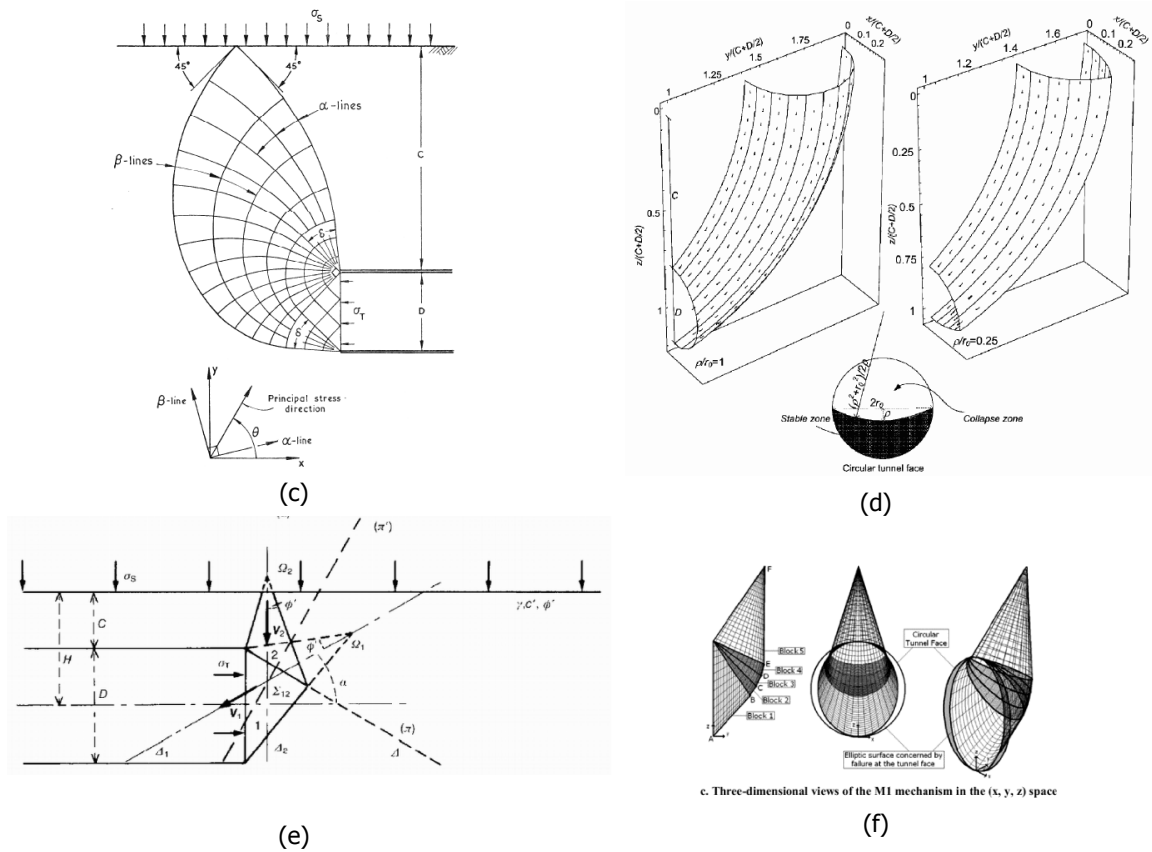
Figure 2-8 Mechanism for collapse of tunnel heading: (a) for fully lined to the face (Mair, 1979); (b) for upperbound failure (Davis *et.al.,* 1980); (c) considering net of stress characteristic (Casarin & Mair, 1981); (d) in compressible material (Klar *et.al,* 2007); (e) and (f) using conical blocks in Mohr Coulomb material (Leca & Dormieux, 1990; Molen *et.al.,* 2009).

Moreover, Lombardi (1974) already emphasised that the excavation of a tunnel is a problem of three-dimensional stresses and deformations in the region of the face where there is a change in the stress field due to possible shearing stresses in planes perpendicular to the tunnel axis (**Figure 2-9**).
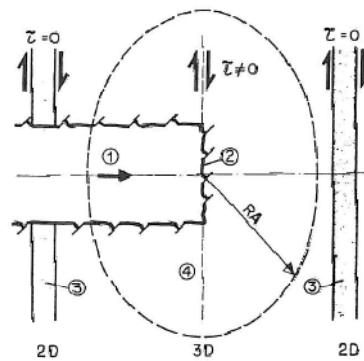
Figure 2-9 Stress state around the face of deep tunnel. (1) axis of the tunnel, (2) face, (3) pseudo-two-dimensional behavior, (4) zone of influence of the face and (RA) radius of influence of the face (Lombardi, 1974).

Therefore, a complete study of tunnel face stability has to deal with the three-dimensional field. A general method of calculation this three-dimensional problem is the use of a 3D finite element (FEM) analysis. Study of face stability of shallow tunnels in granular strata using 3D FEM analyses had been considered by

9

Vermeer *et al.*, (2002), Yoo (2002), Sterpi and Cividini (2004), Shin *et al.* (2008) and Kirsch (2009).

(a)   (b)
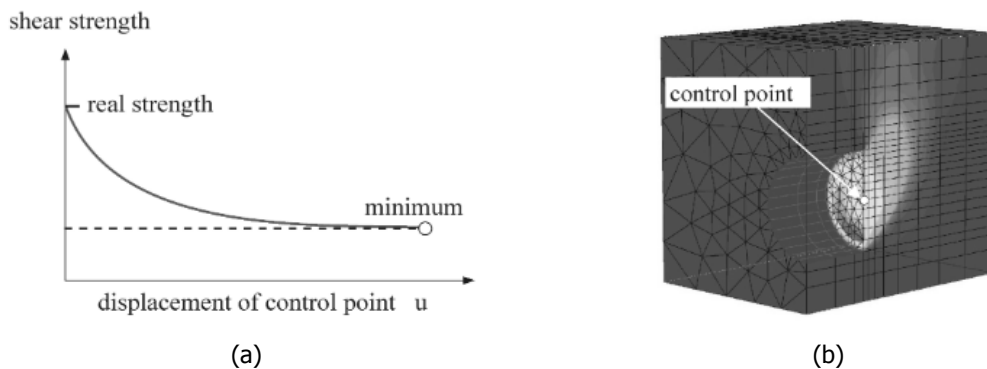
Figure 2-10 (a) Typical strength-displacement curve. (b) Shading of incremental displacement at collapse (Vermeer *et al.,* 2002).

The use of the 3D FEM analyses to meet the problems (as described previously) seems to encounter with the enormous number of elements, hence, enormous computation resources (storage and time). Special cases have been also examined by eliminating one dimension in order to save computation time. For instance, a pseudo-two dimensional stress can be assumed only at certain distance out of the radius of influence of the face, since it might be possible to assume that the shearing stresses in planes perpendicular to the tunnel axis are nil. This radius of influence denotes the area in which the influence of the face is still significant (**Figure 2-9**). If we assume an ideally elastic behaviour of material, the effect of any excavation on the radius would extend infinitely. But in practice, since in most materials have also plastic behaviour, the radius of action may be assumed to be few times of diameter of the tunnel (Lombardi, 1974). This zone depends of the diameter of the tunnel, soil strength, stress states and advance rate of the excavation (Lunardi, 1995). Consequently, any two-dimensional state of stresses or deformations cannot represent complete and accurate solution of the real three-dimensional problem at face.

2.3 Research methodology

2.3.1 Axisymmetric finite element method

As it was described, the complete study of face tunnel has to deal with the three-dimensional fields existing in the area of the tunnelling face. Is it possible to study by means of any two-dimensional FEM solution? There are two kinds of two-dimensional approach. First approach is two-dimensional model in a plane perpendicular to the tunnel axis. If we consider stability of the face tunnelling, the final state of equilibrium will be reached within relatively short distance (see also **Figure 2-9**) from the face (Lombardi, 1974). Therefore, it is clear that this approach is clearly inadequate to study stability near the face. Another approach, a special one, is two-dimensional method that takes into account of the three-dimensional effect. This radial symmetry model aims of modifying one dimension, or is so called axisymmetry. This approach has been examined to study development of plastic zone around deep boreholes (Desai and Reese, 1970), to estimate the face influence on tunnel wall convergence along tunnel and consequences for support loading (Wagner, 1970, Daemen and Fairhurst, 1970) in rock (Daemen, 1975) as shown in **Figure 2-11**.

<center>(a)   (b)</center>
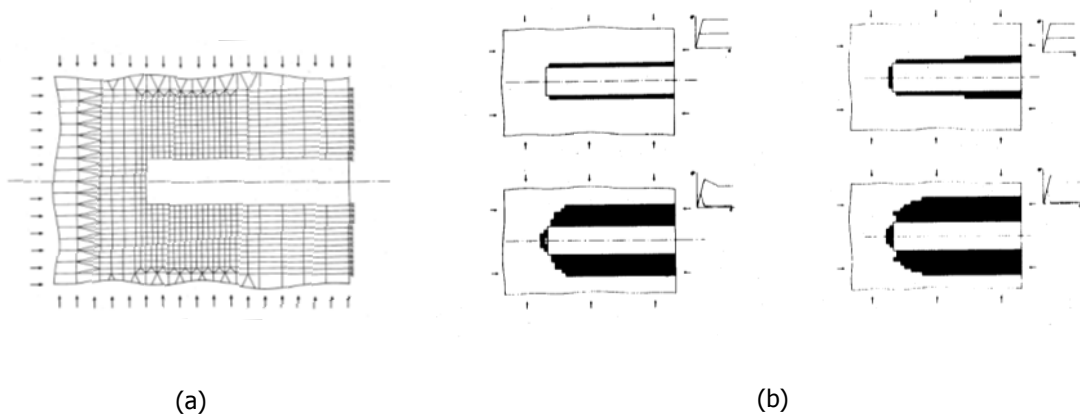
Figure 2-11 (a) Axisymmetric finite element model to estimate the face influence on tunnel wall convergence in rock and (b) typical evolution of plastic zone near the tunnel face for increasing field stresses in a rock (Daemen, 1975).

Similar approach had been applied to study of the face influence in circular tunnel (Shin, 2000) as shown in **Figure 2-12**.
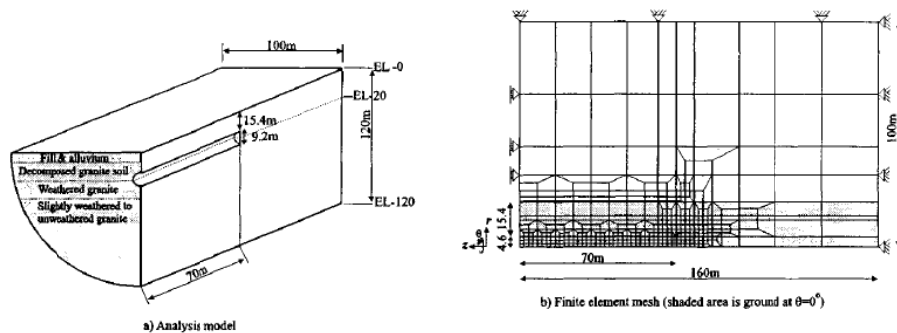
Figure 2-12 Axially symmetric geometry to analysis advance of a circular tunnel heading (Shin, 2000)

Prior to the discussion from the previous paragraphs, the present study focuses on the use of axisymmetric finite element to model the extrusion triaxial test (Lunardi, 1990) with modification of procedure in order to study behaviour of stability of the face tunnelling. Indeed, a three-dimensional FEM model would give better and complete solution, but it requires huge different order of magnitude in computation time and storage. In this study, a commercial software MIDAS GTS NX 2014 version has been used to set-up the 2D FEM extrusion model.

2.3.2   Type of material

2.3.2.1   **Viscosity**

There are two types of rocks or soils considering tunnelling. There are rocks or soils that behave instantaneously, i.e. without viscosity effect. This can behave ideally elastic, the other has an elasto-plastic behaviour whose viscous phase is practically negligible. The other group considers material having a viscous behaviour, i.e. capable of time dependent deformations. The former group, rocks or soil without viscous effect are considered in the present analysis.

2.3.2.2   **Drained and undrained conditions**

Drained condition analyses are appropriate when permeability is high, rate of loading is low, and short term is not important for considered problem. On the other hand, undrained conditions are appropriate when permeability is low or loading rate is very high and short term behaviour has to be analysed.

According to a parametric study by Anagnostou and Kovári (1996), drained conditions tend to apply when the ground permeability is higher than 10^{-7} to 10^{-6} m/s and the net excavation advance rate is 0.1 to 1.0 m/hour or less. In a predominately sandy soil, therefore, drained stability conditions should be considered. In a clayey, low-permeability soil the undrained analysis is valid during excavation. In general implication of the undrained behaviour would be that: excess pore pressures are not generated, no volume change is expected. The undrained analysis requires analysis in terms of total stresses and zero dilatancy angle, because clays (regardless of over consolidated layers) are characterized by a very low amount of dilation ($\psi \approx 0$).

Although undrained conditions are valid during continuous excavation, but in case of excavation standstill, drained conditions have to be applied. Therefore, it would be also necessary to investigate drained condition for excavation in clay. But this particular case is out of scope of the present study.

To summarize, the present study concerns any rocks or soils that have an elasto-plastic behaviour whose viscous effect is negligible. Moreover, undrained condition has been assumed for this type of material assuming low permeability, very high loading rate and negligible long term behaviour.

2.3.3   Research question

Although the experiments on extrusion through the face of a tunnel conducted by Broms and Bennermark (1967), Attwell and Boden, and continued by Lunardi furnish a guide that is sufficiently reliable for predictions of the phenomenon in purely cohesive soils, but it must be kept in mind that all the problems, that are typical of studies performed in the laboratory, would give effect of small scale due to geometry, impossibility of working on completely undisturbed samples (in some type of soil), difficulty in reproducing *in situ* conditions faithfully and the results that cannot be generalized to all types of ground. Moreover, there would be consequence when two-dimensional approaches (whether it is numerical or experimental) are considered to study the three-dimensional problem of stability around face tunneling. These lead us to discuss the following topics:

1. Is there any limitation of extrusion triaxial test due to any possible scale effect on boundaries? Can we consider this type of test for all type of grounds? These questions are relevant since a standard triaxial test can only be used for certain dimension of sample and limited pressure that can be applied;
2. How to define correct procedure in extrusion triaxial tests?;
3. Is it possible reproducing *in situ* conditions of tunnel in extrusion tests? What are consequence adopting the results extrusion tests to study the real three-dimensional problem of face stability?.

2.4   Objective

In order to answer all the research questions, the following section describes how we chose the scheme of the study.

2.4.1   Set up of numerical model of triaxial extrusion test

2.4.1.1   Constitutive model

In this study, a simple model of elastic-perfectly-plastic model has been used to simplify the real elasto-plastic behaviour of the soil under undrained conditions with negligible vicious effects. In this case, Tresca failure criteria are considered. The main motivation to use this model is because it is very simple and it keeps the computational result reasonable unlike in the case of the linear elastic or the rigid perfectly plastic model that are in general not able to accurately representing the true behaviour of the soil. Moreover, the main parameters in the model, which are the Young's modulus, Poisson's ratio, and undrained shear strength, are quite well known by geotechnical engineer and are relatively simple to obtain and to use.

Geometry investigation

The first phase was intended to set up the 2D FEM extrusion test considering parameters and boundary conditions that govern the results and any possible effect on boundary conditions due to geometry (because of the limitation of standard trixial test, e.g. size of the sample and maximum applied confining stress).

2.4.1.3 **Validation**

An essential part of analysis using any FEM method is to validate the numerical models. In this study, the axisymmetrical FEM model is validated considering the 3D model of the extrusion test (4.4.4).

2.4.2 Reference numerical model: the 3D tunnel model (di Prisco *et al.*, 2015)

Some authors such as Vermeer *et al.*, (2002), Yoo (2002), Sterpi and Cividini (2004), Shin *et al.* (2008) and Kirsch (2009) considered 3D FEM analysis to study face stability of shallow tunnels in granular strata. One of particular author, di Prisco *et al.* (2015) studied 3D FEM for tunnels at deep cohesive layers and reproduced the similar principle of the characteristic curve.

As it was discussed in section 2.2, the behaviour of face stability is really a three-dimensional problem. A 3D FEM numerical analysis of tunnel would provide representative behaviour the stress state around the face. Therefore, the 3D FEM tunnel model that was currently studied by di Prisco *et al.* (2015) is chosen as a reference model. Their studies were carried out using the same commercial software, e.g. MIDAS GTS NX and were considered similar constitutive model, liner elastic-perfectly plastic with Tresca failure criteria. In the present study, parametric studies have been also carried out. The results of the sensitivity analyses have been compared with those of the reference model. The aim of making the comparison is to check the performance or quality of results provided by the 2D FEM extrusion test with respect to the 'real' behavior of the tunnel.

3.   Constitutive model and reference analysis

3.1   Introduction

In this study, Tresca's failure criteria have been chosen as one of elasto-plastic model that exists in literature. The main motivation to use this model is because it is very simple and it keeps the computational result reasonable unlike in the case of the linear elastic or the rigid perfectly plastic model that are in general not able to accurately   representing true behaviour of soil. Moreover, the main parameters in the Tresca model, which are the Young's modulus, Poisson's ratio, the shear strength, are quite well known for geotechnical engineer and are relatively simple to obtain and to use. In contrast to the more advance soil models such us the soft-soil creep model or cam clay model, because it requires calibration in order to get more advance parameters. Nevertheless, the material that has been considered in the present study such as rocks or soils that have elasto-plastic behaviour whose viscous effect is negligible. Moreover, undrained condition has been assumed for this type of material assuming low permeability, very high loading rate and negligible long-term behaviour.

In this section an introduction of a linear elasto plastic behaviour is briefly described in order to highlight the fundamental difference between elastic and elasto plastic behaviour. Then, simple elasto plastic model without any hardening or softening is introduced as it is considered in the present study. It is also highlighted how the Tresca yield function is obtained. This explanation is referred to Potts (1990), and the manual of MIDAS GTS NX 2014.

3.2   Linear elastic perfectly plastic

As introduction, it is ideally to describe a linear elasto plastic behaviour. For material with linear elastic perfectly plastic, the yield surface is fixed in stress space. Moreover, it does not change position when loading take place. The behaviour is elastic if the stress state remains below the yield surface.
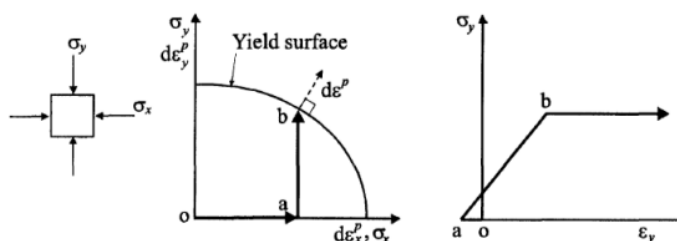
Figure 3-1 Two dimensional behavior of a linear elastic perfectly plastic material considering uniaxial (Potts, 1990).

In **Figure 3-1** shows a two dimensional system of stresses, σ_x and σ_y, considering an element of soil. At point '0' the initial stress of the sample is zero. While keeping $\sigma_y = 0$, the stress component σ_x is increased until point 'a'. Behavior is entirely elastic since the stress state remains inside the yield surface (curve). Although, σ_y does not change, there is a strain ε_y due to Poisson's ratio effect (ε_y is to be negative if $0 < v < 1/2$). The strain ε_y can only be zero if Poisson's ratio, v, is also zero. Then σ_y is increased while the stress σ_x is kept constant until it reaches the yield surface at point 'b'. The behavior is again elastic while the stress remains below the yield surface and the strain ε_y is controlled by the elastic moduli. Once the yield surface is reached (point 'b'), it is not possible to increase σ_y any further. In this case, plastic straining occurs. If the stress state is maintained on the yielding surface (point 'b'), the plastic strains will keep increasing indefinitely. However, the ratio between plastic components $d\varepsilon_x^p$ and $d\varepsilon_y^p$ is fixed by the gradient of yield surface which equals to the plastic potential at point 'b'. Consequently, the element of soil has failed.

It should be note that fundamental difference between elastic and elasto-plastic behavior is that

the former strain increments are proportional to stress increment, whereas in the latter strain increments are a function of the current stress state. Therefore, in real soil the strain increment are not likely to be in the same directions at the applied stress increments.

In the above discussion, it is implicitly assumed that the elastic behavior in the elastic perfectly plastic material is perfectly linear. However, this is not realistic and it is possible to combine nonlinear elasticity with the elasto-plastic framework (Potts, 1990). Due to the complex of the nature of soil it has not been possible to develop an elasto-plastic model that can capture all the facets of real soil behavior and be defined by a limited set of inputs parameters that can be readily obtained from simple laboratory test. There are many such models currently in the literature. These range from simple to complex models. Some simple models are Tresca and Mohr Coulomb model. In the present study Tresca model is considered. In the following sections the material properties considering the linear and plastic parts of the chosen model is briefly described.

3.3 Material Properties of Linear Elastic Isotropic

Linear elastic isotropic materials are based on Hooke's law. Using the modulus of elasticity, E, Poisson's ratio v and coefficient of thermal expansion, the stress-strain relationship for any 3D isotropic materials can be expressed as follows:

$$
\begin{Bmatrix} \sigma_{xx} \\ \sigma_{yy} \\ \sigma_{zz} \\ \tau_{xy} \\ \tau_{yz} \\ \tau_{zx} \end{Bmatrix} =
\begin{bmatrix}
\frac{E(1-v)}{(1+v)(1-2v)} & \frac{vE(1-v)}{(1+v)(1-2v)} & \frac{vE(1-v)}{(1+v)(1-2v)} & 0 & 0 & 0 \\
& \frac{E(1-v)}{(1+v)(1-2v)} & \frac{vE(1-v)}{(1+v)(1-2v)} & 0 & 0 & 0 \\
& & \frac{E(1-v)}{(1+v)(1-2v)} & 0 & 0 & 0 \\
& symmetric & & \frac{E}{2(1+v)} & 0 & 0 \\
& & & & \frac{E}{2(1+v)} & 0 \\
& & & & & \frac{E}{2(1+v)}
\end{bmatrix}
\begin{Bmatrix} \varepsilon_{xx} - \alpha\Delta T \\ \varepsilon_{yy} - \alpha\Delta T \\ \varepsilon_{zz} - \alpha\Delta T \\ \gamma_{xy} \\ \gamma_{yz} \\ \gamma_{zx} \end{Bmatrix}
$$

Equation 3-1

For 2D analysis, $\tau_{yz} = \tau_{zx} = \gamma_{yz} = \gamma_{zx} = 0$ and particularly for plain strain analysis $\varepsilon_{zz} = 0$

$$
\begin{Bmatrix} \sigma_{xx} \\ \sigma_{yy} \\ \tau_{xy} \end{Bmatrix} =
\begin{bmatrix}
\frac{E}{1-v^2} & \frac{vE}{1-v^2} & 0 \\
\frac{vE}{1-v^2} & \frac{E}{1-v^2} & 0 \\
0 & 0 & \frac{E}{2(1+v)}
\end{bmatrix}
\begin{Bmatrix} \varepsilon_{xx} - \alpha\Delta T \\ \varepsilon_{yy} - \alpha\Delta T \\ \gamma_{xy} \end{Bmatrix}
$$

Equation 3-2

For the present study it is assumed that there is no thermal expansion and the modulus of elasticity is constant with height.

As v approaches 0.5, the $(1-2v)$ term approaches '0' (zero), and this can cause numerical errors. Hence, the range of Poisson's ratio for isotropic materials is restricted as follows:

$$-1 < v < 0.5$$

Equation 3-3

3.4 Material properties of perfectly plastic

This section has been referred to the manual of GTS NX 2014.

3.4.1 Failure criterion and invariance

3.4.1.1 **Principle stress invariance**

Principal stress invariance is a convenient method of expressing the failure function. The stress induced at an arbitrary point within the material can be expressed using the following equation, which uses the direction vector n_j that defines the principal stress direction:

$$(\sigma_{ij} - \sigma\delta_{ij})n_j = 0$$

Equation 3-4

where δ_{ij} is Kronecker delta

$n_j \neq 0$ in **Equation 3-4** above, and the necessary and sufficient condition for **Equation 3-4** is as follows:

$$|\sigma_{ij} - \sigma\delta_{ij}| = 0$$

Equation 3-5

The matrix **Equation 3-4** can be expressed as a cubic equation for principal stress, as shown below:

$$\sigma^3 - I_1\sigma^2 + I_2\sigma + I_3$$

Equation 3-6

where,

$$I_1 = \sigma_x + \sigma_y + \sigma_z = \sigma_{ii}$$

Equation 3-7

$$I_2 = (\sigma_x\sigma_y + \sigma_y\sigma_z + \sigma_z\sigma_x) - (\tau_{xy}^2 + \tau_{yz}^2 + \tau_{zx}^2) = \frac{1}{2}(I_1{}^2 - \sigma_{ij}\sigma_{ji})$$

Equation 3-8

$$I_3 = \begin{vmatrix} \sigma_x & \tau_{xy} & \tau_{xz} \\ \tau_{yx} & \sigma_y & \tau_{yz} \\ \tau_{zx} & \tau_{zy} & \sigma_z \end{vmatrix} = \frac{1}{3}(\sigma_{ij}\sigma_{jk}\sigma_{ki}) - \frac{1}{2}I_1\sigma_{ij}\sigma_{ji} + \frac{1}{6}(I_3{}^3)$$

Equation 3-9

in which, I_1, I_2 and I_3 can be expressed using the principle stresses (σ_1, σ_2 and σ_3) as follows,

$$I_1 = \sigma_1 + \sigma_2 + \sigma_3$$
$$I_2 = \sigma_1\sigma_2 + \sigma_2\sigma_3 + \sigma_3\sigma_1$$
$$I_3 = \sigma_1\sigma_2\sigma_3$$

Equation 3-10

3.4.1.2 **Deviatoric stress invariance**

The stress tensor σ_{ij} can be divided into the hydrostatic pressure and invariant stress components, as shown below:

$$\sigma_{ij} = s_{ij} + \sigma_m\delta_{ij}$$

Equation 3-11

Here, σ_m represents the average stress as follows,

$$\sigma_m = \frac{1}{3}(\sigma_x + \sigma_y + \sigma_z) = \frac{1}{3}I_1$$

Equation 3-12

Also s_{ij} is the deviatoric stress and respresents the pure stress states as derives from the previous equation as follows,

$$s_{ij} = \sigma_{ij} - \sigma_m\delta_{ij}$$

Equation 3-13

The deviatoric stress invariance can be expressed,

$$\left|s_{ij} - s\delta_{ij}\right| = 0$$

Equation 3-14

Equation 3-14 can be expressed as follows,

$$s^3 - J_1 s^2 + J_2 s + J_3 = 0$$

Equation 3-15

Here,

$$J_1 = s_{ii} = s_x + s_y + s_z = 0$$
$$J_2 = \frac{1}{2} s_{ij} s_{ji} = \frac{1}{6}\left[(\sigma_x - \sigma_y)^2 + (\sigma_y - \sigma_z)^2 + (\sigma_z - \sigma_x)^2\right] + \tau_{xy}^2 + \tau_{yz}^2 + \tau_{zx}^2$$
$$J_3 = \begin{vmatrix} s_x & \tau_{xy} & \tau_{xz} \\ \tau_{yx} & s_y & \tau_{yz} \\ \tau_{zx} & \tau_{zy} & s_z \end{vmatrix} = \frac{1}{3}\left(s_{ij} s_{jk} s_{ki}\right)$$

Equation 3-16

$J_1, J_2,$ and J_3 can be expressed using the deviatoric principal stresses s_1, s_2 and s_3 as follows:

$$J_1 = s_1 + s_2 + s_3 = 0$$
$$J_2 = \frac{1}{2}(s_1^2 + s_2^2 + s_3^2) = \frac{1}{6}\left[(\sigma_1 - \sigma_2)^2 + (\sigma_2 - \sigma_3)^2 + (\sigma_3 - \sigma_1)^2\right]$$
$$J_3 = \frac{1}{3}(s_1^3 + s_2^3 + s_3^3) = s_1 s_2 s_3$$

Equation 3-17

$I_1, I_2, I_3, J_1, J_2,$ and J_3 are all scalar invariants, which have properties independent of the coordinate axes. To conveniently express the failure function geometrically, $I_1, J_2,$ and J_3 invariants are often used.

3.4.1.2.1 Geometric meaning of the three stress invariance
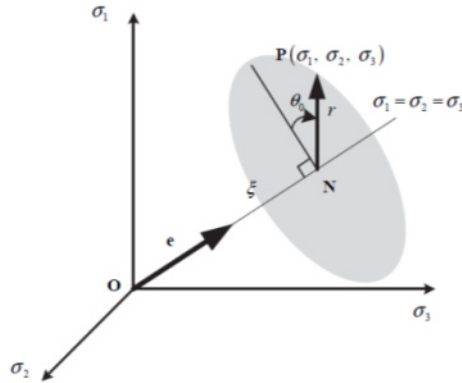
Figure 3-2 Stress state definition in principle stress state (Manual Midas GTS NX)

Vector **OP** can be defined when point **P**=$(\sigma_1, \sigma_2, \sigma_3)$ is expressed as an arbitrary stress state in the principal stress space, as shown in **Figure 3-2**, Vector **OP** can be divided into vector **ON**, which follows the hydrostatic pressure axis; and vector **NP**, which exists in the deviatoric plane perpendicular to the hydrostatic pressure axis. Their size is as follows:

$$|ON| = \xi = \frac{1}{\sqrt{3}} I_1$$
$$|NP| = r = \sqrt{2J_2}$$

Equation 3-18

Vector **NP** needs to be rotated by θ_0 in the σ_1 axis to define point **P** on the deviatoric plane.

Here, θ_0 is called the similarity angle and its equation is as follows:

$$\theta_0 = \frac{1}{3} cos^{-1}(\frac{3\sqrt{3}}{2}\frac{J_3}{J_2^{3/2}})$$

Equation 3-19

Here, θ_0 has the following range:

$$0 \leq \theta_0 \leq \frac{\pi}{3}$$

Equation 3-20

For numerical analysis, it is more convenient to use Lode's angle θ rather than θ_0 and it can be defined using the following equation:

$$\theta = \frac{1}{3}\sin^{-1}\left[-\frac{3\sqrt{3}}{2}\frac{J_3}{J_2^{3/2}}\right]$$

Equation 3-21

Here, $\theta = \theta_0 - \frac{\pi}{6}$ and has the following range:

$$-\frac{\pi}{6} \leq \theta \leq \frac{\pi}{6}$$

Equation 3-22

It is often more convenient to express the principal stress as an invariant stress when defining the failure function of the material, and it can be rearranged using Lode's angle to give the following equation:

$$\begin{Bmatrix}\sigma_1\\\sigma_2\\\sigma_3\end{Bmatrix} = \frac{2\sqrt{J_2}}{\sqrt{3}}\begin{Bmatrix}\sin(\theta + \frac{2}{3}\pi)\\\sin(\theta)\\\sin(\theta + \frac{4}{3}\pi)\end{Bmatrix} + \frac{I_3}{3}\begin{Bmatrix}1\\1\\1\end{Bmatrix}$$

Equation 3-23

3.4.2   Formulation of plastic behaviors

Plastic materials display permanent deformation on structures even after the external load is removed, unlike elastic materials. To express such behavioural properties, strain is formulated following additive decomposition, which divides strain into elastic and plastic components, as shown below:

$$\varepsilon = \varepsilon^{el} + \varepsilon^{pl}$$

Equation 3-24

where ε is the total strain, ε^{el} and ε^{pl} are the elastic and plastic strains respectively.

Because Hook's law defines the relationship between deformation and stress in the elastic region, applying this to **Equation 3-24** and rearranging gives the following equation for stress:

$$\sigma = D\varepsilon^{el} = D(\varepsilon - \varepsilon^p)$$

Equation 3-25

where σ is stress vector and D is material stiffness matrix.

The failure criterion defines the plasticity criteria and can be defined differently depending on the material properties such as soil, steel or concrete. The material failure criterion can be modelled in function form using various experiments on the material. Generally, this function has variables that represent stress and hardening, and can be expressed as follows:

$$f(\sigma, \kappa) = 0$$

Equation 3-26

where f is the failure function and κ is hardening parameter.

If the failure function f is equal to or smaller than '0' (zero), plastic flow does not occur and if f is larger than '0', plastic flow occurs.

3.4.2.1 **Plastic flow rule**

Material failure induces plastic flow, and this plastic flow causes stress redistribution to maintain the equilibrium state of the material. The plastic flow calculation is done in nonlinear form and the increment form is generally used for formulation. The general values used for calculating the plastic flow in plasticity analysis for materials are the incremental stress direction and plastic strain increment direction. The incremental stress direction is as follows:

$$n_i = \frac{\partial f_i}{\partial \boldsymbol{\sigma}}$$

Equation 3-27

where $\boldsymbol{n}$ is vector representing the stress increment direction perpendicular to the failure surface and i is number of failure functions.

The plastic strain increment can be divided into the size and directional components using Koiter's law as follows:

$$\dot{\boldsymbol{\varepsilon}}^p = \sum_{i=1}^{n} \dot{\lambda}_i \frac{\partial g_i}{\partial \boldsymbol{\sigma}} = \sum_{i=1}^{n} \dot{\lambda}_i \, \boldsymbol{m}_i$$

Equation 3-28

Here, g is the plastic potential function, which can be expressed as·

$$f(\boldsymbol{\sigma}, \boldsymbol{\kappa}) = 0$$

Equation 3-29

using stress and hardening variable $\boldsymbol{\kappa}$, generally obtained from material tests. $\dot{\lambda}_i$ is the plastic multiplier, and it needs to satisfy the following Kuhn-Tucker condition:

$$f \le 0, \dot{\lambda}_i \ge 0, \dot{\lambda}_i f = 0$$

Equation 3-30

From the conditions above, plastic flow does not occur when the failure function f is smaller than 0 and $\dot{\lambda}_i$ is always 0. When plastic flow occurs ($\dot{\lambda}_i$ is larger than 0), the failure function is always 0. $\boldsymbol{m}$ is the vector that defines the plastic strain increment in **Equation 3-28**. Here, the method of defining the plastic strain increment by $\frac{\partial f}{\partial \sigma}$, which uses the failure function f and not the plastic potential function g, is called the associated flow rule and the method which uses the plastic potential function to define the plastic strain increment direction by $\frac{\partial g}{\partial \sigma}$ is called the non-associated flow rule. Using the non-associated flow rule on a material model can suppress the excessive cubical expansion phenomena due to the discord between the stress direction and strain direction. However, the amount of calculation increases because the stiffness matrix is asymmetric and an asymmetric solver needs to be used.

The hardening variable··used for strain hardening can be defined using the dimensionless equivalent plastic strain as shown below:

$$\kappa = \sqrt{\frac{2}{3} (\boldsymbol{\varepsilon}^p)^T \boldsymbol{Q} \boldsymbol{\varepsilon}^p}$$

Equation 3-31

Here,

$$\boldsymbol{\varepsilon}^p = \begin{Bmatrix} \varepsilon_{xx}^p \\ \varepsilon_{yy}^p \\ \varepsilon_{zz}^p \\ \gamma_{xy}^p \\ \gamma_{yz}^p \\ \gamma_{zx}^p \end{Bmatrix}, \quad \boldsymbol{Q} = \begin{bmatrix} 1 & 0 & 0 & 0 & 0 & 0 \\ 0 & 1 & 0 & 0 & 0 & 0 \\ 0 & 0 & 1 & 0 & 0 & 0 \\ 0 & 0 & 0 & 1/2 & 0 & 0 \\ 0 & 0 & 0 & 0 & 1/2 & 0 \\ 0 & 0 & 0 & 0 & 0 & 1/2 \end{bmatrix}$$

Equation 3-32

3.4.2.2   **Stress return method**

3.4.2.2.1 Implicit backward Euler method
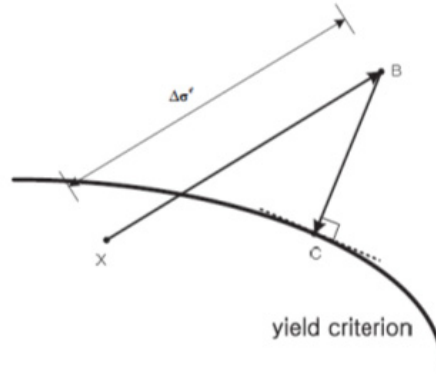
Figure 3-3 Implicit backward Euler method (Manual Midas GTS NX 2014)

As shown in **Figure 3-3**, the implicit backward Euler method can be expressed using the following equation:

$$\boldsymbol{\sigma}_C = \boldsymbol{\sigma}_B - \Delta\lambda \boldsymbol{D}\boldsymbol{m}_c \qquad \textbf{Equation 3-33}$$

Because the unknown C values exist on both sides of **Equation 3-33**, the concept of residual vectors $\boldsymbol{r}$ is introduced to find the value using repeated analysis:

$$\boldsymbol{r} = \boldsymbol{\sigma}_C - (\boldsymbol{\sigma}_B - \Delta\lambda \boldsymbol{D}\boldsymbol{m}_c) \qquad \textbf{Equation 3-34}$$

The residual vector **r** converges to 0 when the final stress state lies on the failure surface. The new residual vector $\boldsymbol{r}_{new}$ for recursive calculations using the first order Taylor expansion can be defined using the following equation:

$$\boldsymbol{r}_{new} = \boldsymbol{r}_{old} + \dot{\lambda}\boldsymbol{D}\boldsymbol{m} + \Delta\lambda \boldsymbol{D}\frac{\partial \boldsymbol{m}}{\partial \boldsymbol{\sigma}}\dot{\boldsymbol{\sigma}} \qquad \textbf{Equation 3-35}$$

Because the residual vector is $\boldsymbol{r}_{new} = \boldsymbol{0}$ for the converged final stress, substituting this into **Equation 3-35** and rearranging for $\dot{\boldsymbol{\sigma}}$ gives,

$$\dot{\boldsymbol{\sigma}} = -(\boldsymbol{I} + \Delta\lambda \boldsymbol{D}\frac{\partial \boldsymbol{m}}{\partial \boldsymbol{\sigma}})^{-1}(\boldsymbol{r}_{old} + \dot{\lambda}\boldsymbol{D}\boldsymbol{m}) = -\boldsymbol{R}^{-1}(\boldsymbol{r}_{old} + \dot{\lambda}\boldsymbol{D}\boldsymbol{m}) \qquad \textbf{Equation 3-36}$$

Also, using the 1st order Taylor expansion on the failure function gives the following equation,

$$f_{new} = f_{old} + \frac{\partial f}{\partial \boldsymbol{\sigma}}\dot{\boldsymbol{\sigma}} + \frac{\partial \kappa}{\partial \boldsymbol{\sigma}}\dot{\kappa} = f_{old} + \boldsymbol{n}^T\dot{\boldsymbol{\sigma}} + h\dot{\lambda} = 0 \qquad \textbf{Equation 3-37}$$

Substituting **Equation 3-37** into equation **Equation 3-36** and rearranging for $\dot{\lambda}$ gives the following equation:

$$\dot{\lambda} = \frac{f_{old} - \boldsymbol{n}^T\boldsymbol{R}^{-1}\boldsymbol{r}_{old}}{h + \boldsymbol{n}^T\boldsymbol{R}^{-1}\boldsymbol{D}\boldsymbol{m}} \qquad \textbf{Equation 3-38}$$

3.4.2.2.2 The cutting plane method
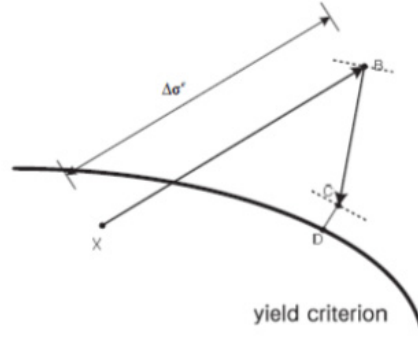
Figure 3-4 The cutting plane method (Manual Midas GTS NX 2014)

Considering **Figure 3-4**, the cutting plane method can be defined as follows,

$$\sigma_C = \sigma_X - \Delta\sigma^e - \Delta\lambda Dm \qquad \text{Equation 3-39}$$

Defining the stress return direction above at point B in the perpendicular direction modifies **Equation 3-39** as follows:

$$\sigma_C = \sigma_B - \Delta\lambda Dm_B \qquad \text{Equation 3-40}$$

Also, using the 1st order Taylor expansion on the incremental function gives the following equation,

$$f_C = f_B + \frac{\partial f}{\partial \boldsymbol{\sigma}}\Delta\sigma + \frac{\partial \kappa}{\partial \boldsymbol{\sigma}}\Delta\kappa = f_B - \Delta\lambda n_B Dm - \Delta\lambda h = 0 \qquad \text{Equation 3-41}$$

Hence, the plastic multiplier increment $\Delta\lambda$ is as follows,

$$\Delta\lambda = \frac{f_B}{n_B Dm_B + h} \qquad \text{Equation 3-42}$$

3.4.2.3   Constitutive equation

The plastic constitutive equation can be composed as follows. The small stress increment is determined by the elastic part of the strain increment vector, which is based on Hooke's law.

$$\dot{\sigma} = D(\dot{\varepsilon} - \dot{\varepsilon}^p) = D\dot{\varepsilon} - \dot{\lambda}Dm \qquad \text{Equation 3-43}$$

Because the current stress always needs to be positioned on the failure surface, the consistency condition $\dot{\lambda}\dot{f} = 0$ needs to be satisfied. Rearranging equation **Equation 3-43** for the small strain increment gives the following equation:

$$\dot{\sigma} = \left(D - \frac{Dmn^T D}{h + n^T Dm}\right)\dot{\varepsilon} = D^{ep}\dot{\varepsilon} \qquad \text{Equation 3-44}$$

where **D**$_{ep}$ in is called the continuum tangent stiffness matrix.

When using the consistent tangent stiffness matrix for the Newton-Raphson recursive formula, it converges faster than when **Equation 3-44** is used because of the second order convergence property. This second order convergence property can be obtained from the following process. First, differentiating **Equation 3-43** gives the following equation:

$$\dot{\sigma} = D\dot{\varepsilon} - \lambda Dm - \Delta\lambda D\frac{\partial m}{\partial\sigma}\dot{\sigma} - \Delta\lambda D\frac{\partial m}{\partial\kappa}\frac{\partial\kappa}{\partial\lambda}\dot{\lambda}$$

Equation 3-45

where $\Delta\lambda$ is the change in λ.

Equation 3-45 can be rearranged as follows:

$$A\dot{\sigma} = D\dot{\varepsilon} - \lambda D\bar{m}$$

Equation 3-46

where,

$$A = I + \Delta\lambda D\frac{\partial m}{\partial\sigma}$$

Equation 3-47

and,

$$\bar{m} = m + \Delta\lambda D\frac{\partial m}{\partial\kappa}\frac{\partial\kappa}{\partial\lambda}$$

Equation 3-48

If, $H = A^{-1}D$, Equation 3-46 can be rearranged as follows,

$$\dot{\sigma} = H(\dot{\varepsilon} - \lambda\bar{m})$$

Equation 3-49

If Equation 3-49 is rearranged for the total strain term using the consistency condition, the following equation can be obtained:

$$\dot{\sigma} = (H - \frac{H\bar{m}n^T H}{h + n^T H\bar{m}})\dot{\varepsilon} = C^{ep}\dot{\varepsilon}$$

Equation 3-50

C^{ep} in Equation 3-50 is so called the consistent tangent stiffness matrix.

3.4.3   Tresca failure criterion

The Tresca criterion was originally developed to be used on failure conditions of metallic materials. In geotechnical analysis, it is often used to simulate the ground material behaviour for undrained conditions. The failure condition for this criterion can be expressed using the uniaxial compression strength (σ_y) considering the ordered principal stresses ($\sigma_1 < \sigma_2 < \sigma_3$), as shown below.

$$|\sigma_3 - \sigma_1| = \sigma_y = 2S_u$$

Equation 3-51

In the case of soil under undrained condition, the failure is governed by two-times of the undrained strength. Equation 3-51 can be expressed using stress invariant J_2 and θ_0 (for $0° \le \theta_0 \le 60°$) as follows,

$$\sigma_1 - \sigma_3 = \frac{1}{\sqrt{3}}\sqrt{J_2}\left[cos\theta_0 - \cos{(\theta_0 + \frac{2}{3}\pi)}\right] = \sigma_y$$

Equation 3-52

Rearranging the former equation,

$$f(J_2, \theta_0) = 2\sqrt{J_2}\sin\left(\theta_0 + \frac{1}{3}\pi\right) - \sigma_y = 0$$

Equation 3-53

Or, it can be expressed using the terms, I_1, J_2 and θ_0 (for $-\frac{\pi}{6} \le \theta_0 \le \frac{\pi}{6}$)

$$f(J_2, \theta_0) = \frac{2}{\sqrt{3}}\sqrt{J_2}\left[sin\left(\theta + \frac{2}{3}\pi\right) - \sin\left(\theta + \frac{4}{3}\pi\right)\right] - \sigma_y = \sqrt{J_2}cos\theta - \sigma_y = 0$$

Equation 3-54
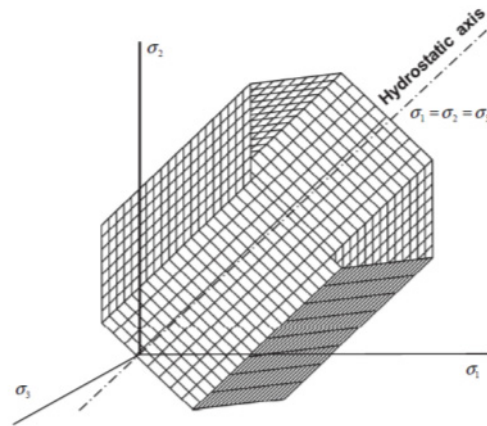
Figure 3-5 Tresca failure surface shape in principle stress space (Manual Midas GTS NX)

The effects of hydrostatic pressure on the failure plane are not considered for this criterion and so, it's unrelated to I_1. The Tresca failure criterion is a hexagonal column parallel to the hydrostatic axis in the principal stress space, as shown in **Figure 3-5**, and is expressed as a regular hexagon in the deviatoric plane, as shown in **Figure 3-6a**.

(a)   (b)
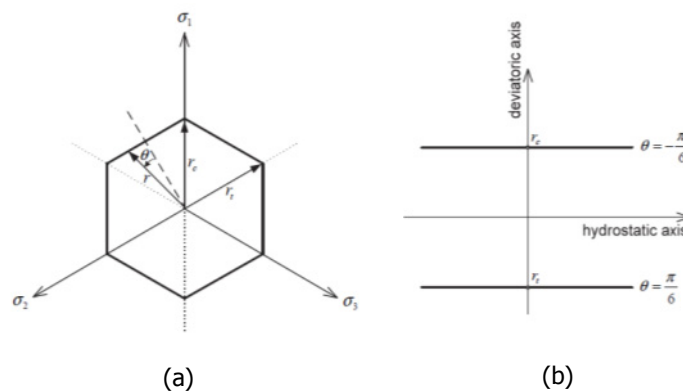
Figure 3-6 (a) failure surface shape in π plane and (b) failure surface shape in the meredian plane for θ= -π/6 (Manual Midas GTS NX)

According to the experimental results, the shear strength of the saturated soil is unrelated to I_1 for undrained loading. The Tresca model can obtain appropriate results under these conditions.

As this model is perfectly plastic, there is no hardening/softening law required. Moreover, as this model is intended to study the undrained behaviour of saturated clay, it should predict zero volumetric strains (i.e. on yield surface), both the elastic and plastic components of volumetric strain must be zero. A convenience choice is to assume associated plastic flow and adopt the Tresca failure function as plastic potential. This causes the vector of incremental plastic strain is normal to the yield surface (**Figure 3-7**) and implies no incremental plastic direct strain (Potts, 1990).

3.5   Typical results of Unconsolidated-Undrained (UU) triaxial test

For the most engineering practices, triaxial test has been considered in order to define better soil parameters that are used for analysis. There are two distinguish tests in any triaxial test. The first phase is consolidation phase, during which the cell pressure is increase. This provides uniform confining stresses on the specimen equal to the minor principle stress, σ_3. During this phase the soil might be allowed to consolidate or not, depending on the type of the test being performed. The second phase of the test is fissure or shear phase. During this test a load is applied through the piston located on the top of the system. This load increases the stresses at the top of the specimen. Since there are no shear stresses,

23

either the top or the side of the specimen, these are the principle plane. So the major principle stress, σ_1, is applied to the top of the specimen and the cell pressure provides minor principle, σ_3, to the side of the specimen. The vertical stress is gradually increased until the specimen failures.

If we consider Unconsolidated-Undrained (UU) triaxial test, we do not measure the pore pressure and do not compute the effective stresses. The results of the test are in terms of total stresses. The purpose of UU test is to determine the undrained shear strength S_u. The drainage valve is closed in UU tets. Initially there is no initial stress, so the Mohr Coulomb appears as point at the origin of the diagram. When we apply the confined stress during consolidation phase, the Mohr Circle remains a point. It is because σ_1 and σ_3 about equal to the cell pressure. However, the Mohr Circle (a point) moves to the right along x-axis, as the cell pressure increases. Once the consolidation phase completes, the shear phase starts by increasing the vertical stress, σ_1, applied to the specimen. The minor principle σ_3 does not change as we shear the specimen. We continue to increase the vertical stress until the soil fails. Again the maximum principle stress at failure is σ_{1f}. In addition, we have the undrained shear strength S_u (sample 1). Because the drainage valve was closed during the consolidation phase, no consolidation occurred and the soil does not gain any strength during this phase. Therefore, the undrained shear strength under confining stress is no greater than the undrained shear strength under unconfining stress in the same soil. Similarly if we conduct another test (sample 2) on identical specimen, but raise the σ_3, the soil would not gain any strength, because no consolidation is allowed. This test gave the same results as the previous test. If we plot the shear strength envelope of the tests, we will have zero slope and intersect with y-axis at S_u. This is known as $\varphi = 0$ condition. In general, saturated clay loaded under undrained condition fails under $\varphi = 0$ condition. See **Figure 3-7**.
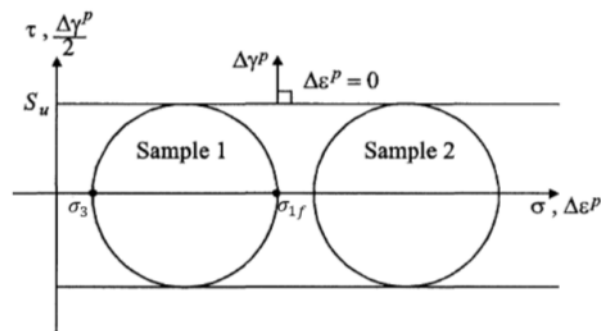
Figure 3-7 Mohr's circle of total stress test (e.g. UU triaxial test).

A failure criterion is then adopted which relates the undrained strength, S_u, to the diameter of the Mohr's circle at failure. To complete the model it is only necessary to define the elastic parameters. There should be no elastic volumetric strains, therefore, $v \sim 0.5$. In this case the Tresca model can therefore be considered and defined by specifying the undrained strength, S_u, and the undrained Young's modulus, E_u.

3.6   Axisymmetrical solid elements

3.6.1   Coordinate system
Various coordinate systems (**Figure 3-8**) are needed to use the finite element method to appropriately model and correctly analyze the given problem. For axisymmetrical model, cylindrical coordinate system is used on GTS NX.
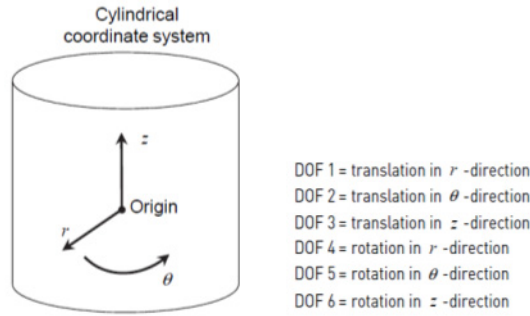
Figure 3-8 Cylindrical coordinate system and its degree-of-freedoms (DOFs) in axysymmetric element

GTS NX uses various coordinate systems for ground or structural modelling and analysis as shown on **Figure 3-9**.

Type of coordinate system	Explanation
GCS : global coordinate system	Coordinate system that expresses the entire model using the same standard. Rectangular coordinate system
NDCS : nodal displacement coordinate system	Coordinate system that describes the nodal motion direction. Rectangular/Cylindrical coordinate system
ECS : element coordinate system	Coordinate system determined by the position of the nodes that make up the element. Rectangular coordinate system
MCS : material coordinate system	Coordinate system that defines the direction of the material applied on the element. Rectangular/Cylindrical coordinate system
ERCS : element result coordinate system	Coordinate system that prints the element results. Rectangular/Cylindrical coordinate system
EFCS : element formulation coordinate system	Coordinate system used for finite element formulation. Same as GCS or element coordinate system

Figure 3-9 Various coordinate systems in GTS NX

In the case of axisymmetrical problem, GTS NX uses Material Coordiante System for ground analysis as shown on **Figure 3-10**.
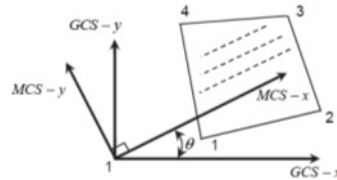
Figure 3-10 Definition of material axis for axisymmetrical soild element (Manual Midas GTS NX)

3.6.2   Node and DOFs

Nodes and elements determine the size and shape of the finite element model and are the starting point of all analyses. A model defined by nodes and elements is the same as physical phenomena expressed using numerical equations in matrix form. The variables that affect the matrix equation are displacement, rotation, pore pressure and other physical quantities, which are called degrees of freedom (DOF). Each node has a coordinate system that describes the direction of motion. This is called the nodal displacement coordinate system. All DOFs mentioned above follow the coordinate system direction assigned to the nodes, and all nodes describe the direction of motion with reference to the global coordinate system.

Axisymmetric solid elements have displacement DOF in the Global Coordinate System x (radial direction) and y directions.

$$\boldsymbol{u_i} = \{u_i v_i\}^T$$

Equation 3-55

25

3.6.3 Stress and strain

Axisymmetric solid elements consider strain and stress defined on the GCS, and the components are as follows:

$$\boldsymbol{\sigma} = \begin{Bmatrix} \sigma_{xx} \\ \sigma_{\theta\theta} \\ \sigma_{yy} \\ \tau_{yx} \end{Bmatrix}, \boldsymbol{\varepsilon} = \begin{Bmatrix} \varepsilon_{xx} \\ \varepsilon_{\theta\theta} \\ \varepsilon_{yy} \\ \gamma_{yx} \end{Bmatrix}$$

Equation 3-56
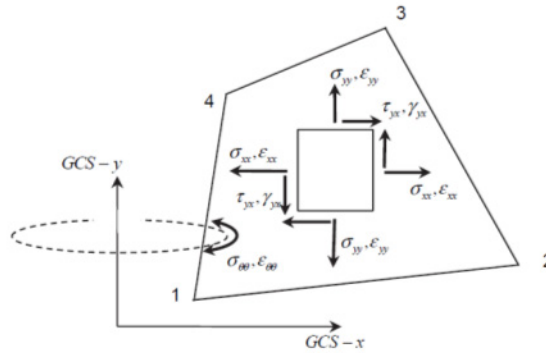
Figure 3-11 Stress strain of an axisymmetric element

3.6.4 Load

The loads applied to axisymmetric solid elements are as follows:

Load type	Explanation
Self-weight due to gravity	Applied to the material density
Pressure load	Distributed load applied on an element side (Load acting on the outer surface of a structure when considering axisymmetry.)
Water pressure load	Distributed load applied on an element side Size determined by pore pressure/water level (Load acting on the outer surface of a structure when considering axisymmetry.)
Element temperature load	Element temperature that causes deformation of the axissymetric section
Prestress/Initial equilibrium force	Initial stress of an element and the corresponding equilibrium force

Table 3-1 Loads applied on axisymmetric element

3.6.5 Element results

On GTS NX, the results of an axisymmetric solid element are printed in the user defined reference coordinate system. The selectable systems are the ECS, MCS and arbitrary coordinate system. The component of element result has the x, y direction and a circumferential direction of θ.

Result Article		Explanation
Stress	Stress component	Position : vertex/element center σ_{xx}, σ_{yy}, $\sigma_{\theta\theta}$, τ_{xy}
	Principal stress	Position : vertex/element center P_1, P_3
	Von-Mises stress	Position : vertex/element center σ_v
	Max shear stress	Position : vertex/element center τ_{max}
Strain	Strain component	Position : vertex/element center ε_{xx}, ε_{yy}, $\varepsilon_{\theta\theta}$, γ_{xy}
	Principal strain	Position : vertex/element center E_1, E_3
	Von-Mises strain	Position : vertex/element center ε_v
	Max shear strain	Position : vertex/element center γ_{max}

Table 3-2 Results article of axisymmetric solid elements (Manual Midas GTS NX)

3.6.6   Non linear analysis

Geometric nonlinearity can be considered for axisymmetric solid elements and material nonlinearity can be considered for elastic and nonlinear elastic materials. The additional result articles for nonlinear material usage are listed in the table below. The material states are expressed using symbols.

Result article		Explanation
Stress	Equivalent stress	Position : Integral point Calculated according to plastic model, σ_{eq}
	Material status	Position : Integral point Elastic: - Plastic/Nonlinear elastic: $\bigcirc$ Unloading/reloading: $\oplus$ Tension failure: $\oplus$ Cap failure: $\ominus$
Strain	Equivalent strain	Position : Integral point Calculated according to plastic model, ε_{eq}
	Effective plastic strain	Position : Integral point e_p

Table 3-3 Nonlinear analysis result article of axisymmetric solid elements

3.7   Numerical scheme and formulation

The detail scheme and formula can be further found in the manual.

4. Set up 2D Numerical modelling of extrusion test

4.1 Introduction

Axisymmetric FEM model of the triaxial extrusion test has been built and examined thanks to Midas GTS NX 2014. The magnitude of parameters that is a priori chosen is typically for kaolin clay (Burns *et al.*, 2010) with a constant ratio of the initial stress and undrained shear strength, σ_0/S_u, up of 6.0. First of all, a preliminary analysis has been carried out in order to investigate any possible effect due to dimension of sample by varying: (1) the diameter of the specimen by keeping the diameter of the cavity at constant; (2) the height of the cavity by keeping the diameter of the specimen and the cavity at constant and (3) and the total height of the cell by keeping the others dimensions at constant (see **Figure 4-1**). One unique dimension of the specimen will be chosen for further study. The chosen dimension must concern any possible scale effect on the results that will be investigated in this preliminary analysis. All the results here will be shown are in terms of the characteristic curve (stress-displacement curve) whereas extrusion or displacement at the cavity is averaged.

4.2 Idealization

4.2.1 2D Axially symmetric model

In this study a two-dimensional axially symmetric model of the extrusion tests is developed. A sketch of the model is shown in **Figure 4-1**.
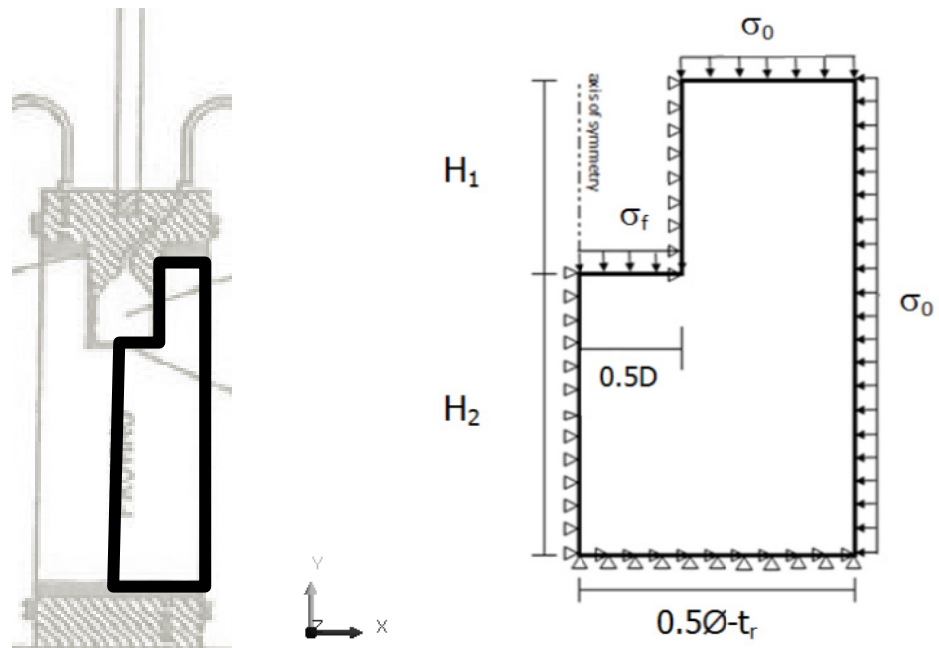
Figure 4-1 A sketch of 2D-Axisymmetrical model of extrusion tests. Edges: H_1 & H_2. Internal and external diameter: D and Ø. t_r is the thickness of the circular ring. Pressure: axial and radial pressure, σ_0 and face pressure, σ_f.

4.2.2 Boundary conditions

For the 2D FEM extrusion model, it is assumed that that both displacements for all nodes along the bottom of the mesh are zero (rough condition) as shown in **Figure 4-1b**. Consequently, nodal reactions (forces) will be generated in both the horizontal and vertical directions as a result of the analysis. In fact, whether

the bottom was assumed to be rough or smooth, would not give any effect since the dimension would be chosen in order to avoid any possible boundary effect on the results, if edge H_2 is sufficiently high (4.4.2.2).

On the vertical boundaries (along the axis of symmetry as edge H_2 and considering the circular ring as edge H_1) the horizontal displacement and vertical force have been assumed to be zero (**Figure 4-1b**). By assuming that the vertical force equals to zero it implies that there can be no vertical shear stress on these boundaries. Therefore, the nodes are free to move in the vertical direction. As another result of the analysis, however, horizontal reactions will be generated at the nodes.

Vertical pressures (on the top boundary as radial pressure and on the extrusion chamber as face pressure) are applied immediately. In addition any horizontal nodal forces are assumed to be zero. In fact, these boundary conditions are similar to a model of a smooth flexible circular footing. Similar principle applied also to horizontal pressure that is applied immediately on the mesh boundary located on the outer radius of the model. In this case, vertical nodal forces are assumed to be zero.

4.2.3   Idealization

4.2.3.1   **Material**
The material is assumed to be built perfectly homogeneous. The mechanical response of the material is assumed to be isotropic elastic perfectly plastic. The material behavior is under undrained conditions (the undrained strength, S_u, is the unique constitutive parameter related to the material strength) by neglecting viscosity behavior, since in practice the rate of advance of the tunnel is maintained to be sufficiently fast (2.3.2.2).

4.2.3.2   **Rigid lining**
The circular ring being extruded to the sample is assumed to be perfectly rigid. Therefore, the influence of its stiffness on the system response is disregarded. By considering a very stiff lining, as consequence the radial soil movement is equal to the soil movement gives upper bound to lining pressure as illustrated in **Figure 4-2**.
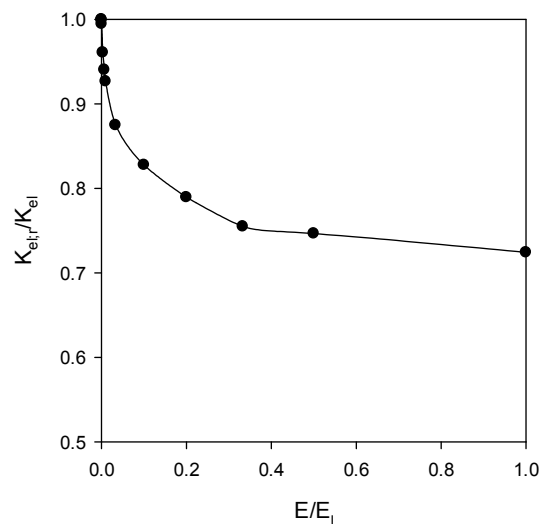
Figure 4-2 Variation of $K_{el}/K_{el,r}$ with the stiffness of the tunnel lining (di Prisco *et al.*, 2015)

where is K_{el} the elastic slope on the *RLSR-Ω_f* (see **Equation 4-3** and **Equation 5-1**) plane for non-rigid lining and $K_{el;r}$ is the elastic slope on the *RLSR-Ω_f* plane for rigid lining.

4.2.3.3   **In comparison with 3D tunnel model**
The former assumptions are quite similar to those of the 3D FEM models (di Prisco *et al.*, 2015). Actually, some differences in assumption of both models do exist. In the case of 2D FEM extrusion test, the

diameter of the extrusion chamber is irrelevant since the applied pressure, σ_0, was superior. This is not strong assumption since, in this study, deep tunnel is considered where the geometrical ratio *H/D* (where *H* is the tunnel cover and *D* is the equivalent diameter of the tunnel) is sufficiently large to ensure the development of a local failure mechanism not involving superficial layers (this implies the superficial boundary conditions not influencing the failure mechanism). The other difference with respect to the 3D tunnel model is the shape of the cross-section. In the case of extrusion it will be always in circular, whereas in the 3D numerical model it has a unique shape (**Figure 4-3**) was taken into consideration. This type of shape is the most efficient cross-section considering the usability of tunnels with the least amount of material that would be excavated, because its equivalent diameter was comparable to that of the circular shape, the geometry effect could not affect the mechanical response of the system. Different boundary condition has been applied in both models. In fact, it causes difference in results between two models (see section 5.3.1).

| (a) | (b) |
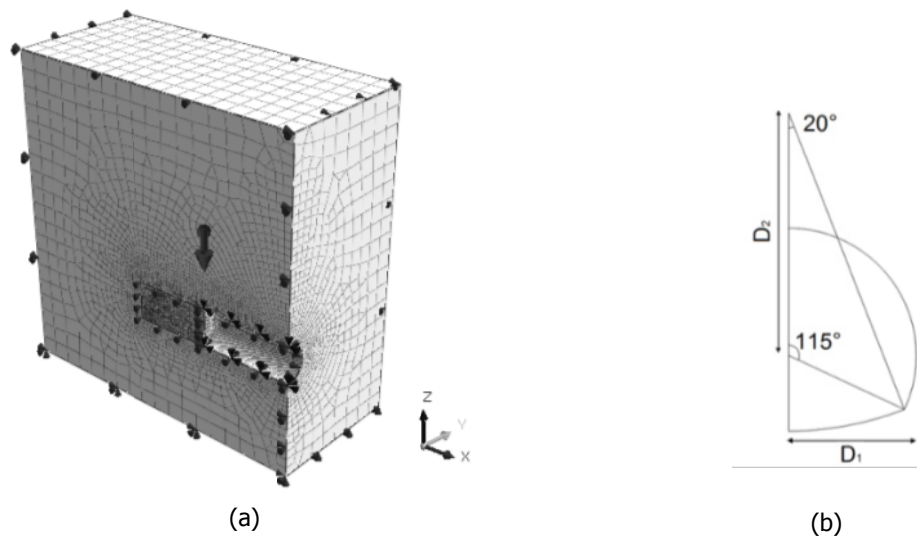
Figure 4-3 (a) the 3D FEM tunnel and (b) the tunnel cross-section (Di Prisco, *et al.*, 2015).

4.2.4   Applied stresses and K₀

Generally, in the standard triaxial test, the coefficient of pressure (K_0) could be expressed as a ratio between the applied radial and axial pressure in terms of effective stress. Since the undrained conditions have been assumed for the present study, therefore, K_0 has been considered in terms of total stress as expressed:

$$K_0 = \frac{\sigma_3}{\sigma_1}$$

Equation 4-1

where, σ_0 is the applied pressure, in which the axial (σ_1) and radial stresses (σ_3) are equal in the case of $K_0 = 1.0$ and σ_f is the stresses on the extrusion chamber or so called stress of the face. The stresses on the extrusion chamber, σ_f, is always equal to the axial stress, σ_1, at any value of K_0.

4.2.5   Phase of analysis

First of all, the axial (σ_1), radial (σ_3) and face stress (σ_f) are equally applied considering confining pressure in the cell (σ_0) in order to have proper state of stresses. Then, the corresponding displacement of the former phase of analysis is redefined so that the extrusion measured on the displacement controlled points starting from zero values during reduction of the face stress. By decreasing progressively the magnitude of the face stress, the average displacement or extrusion is considered of each time steps. The final goal is to

30

plot the correlation between the face stress and the extrusion (the characteristic curve). In practice the value σ_0 is corresponded to the initial horizontal stress at the face as mentioned in **Equation 4-2.**

$$\sigma_0 = K_0[\gamma(H + D/2) + q] \qquad\qquad \text{Equation 4-2}$$

where q is the vertical stress applied on the surface, H is the depth of soil above the centre of the tunnel axis, D is diameter of the tunnel, γ is the unit weight of the soil, and K_0 is The coefficient of lateral earth pressure.

There are some different procedures considering phase analysis in the 2D FEM extrusion test model and the 3D FEM tunnel. In the 3D FEM tunnel, the initial state of stress is obtained by applying gravity in a medium initially assumed to be elastic (**Figure 4-4a**). The front is assumed to be rigid, exactly as the lining is. In the other hand, in the case of 2D FEM extrusion test, the initial state of stress is uniform, since the applied stresses are confined and acting surrounding the specimen (**Figure 4-4b**). The removal of the material of the tunnel front is simulated by transforming the kinematic control at the tunnel front into a static control of the pressure there applied. The initial linear distribution of the horizontal stress at the front is then progressively reduced. The only different in the case of 2D FEM extrusion test, is that the distribution of the horizontal stress at the front is uniform, due to the confining pressure applied on the sample.

(a)   (b)
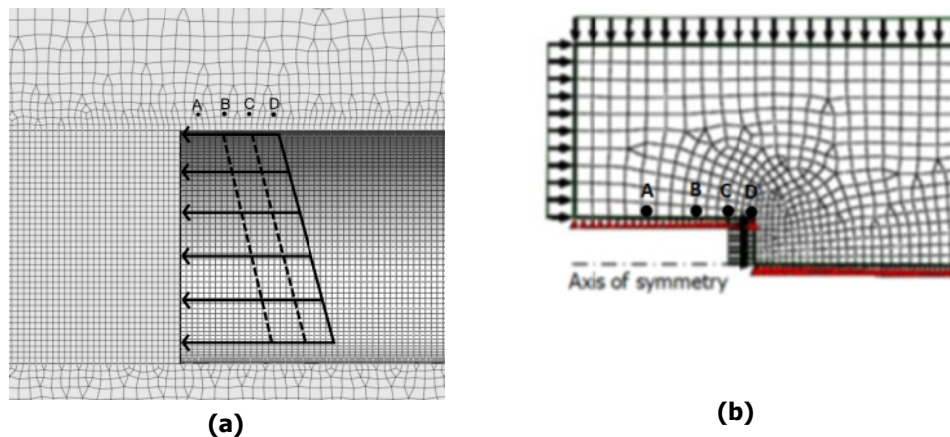
Figure 4-4 Load-displacement control by considering progressive reduction in the stress on the front (a) of the tunnel in the 3D tunnel model and (b) of the face of extrusion chamber in the 2D FEM extrusion test.

The non-linear problem is solved by using the Newton-Raphson method and the convergence of the iterative solution is determined by assessing simultaneously the force (tolerance 10^{-3}), the displacement (tolerance 10^{-3}) and the energy norm ratio (tolerance 10^{-6}) (Midas GTS NX 2014).

4.3   The characteristic and normalized curve

Lombardi (1974) has studied stress-strain relationship of the core, particularly at the face, considering given circular cavity and hydrostatic stress by means of a characteristic lines method. These lines gave possibility to define relationship of the pressure and radial deformation of the core ahead of the face whether in the elastic range (stable face) or in the elasto-plastic range (stable face in short term or unstable). Similar principle, the behavior category, particularly at the face, was also introduced by means of the characteristic lines for an extrusion test (Lunardi, 1995 & 2000). Moreover, some of those authors, in particular Vermeer *et al.* (2002), Yoo (2002) and Kirsch (2009) numerically reproduced a characteristic curve having stress-displacement relationship at face and also experimentally obtained by Chambon and Corté (1994).
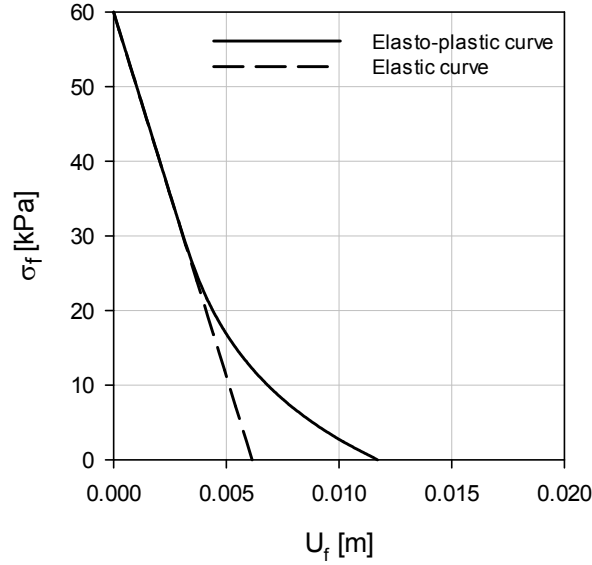
Figure 4-5 Elastic and elasto-plastic characteristic curves obtained from 2D FEM extrusion test with D=10mm, H=108mm, E=80KPa, v=0.495, K₀=1.0, and Sᵤ=30 KPa (elastic curve) and 10 KPa (elasto-plastic curve).

In this study we modify the representation of the characteristic curve by changing the axis: the average face pressure, σ_f, in y-axis and the average displacement at the face, U_f in x-axis. For example, the typical shape of characteristic curve is shown in **Figure 4-5** giving two different responses: the elastic and elasto-plastic. This linear curve was typically curve that can be obtained when the geometry is adequate to avoid any effect from boundary and when the value S_u is much higher with respect to σ_0. Otherwise, the elastic-plastic curve is obtained where irreversibility takes places but the unstable behavior is not totally reached. In general, the shape of the curve is actually governed by the geometry and mesh. Another observation was that the initial linear shape of both curves is coincident. Afterwards, the displacements in the elasto-plastic curve develop faster giving the residual displacement, U_f higher than that of elastic one, $U_{r;el}$. Generally, from **Figure 4-5** we can define three different behaviors: (i) initial part which is linear; (ii) transitional part, where the curvature rapidly increases and (iii) finally a further reduction in the curvature, whether in stable face in short term or unstable (Lombardi, 1974 and Lunardi, 2000).

It is also a very convenient to introduce a normalized curve as shown in (**Figure 4-6**), where on the y-axis the average stress of the front is normalized with respect to its initial value σ_0, so called the Relative Load Sharing Ratio (RLSR),

$$RLSR = \left(1 - \frac{\sigma_f}{\sigma_0}\right)$$

Equation 4-3

whereas on the x-axis the average displacement is normalized (u_σ) with respect to the elastic residual displacement, $U_{r;el}$.

$$u_\sigma = \frac{u_f}{u_{r,el}}$$

Equation 4-4
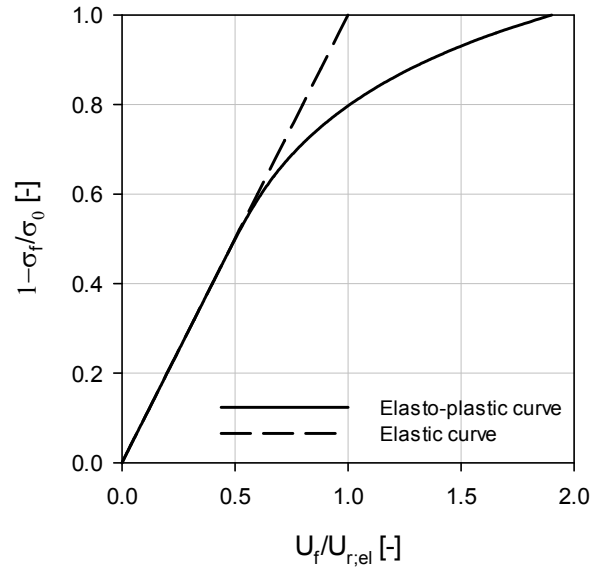
Figure 4-6 Normalization of the characteristic curves of Figure 4-5.

Results of the analysis for the following section consider the characteristic curve and or the normalized characteristic curve.

4.4   Dimension of specimens

The goal of this section is to define the final configuration of the 2D FEM extrusion test, such as diameter and height of the sample and diameter of extrusion chamber to be used for further analysis. This concerns an undrained analysis with the ratio σ_0/S_u of 6.0. A limit of dimension of sample does exist since in practice a standard dimension of sample of the test is rarely found bigger than 50 mm of diameter and 100 mm of height. Moreover, any possible errors in discretization of model are studied considering mesh (geometry and size) and in distortion due to a singularity velocity.

4.4.1   Discretization errors (mesh and singularity velocity)

In some particular cases of numerical modeling care must be taken due to any possible development of displacement singularities due to presence of zone of high distortion (van Langen, 1991) considering soil-structure interaction. It is a fan radiating in different directions at corner point of footing. Two mechanisms shown in **Figure 4-7** imply displacement singularity at the ends of the rigid bodies on cohesive layer in cohesive layer (Cox, 1960 and van Langen, 1991) due to infinitely large of stresses at the edge of the structure as a consequence of the constant displacement of the rigid body (Boussinesq, 1885).

(a)   (b)

Figure 4-7 (a) Singularity velocity at corner point of footing and (b) of rigid buried structure in a cohesive soil mass (Langen, 1991).

It would be possible that this type of problem would occur especially at the corner of extrusion chamber where the circular steel to be extruded within the sample. Apparently, the singularity at the corner of the face of extrusion chamber is not so apparent. This might be due to the fact that the

mechanism of potential slip line involved in these zones would be more confined and limited considering direction of velocity at corner that would appear because of the applied uniform pressure in the system (Langen, 1991 and Potts, 1999). However, this effect seems to be negligible by increasing the number of mesh, since finer mesh would easily incorporate with some theoretical potential slip line solution in comparison with rough mesh. In principal, this process of refinement could be repeated until the results were unaffected by further mesh refinement (Potts, 1999). Simple examples to see the effects of refinement are given in Appendix 1: Bearing capacity of circular footing and Appendix 2: Rough rigid punch penetrating into cohesive soil.

(a)

| (b) | (c) | (d) | (e) |
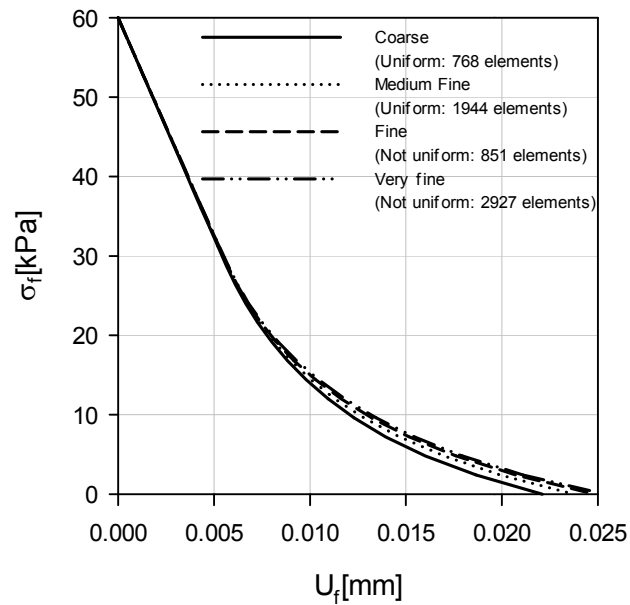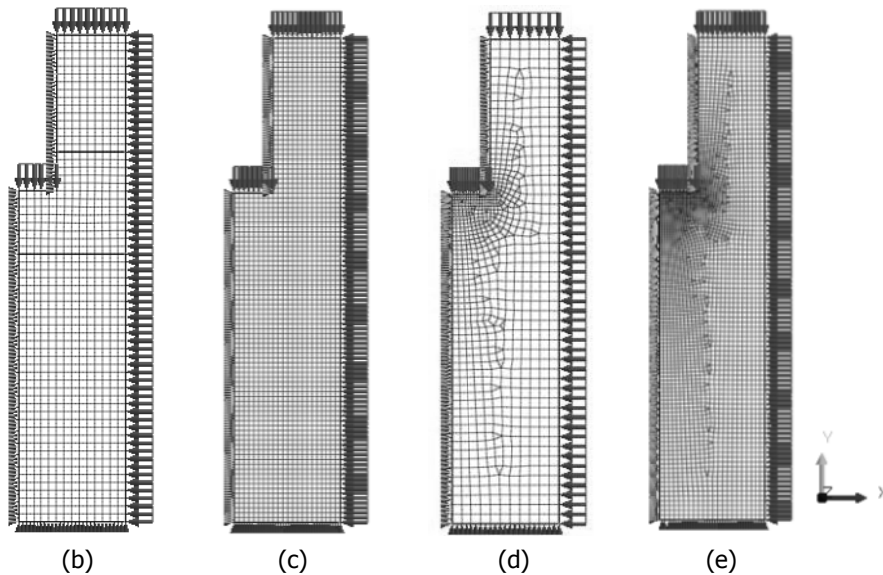
Figure 4-8 (a) Effect of mesh on the characteristic curve. Continuous line: uniform and coarse mesh with 768 elements (b), dotted line: uniform and medium fine mesh with 1944 elements (c), dash line: none uniform and fine mesh closed to face with 851 (d) and dash-dotted line: none uniform and very fine mesh closed to face with 2927 elements (e).

Four models are considered: two uniform models and two non-uniform meshes with concentrated

34

smaller element around face (0.5x0.5 mm). As shown in **Figure 4-8a**, the solution becomes convergent when the model goes to finer mesh. It has been observed that improvement on the results occur when finer mesh is considered, in particular area around the face. Moreover, any model finer than 0.5x0.5 mm (size of elements located close to the face), would give no further improvement on the results or in other word, there would be no big different considering the characteristic curve (see Fine and Very Fine mesh on **Figure 4-8a**). Due to this reason, the model with none uniform and fine mesh closed to face with 851 elements has been considered as the most efficient model.

4.4.2   Investigation of geometry

The internal diameter of the vertical of the vertical cylinder is R, while the total diameter of the sample is 2Ø. It is assumed that the thickness of the steel cylinder would give no effect to the results. The total height of the sample is the sum of H_1 and H_2 (**Figure 4-1**).

Generally speaking, dimension of sample used for triaxial test consists of the total diameter between 50 to 70 mm and height between 100 to 140 mm. In practice a standard dimension of sample of the test is 50 mm of the total diameter and 100 mm of the total height.

In this section, a sequence of analysis was carried out in order to check possible effects of geometry on the results of numerical analysis. In this case, the ratio σ_0/S_u of 6.0 is considered in the analysis. The results shown in the following are in term of the characteristic curve and relationship between the normalized stability factor and the normalized extrusion.

4.4.2.1   **Varying the height of the cavity, H_1**

By varying the height of the cavity, H_1 and keeping the inner and outer diameters at constant value, the characteristic curves do not scatter (**Figure 4-9a**). Moreover, it can be observed that by varying the ratio of H_1/D at least up to 2.0 and by considering any constant value of ratio ø/D, e.g. 3.1 or 4.3, the difference on the result considering elastic and elasto-plastic solutions is negligible (**Figure 4-9b**).

Figure 4-9 (a) Characteristic curve by varying H_1/D with constant $H_2/D=4.3$ and $\sigma_0/S_u=6.0$. Long dash line: ø/D=3.1 and dotted line: ø/D=4.3. (b) U_f versus H_1/D.

In the other hand, different value of ø/D gives different response, in particular elastic solution (**Figure 4-9a**), even though the ratio of H_1/D is kept at constant value. Although the offset of the plastic evolution for ø/D=3.1 and 4.3 are qualitatively comparable as shown in **Figure 4-10**, but it would give effect on the results (see detail in section 4.4.2.3).

(a)   (b)

Figure 4-10 Plastic zone (grey) for constant $H_2/D=4.3$ and $\sigma_0/S_u=6.0$ with varied H_2/D. Left to right: $H_1/D=1.0$, 2.0 and 3.0 respectively. (a) ø/D=3.1 and (b) ø/D=4.3.RLSR=1.0.

4.4.2.2   **Varying H_2**

In the second case, edge H_2 is varied by keeping the others edges at constant value. In this case the ratio $H_1/D=2.0$ is used since varying this edge as shown in the former case gave no significant different on the results (**Figure 4-9**). From the characteristic curve shown in **Figure 4-11a**, the higher the ratio ø/D is, the less the difference on the results by varying H_2/D is. This was true if the ratio ø/D was sufficiently high, e.g., at least when ø/D=4.3, to guarantee no scale effect (**Figure 4-11a**).

(a)   (b)
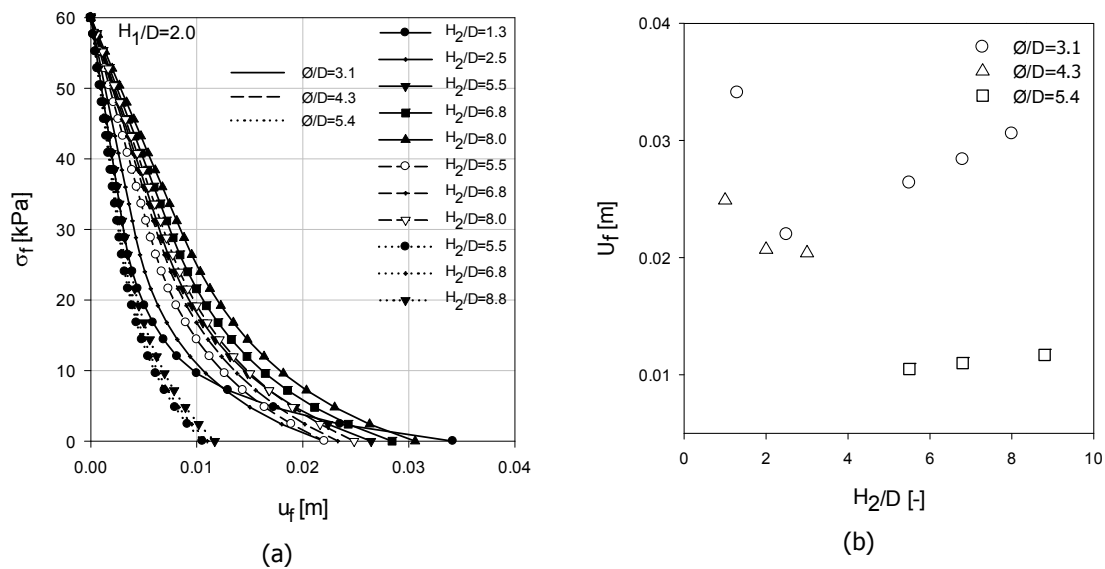
Figure 4-11 (a) Characteristic curve by varying H_2/D with constant $H_1/D=2.0$ and $\sigma_0/S_u=6.0$. Long dash line: ø/D=3.1, medium dash line: ø/D=4.3 and dotted line: ø/D=5.4. (b) U_f versus H_2/D.

Moreover, if we consider the plastic zone around the face of the extrusion, the development of the plastic zone reaches the boundary (where vertical and horizontal displacements are set to zero) and then propagates. This occurs due to the fact that the shear is allowed as the boundary was fixed only on vertical direction. This applies when edge H_2/D was too short, e.g. $H_2/D=1.3$, as shown in **Figure 4-12a-left**. This might give a scale effect on the characteristic line.

36

(a)
Left to right: H_2/D= 1.3, 2.5, 4.3, 5.5 and 6.8 respectively

(b)
Left to right: H_2/D= 5.5, 6.8 and 8.0 respectively

(c)
Left to right: H_2/D= 5.8, 6.8 and 8.8 respectively

Figure 4-12 Plastic zone (grey) for constant $H_1/D=2.0$ and $\sigma_0/S_u=6.0$ with varied H_2/D. (a) ø/D=3.1, (b) ø/D=4.3 and (c) ø/D=5.4.RLSR=1.0.

Similar observation as in the previous case, different value of ø/D gives different response, in particular elastic solution (**Figure 4-11a**), even though the ratio of H_2/D is kept at constant value. Again, qualitatively, the offset of the plastic evolution for different value of ø/D are comparable (**Figure 4-12**), but it gives effect on the results (see detail in section 4.4.2.3).

4.4.2.3 **Varying diameter of sample, ø**

In **Figure 4-13** shows the results when the outer diameter of the sample, ø, is varied while the diameter of the cavity, D, is kept at constant value. It has been observed that when the ratio of ø/D is increased, while H_1/D is kept constant at least up to 4.3, the results would not improve any further, e.g. at least when ø/D= 5.0 (**Figure 4-13b**).

(a)

(b)
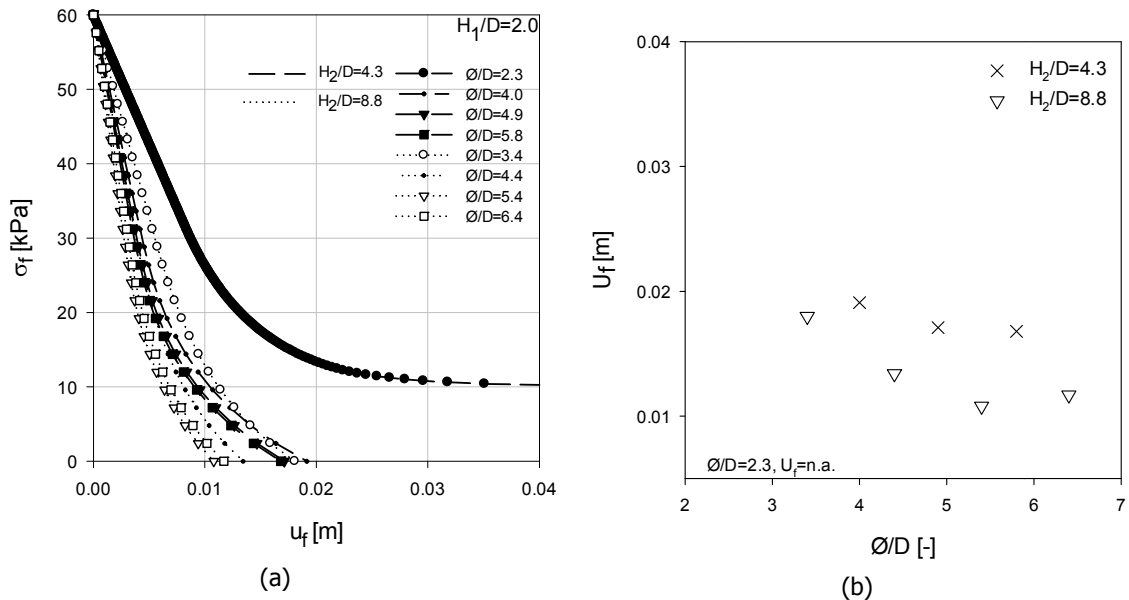
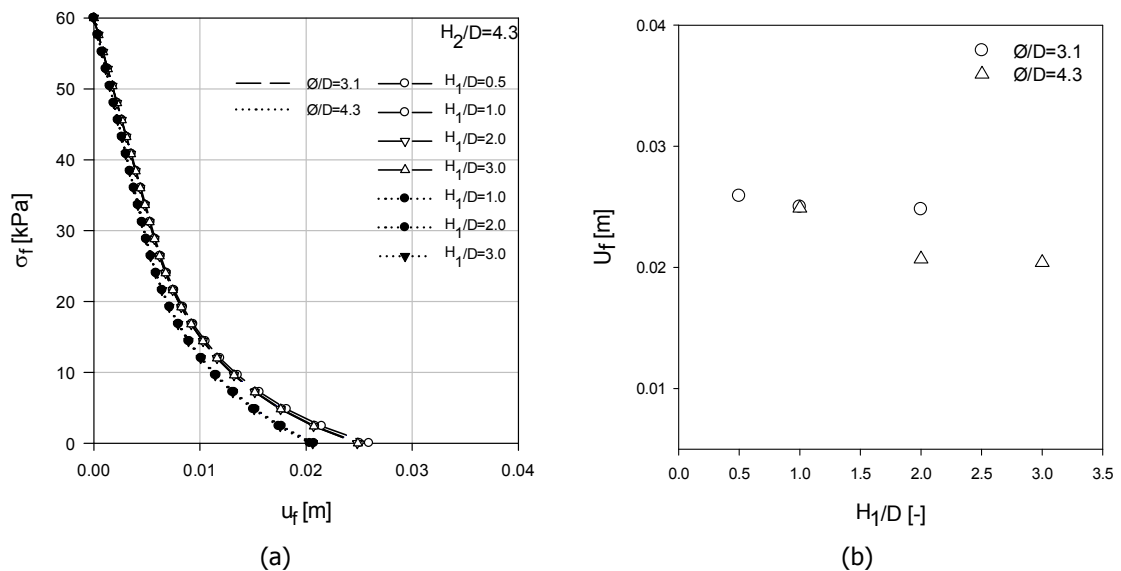**Figure 4-13 (a) Characteristic curve by varying ø/D with constant $H_1/D=2.0$ and $\sigma_0/S_u=6.0$. Long dash line: $H_2/D=4.3$ and dotted line: $H_2/D=8.8$. (b) U_f versus ø/D.**

If we consider ø/D=2.3 the development of plastic zone around the face of the extrusion reaches the boundary (where horizontal pressure is applied immediately on the mesh boundary located on the outer radius of the model). In the previous case, the plastic zone propagated although reached the bottom

boundary (shear in horizontal direction was allowed). But in this case, it is now constrained (boundary in which pressure is directly imposed as shown on **Figure 4-14a left**). As consequent of this boundary effect, an asymptotic characteristic line is obtained (**Figure 4-13a**).

<table>
<tr><td align="center">(a)
Left to right: ø/D = 2.3, 4.0, 4.9, and 5.8 respectively</td><td align="center">(b)
Left to right: ø/D = 3.4, 4.4, 5.4, and 6.4 respectively</td></tr>
</table>
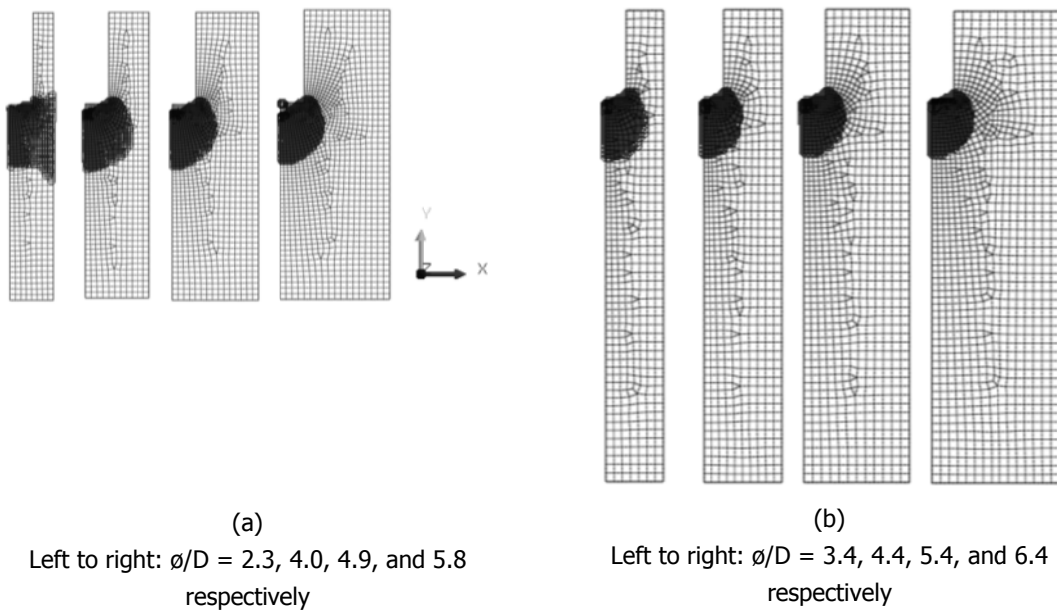
Figure 4-14 Plastic zone (grey) for constant $H_1/D=2.0$ and $\sigma_0/S_u=6.0$ with varied ø/D. (a) $H_2/D=4.3$ and (b) $H_2/D=8.8$.RLSR=1.0.

4.4.3   Chosen dimension

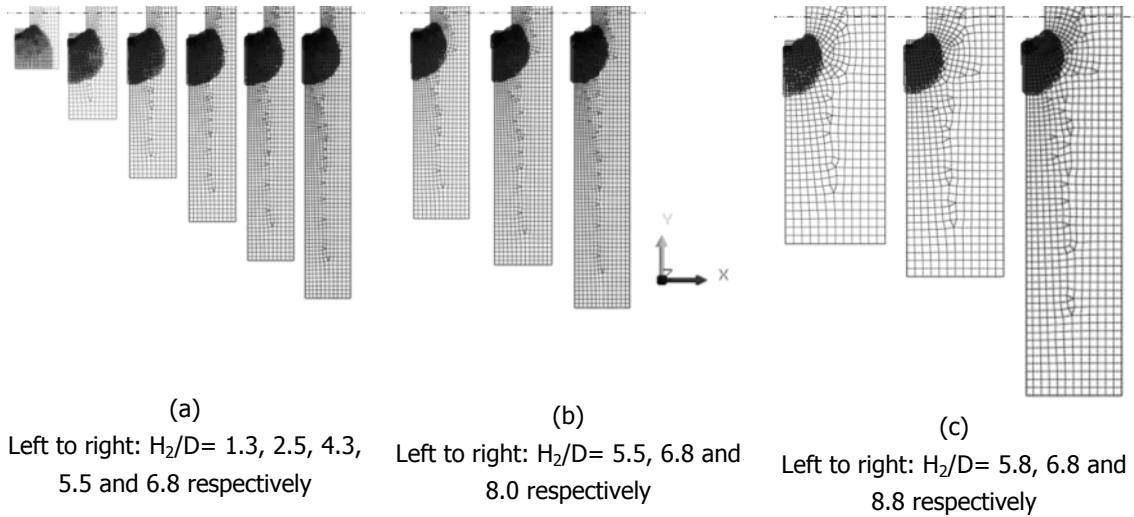Based on the above results, increasing Ø/D ratio would always favourable for the whole system. For instance, the results would not improve any further when ø/D=5.0 is considered (**Figure 4-13b**). Moreover, increasing the height (especially H_2) would be less efficient or even useless, if ratio of Ø/D was not chosen properly or too small.

For further analysis a dimension of D=10 mm, Ø=54 mm (Ø/D=5.4 and including the total thickness of the steel cylinder of 6 mm), H_1=20 mm (H_1/D=2.0) and H_2=88 mm (H_2/D=8.8) has been chosen (**Figure 4-15a**).

(a)

(b)
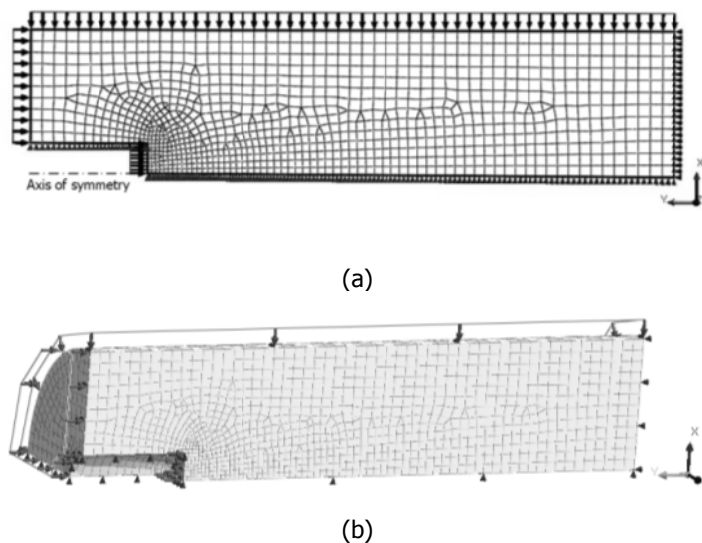
Figure 4-15 (a) 2D FEM extrusion test (considering non-uniform and concentrated of *fine* mesh around face consisting in total of 851 elements) and (b) 3D-FEM models (14,376 elements) of extrusion test with chosen dimension: H_1=32 mm (H_1/D=2.0), H_2=68 mm

4.4.4   Validation

In order to validate the 2D FEM extrusion test we introduce also a 3D FEM extrusion test having only one-quart of the total geometry as shown in **Figure 4-15b**. In this model, similar idealization (boundary conditions, applied stress and phase's analysis) and soil parameters have been applied. The results are identical considering elastic, elasto-plastic solutions as shown in **Figure 4-16**. This implies correct integrations (stress-strain relationship) in the numerical scheme and outputs considering the 2D FEM extrusion test. In order to save computation time and storage, we consider this 2D model for further analysis.
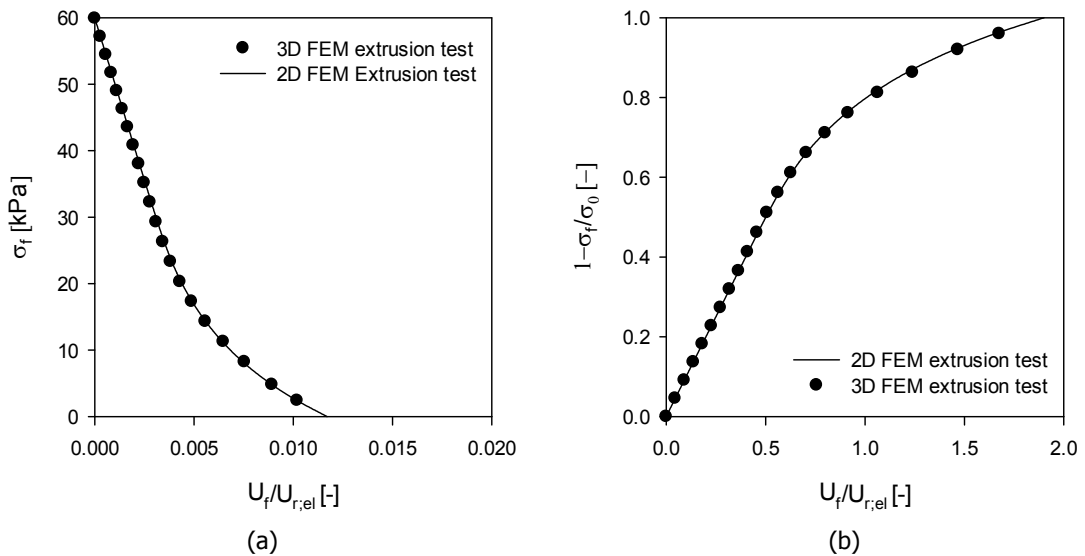
Figure 4-16 Comparison of results between the 2D and 3D FEM Extrusion tests considering the characteristic (a) and normalized curve (b).

5. Numerical investigation of face stability

5.1 Parametric study

In this step, the final dimension of the specimen (4.4.3), in which there is no effect of the boundary to be expected, is used to study the effect of the soil parameters such as shear strength (S_u), elastic modulus (E) and the effect of magnitude of initial pressure (σ_0). The results shown are in term of the characteristic curve and the non-dimensional plane considering the normalized stability factor and the normalized extrusion. The parameters (E and S_u) that are a prior and artificially defined are typical value for a kaolin clay.

5.1.1 Effect of elastic modulus, E

By varying the elastic modulus E, result gives different initial stiffness of the system. In fact, elastic strain is governed by Poisson's ratio, v, along with the elastic modulus. These particular values of parameters influence the characteristic curve, but not the curve with the normalized plane as shown in **Figure 5-1b**. This implies varying the elastic modulus E gives no effect on plasticity as proven also in **Figure 5-2** considering plastic zone.

Figure 5-1 Effect of varying E and σ_0/S_u=6.0 on the results considering (a) face pressure-displacements and (b) normalized face pressure-displacement.

Figure 5-2 Plastic zone (grey) for different value of E and σ_0/S_u=6.0. From left to right: E=10, 20, 40, 80, 160 and 320 kPa. RLSR=1.0.

5.1.2 Effect of ratio σ_0/S_u

5.1.2.1 Constant S_u

The result implies that the plastic zone is governed by the ratio between initial stress and shear strength, σ_0/S_u (**Figure 5-3**), despite the different value of E (**Figure 5-1**). By increasing the ratio, it increases the plastic zone as shown in **Figure 5-4**, Moreover, If we consider σ_0/S_u=4.0, the diameter of the plastic zone is approximately equal to the inner diameter of the sample. By increasing the ratio of σ_0/S_u up to 6.0, the diameter of the plastic zone is equal to two times of the inner diameter of the sample (**Figure 5-4**).

(a)

(b)
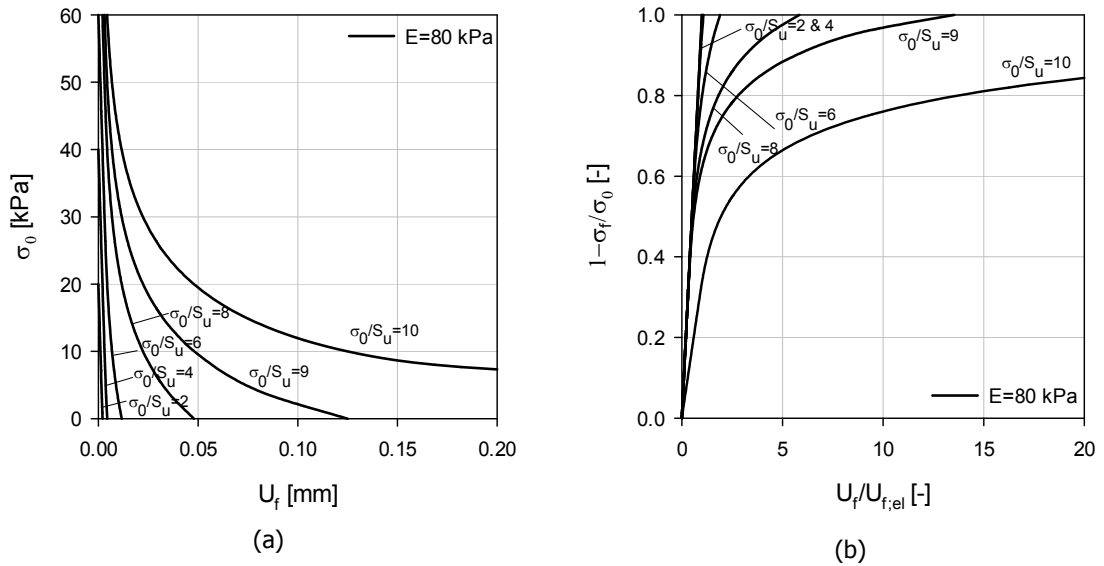
Figure 5-3 Effect of varying σ_0 with S_u=10kPa and E=80 KPa on the results considering (a) face pressure-displacements and (b) normalized face pressure-displacement.
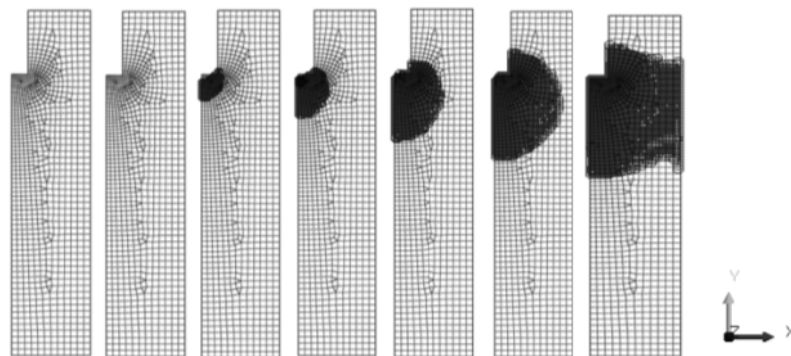
Figure 5-4 Plastic zone (grey) for different value of σ_0 with S_u=10kPa and E=80 KPa. From left to right: σ_0/S_u=1, 2, 4, 6, 8, 9 and 10 respectively. RLSR=1.0.

5.1.2.2 Constant σ_0

Due to the fact that the results were governed by ratio of σ_0/S_u, for this particular case similar trend is also obtained with respect to the former case. If the ratio of σ_0/S_u lower than 3.0, there is no plastic condition. In fact, it gives almost linear relationship between the face pressure and extrusion (**Figure 5-5**).
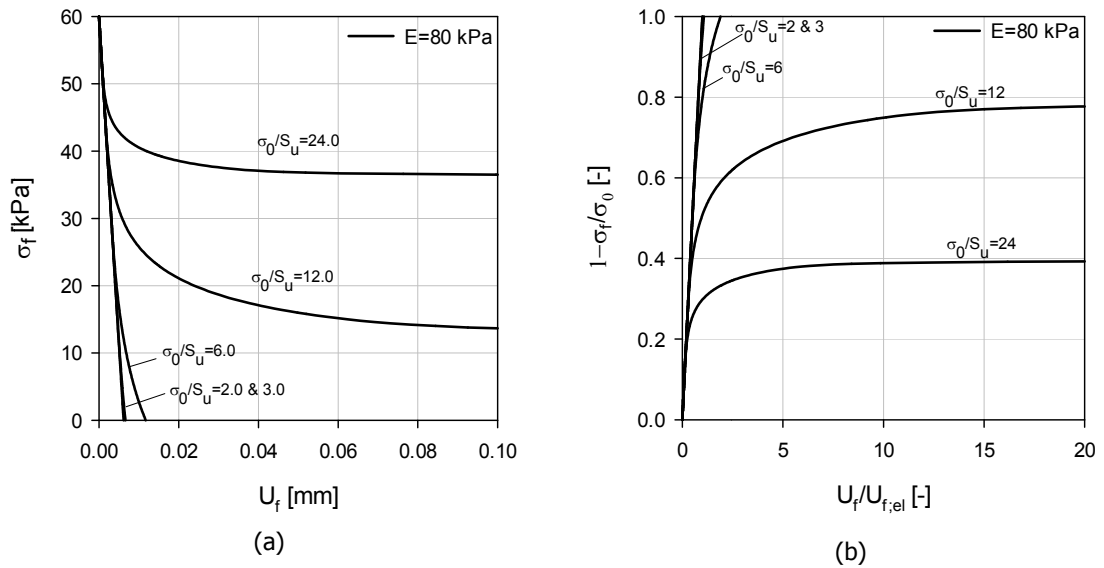
Figure 5-5 Effect of varying initial pressure, σ_0, on the results considering (a) face pressure-displacements and (b) normalized face pressure-displacement.
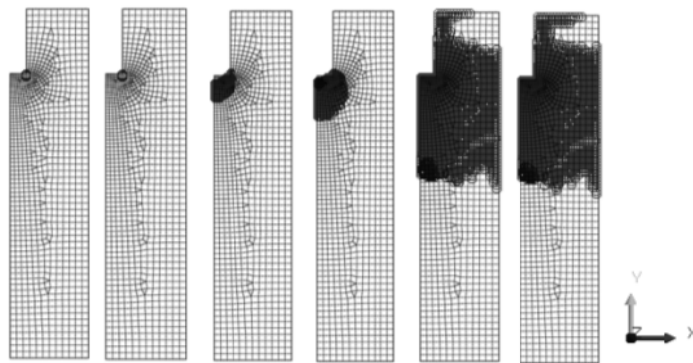
Figure 5-6 Plastic zone (grey) for different value of S_u with σ_0=60kPa and E=80 KPa. From left to right: σ_0/S_u=2.4, 3.0, 4.0, 6.0, 12, and 24 respectively. RLSR=1.0.

As it was also observed (4.4.2), every time the plastic zone reaches the outer diameter, then the development of the plastic zone is constrained due to the applied boundary conditions (**Figure 5-4** and **Figure 5-6**). Then, an asymptotic curve was obtained when σ_0/S_u equals (**Figure 5-3**) or higher than 10 (**Figure 5-5**).

It can be concluded that if the ratio of σ_0/S_u larger than certain value, the development of plastic zone could be limited by the outer diameter or boundary. Therefore, it could give unrealistic results suffered from the scale effect. These unstable results produce the characteristic curves that are approaching to asymptotic. This will be investigated more detail in section 5.4.2.

5.1.2.3 **Scale effect**

Although the magnitude of the parameters are different (e.g. between kaolin clay and NC clay), but by keeping the ratio of σ_0/S_u at the same value, both curves are superimpose considering normalized face pressure and displacement (**Figure 5-7b**). This implies that no difference in plasticity could be expected when the ratio of σ_0/S_u is kept at constant value, although the other soil parameters are changed. See **Figure 5-8**.
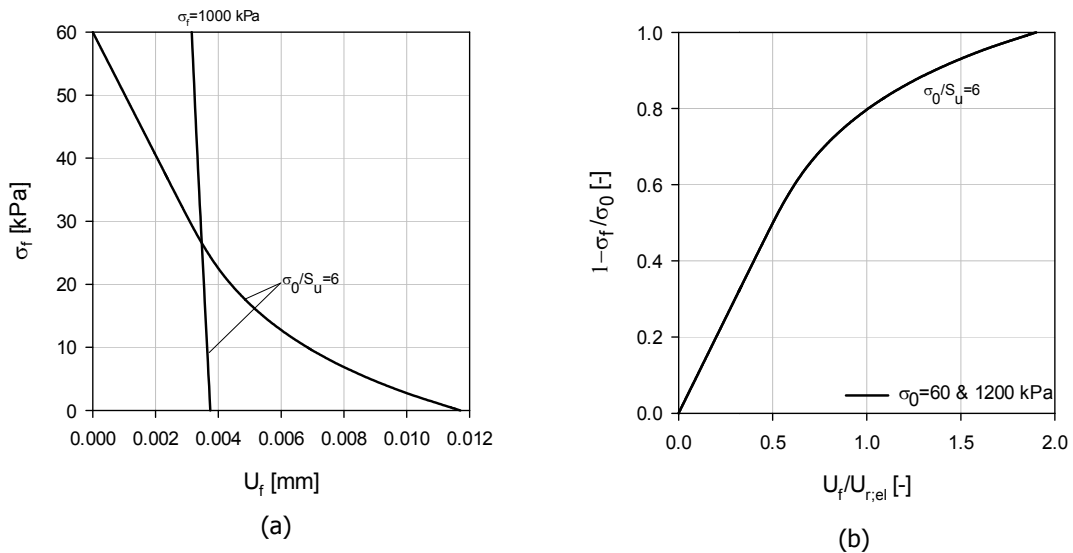
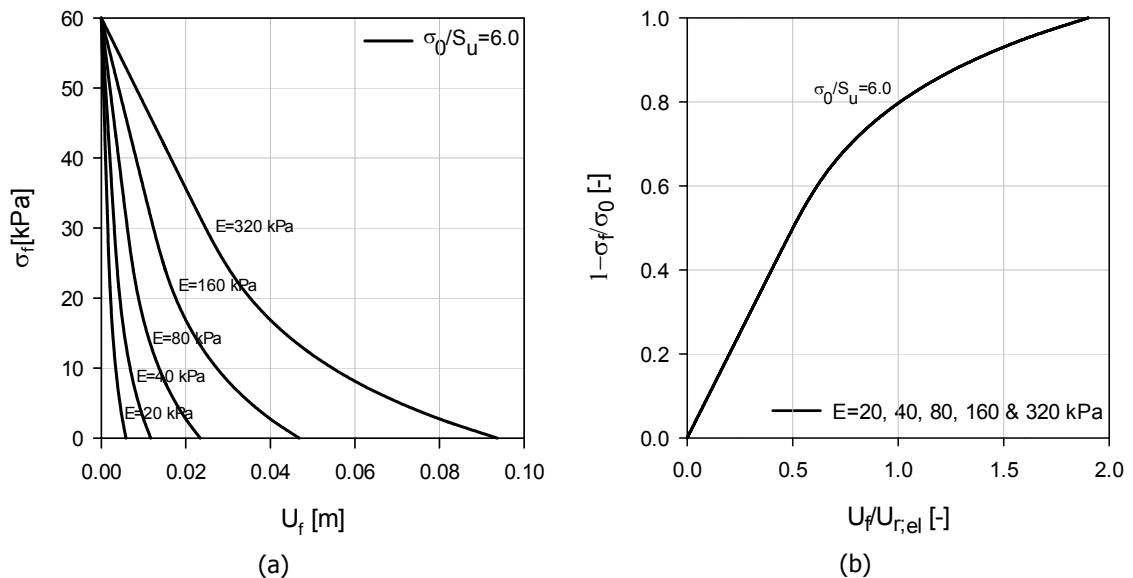**Figure 5-7 Effect of scaling the magnitude of the parameters considering the same ratio of σ_0/S_u on the results considering (a) face pressure-displacements and (b) normalized face pressure-displacement.**
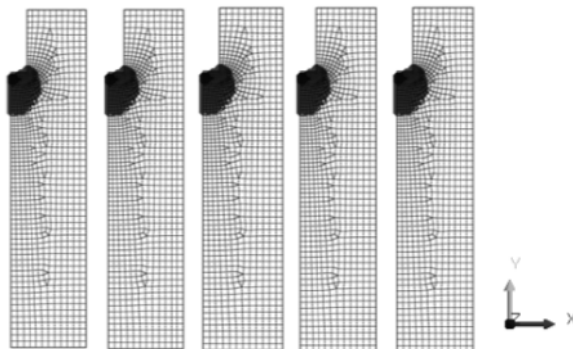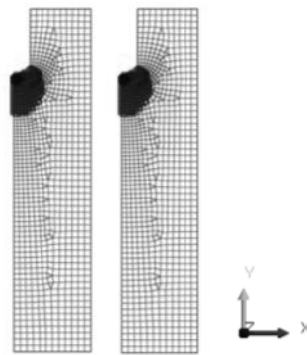

Figure 5-8 Plastic zone (grey) for different magnitude of the parameters considering constant ratio of σ_0/S_u. Left: E=5000kPa and σ_0/S_u=1200/200. Right: E=80kPa and σ_0/S_u=60/10. RLSR=1.0.

5.2   Elastic behavior

What we can observe considering elastic behavior based on the parametric study? First of all, it has been observed in **Figure 5-3** and **Figure 5-5** that when the ratio of σ_0/S_u is equal or lower than 3.0, a straight line is obtained giving an elastic response in the 2D FEM extrusion test.

Moreover, if the results of the 2D FEM extrusion test and the 3D FEM tunnel are plot into the two non-dimensional variables that already introduced by Yoo (2001),

$$\Omega_f = \frac{u_f E}{D\sigma_0}$$

Equation 5-1

and RLSR (Equation 4-3), it yields a linear curve as shown in **Figure 5-9**.
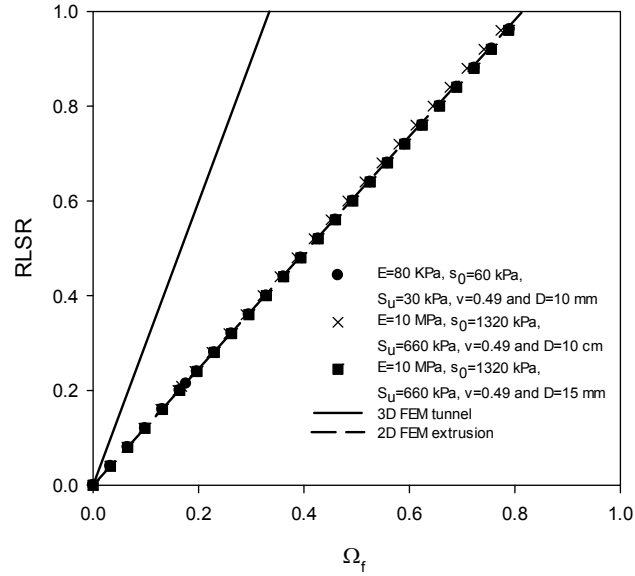
Figure 5-9 Elastic curve in the non-dimensional RLSR-Ω_f plane considering the results of the 2D FEM extrusion test and 3D FEM tunnel with $v=0.495$.

The inclination of this curve, in this non-dimensional plane, is called $K_{el,r}$ (where the subscript r stands for rigid, since these results are obtained by imposing a rigid lining) which is governed also by Possion' ratio, v. As a consequence, the residual non-dimensional displacement ($\Omega_{f,r} = \Omega_f$ for $\sigma_f=0$ or $RLSR=1$) is equal to $1/K_{el,r}$. The average value of $K_{el,r}$ for the 2D FEM extrusion test is equal to 1.25 which is lower than that of the 3D FEM tunnel which was 2.99, considering constant value of $v=0.495$.

In addition, an alternative representation of the numerical results can be done by considering $RLSR$-u_σ plane (Equation 4-3 and Equation 4-4) where $u_{r,el}$ becomes,

$$u_{r,el} = \Omega_{f,r} D \frac{\sigma_0}{E} = \frac{D\sigma_0}{EK_{el,r}}$$

Equation 5-2

All the curves shown in **Figure 5-9** are perfectly superimpose and their inclination is equal to 45 degrees as shown in **Figure 5-12** considering the non-dimensional RLSR-u_σ plane.

5.2.1   State of stress

This elastic behavior occurs when the stress state in the ground at the face and around the cavity during tunnel advance is sufficient to overcome the capacity of the medium to resist it in the elastic range (Lunardi & Kovári, 2000). Moreover, the progressive reduction in stress on the tunnel face causes a stress migration (Yoo, 2012), and further defined as "pincers effect" (di Prisco *et al.*, 2015). This causes an increase in both vertical and horizontal stresses in the soil around the tunnel. In fact similar behavior does exist in the case of the 2D FEM extrusion test.
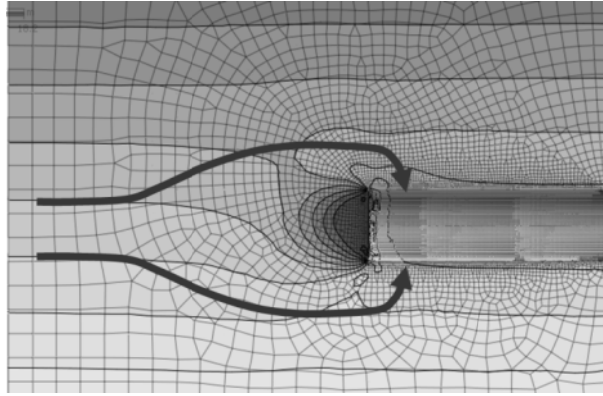
Figure 5-10 A sketch of migration of the horizontal stress: "pincers effect"

To quantify this effect, four different points (Points A, B, C and D) are positioned at different distances from the front section of the extrusion chamber (x_f): x_f =0.08D (point A), 0.17D (point B), 0.33D (point C) and 0.5D (point D). See **Figure 4-4b**. **Figure 5-11** shows a linear increase in both vertical and horizontal stresses considering each point variation in the stresses is investigated during simulation. The stress variations are larger, as was expected, in the points closer to the face.
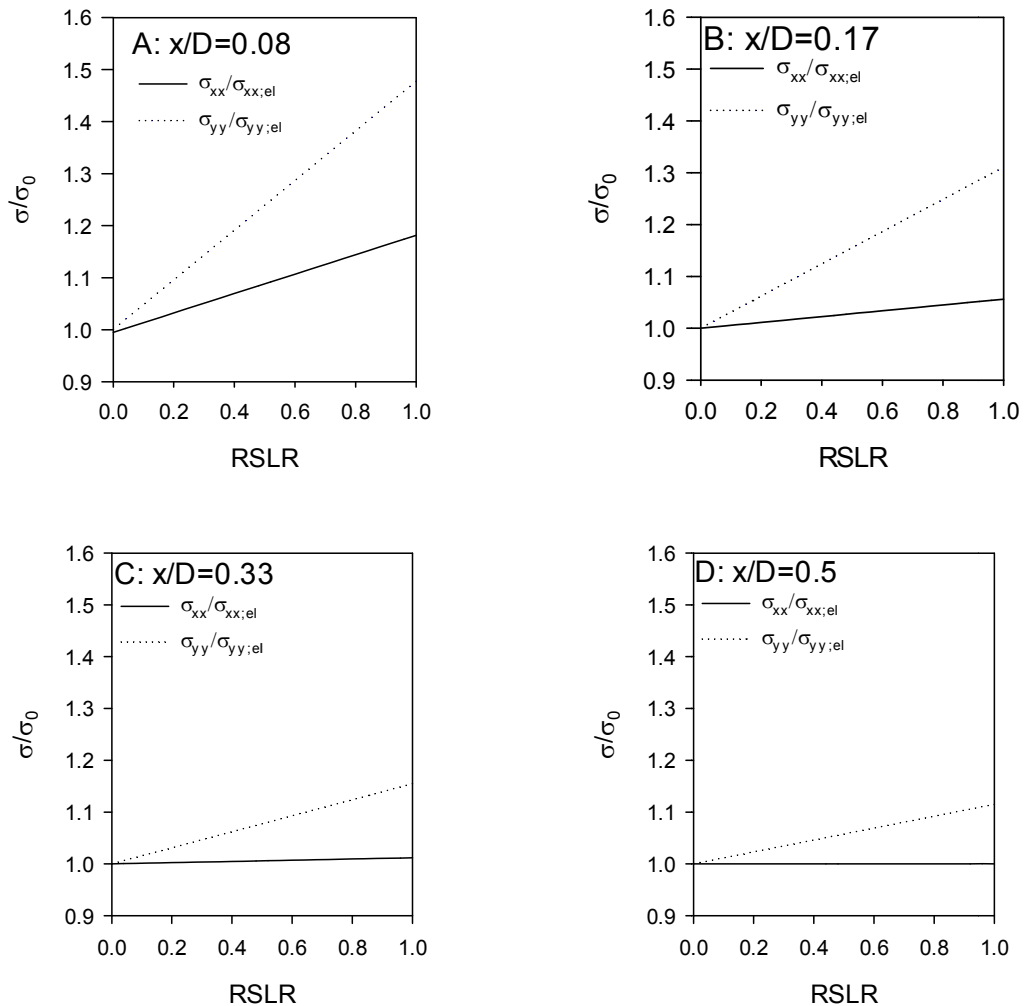
Figure 5-11 Evolution of both vertical stresses (σ_y) and horizontal stresses (σ_x) of points A, B, C,& D of Figure 4-4 (b) obtained for σ_0=1320 kPa, E=10MPa, v=0.49 considering elastic behavior.

5.3   Elasto-plastic behaviour

5.3.1   Reponse

In this paragraph, we focus on the results of one particular reference considering σ_0=1320kPa (typically for tunnel with D=12m, H=60m and and γ_{sat}=20 kN/m³ considering **Equation 4-2**) E=10MPa, v=0.495, S_u =200kPa. The results of this analysis are shown in **Figure 5-12**.
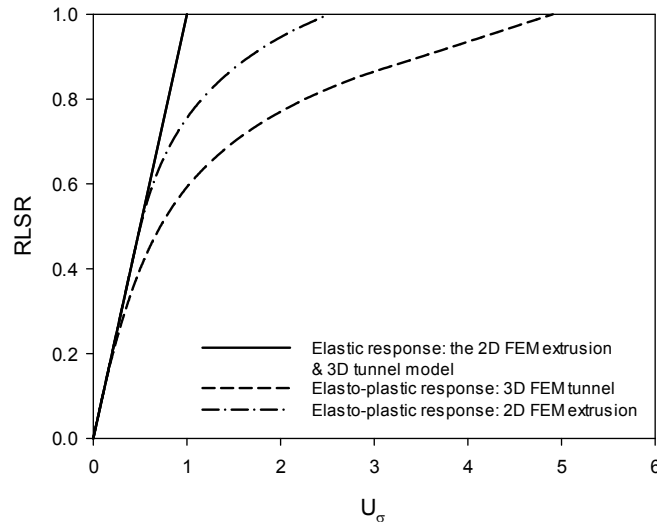
Figure 5-12 Elastic and elasto-plastic curves in the non-dimensional RLSR-σ_f plane considering the results of the 2D extrusion test and the 3D FEM tunnel for E=10MPa, v=0.495, S_u =200kPa andσ_0=1320kPa.

Figure 5-12 shows that in the case of the 2D FEM extrusion test and the 3D FEM tunnel, the response started with linear behavior. In the case of the 2D FEM extrusion test, this linear response starts at value of RSLR=0.45 while in the case of the 3D tunnel it starts earlier (RLSR=0.25). Afterwards, it gives none linear response in both models. The final value of u_σ is not 1.0 since the residual displacement at the front is quite larger with respect to the elastic one. From **Figure 5-12** we can subtract three different responses for both 2D and 3D FEM models: a linear initial response (where the linear curve is suporimpose to the elastic-plastic curve), a subsequent knee and a final approximatively linear trend.

As we can also observe from **Figure 5-12**, the difference in quantity does exist considering curves from the 2D and 3D FEM models. In order to justifiy the difference, we consider the state of the stresses in terms of ratio between the stresses and the initial one (σ/σ_0). The direction of these stresses is always perpendicular to the tunnel or the extrusion chamber axis. These stresses give "destabilizing effect" to the system during the simulation (reduction of the face pressure) considering both models. The stresses have been extracted along the two boundaries of both models as shown in **Figure 5-13e** and **-f**. The ratio of the stresses is then plotted agaist the relative distance to the axis of the tunnel or the exutrusion chamber, r/D. The plots consider RLSR=0, 0.25, 0.5, 0.75 and 1.0.

**Figure 5-13a** and **b** show that the evolution of the stresses (considering different value of RLSR) is very small when we consider the surfaces of the boundaries (right and left) located close to the tunnel face. Therefore, these "destabilizing loads" tend to be constant during the simulation or reduction of the face pressure. In the other hand, different conclusion (with respec to the 3D FEM tunnel) is observed in the case of the 2D FEM extrusion test since different boundary conditions were applied. In the case of the 2D model, it is obvious that the evolution of the stresses is constant considering the top boundary (**Figure 5-13c**). It is because the constant vertical pressures (σ_0 and σ_f) were imposed on the top boundaries. Meanwhile, zero displacements in horizontal and vertical directions have been applied considering the bottom boundary. Therefore, during the reduction of σ_f (simulating excavation) it causes a reduction of

the stresses as a consequence of equilibrium (**Figure 5-13d**). Hence, it causes reduction of the "destabilizing loads" in the system and therefore it reduces displacement at the front. The evidence of the reduction of the destabilizing loads is the main reason why the curve produced by the 2D extrusion test is (**Figure 5-12**) and will be always higher or more stable than that of produced by the 3D tunnel model.

(a)

(b)

(c)

(d)

(e)

(f)
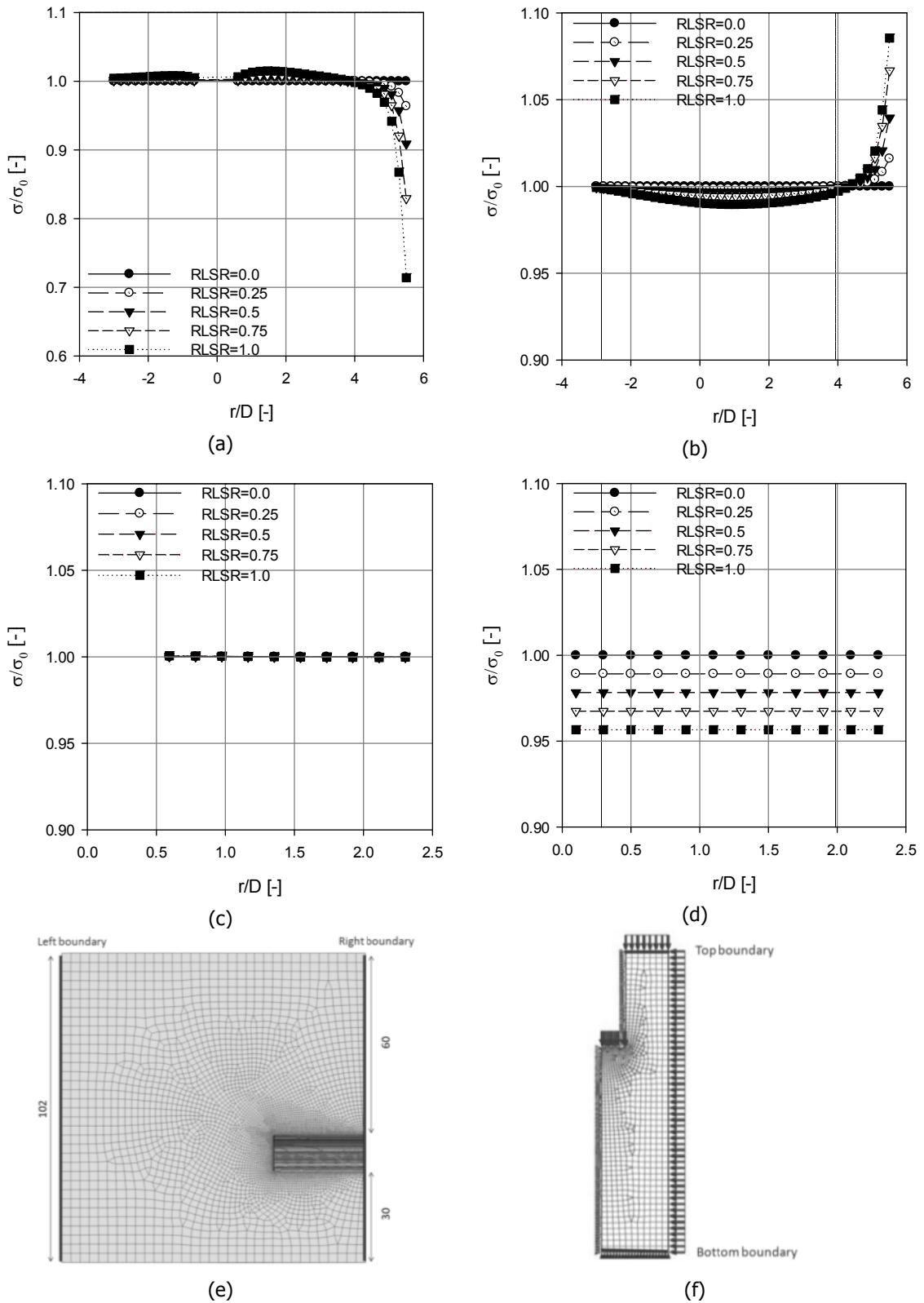
Figure 5-13 State of the stresses on: (a) the right and (b) the left boundary of the 3D tunnel model (e) and (c) the top and (d) the bottom boundary of the 2D FEM extrusion test (f). Note:

the axis of the tunnel or extrusion chamber corresponds to r/D=0, where D is the equivalent diameter of the tunnel or extrusion chamber and r is the distance with respect to the tunnel axis.

Broms and Bennemark (1967) had already defined a direct measure of the occurrence of irreversibility of stress-displacement curve by plotting the normalized residual displacement, U_σ (**Equation 4-4**), versus the instability ratio N (**Equation 2-1**). Based on the result of 15 numerical analyses (**Figure 5-14**), if the instability ratio is sufficiently small the normalized residual displacements are very close to one (vertical dashed line). In contrast, when N is sufficiently large, the normalized residual displacements are very high, having more plastic response.
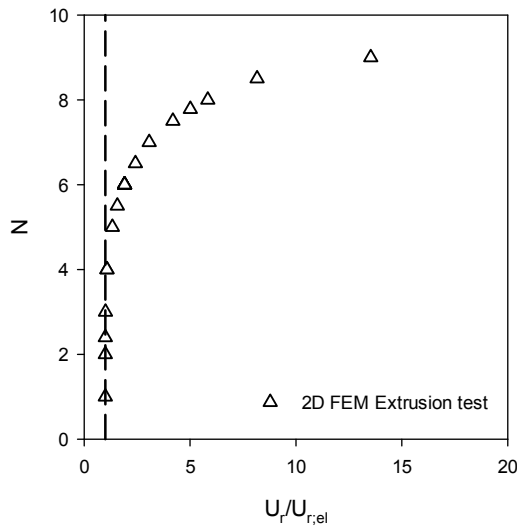
Figure 5-14 Representation of normalized residual front displacements versus the instability ratio with different value of K$_0$.

5.3.2   State of stress

In **Figure 5-15** the evolution of both vertical and horizontal stresses in points A, B, C and D is shown considering elastic-plastic response. Moreover, stresses migration has been observed, in particular in the point close to the face (point A).
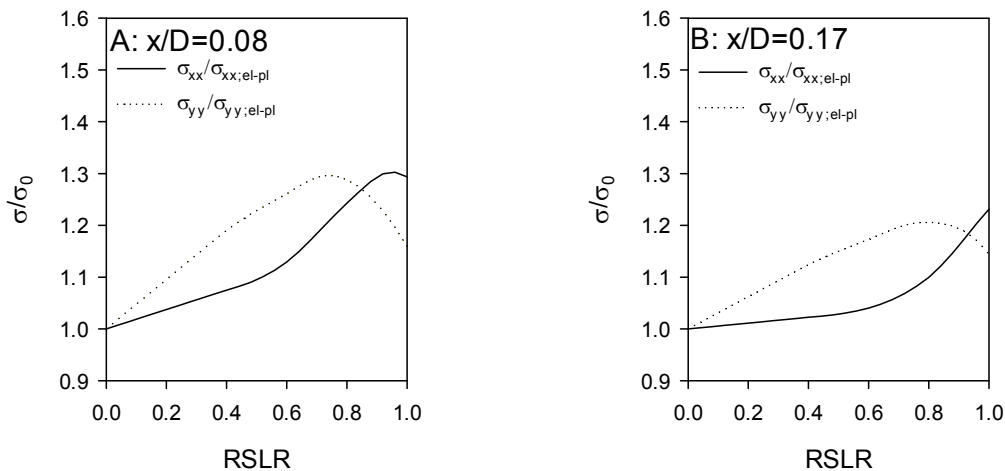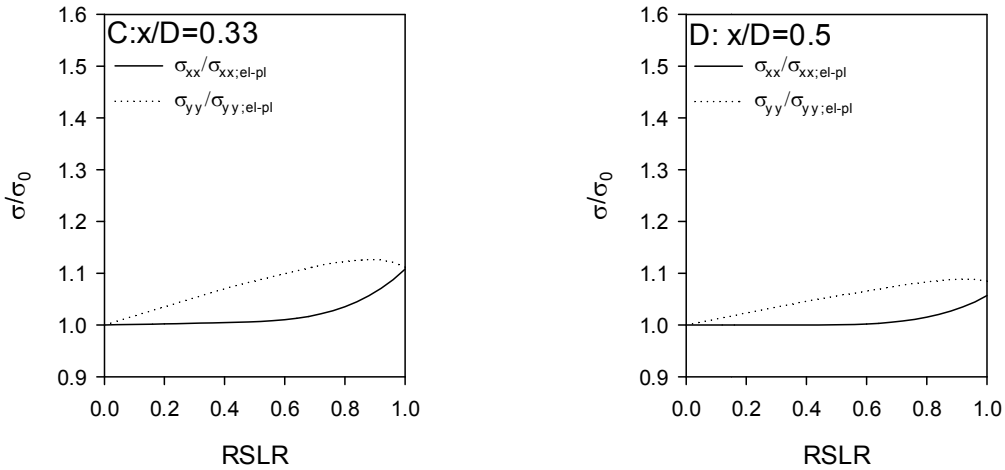
Figure 5-15 Evolution of both vertical stresses (σ_y) and horizontal stresses (σ_x) of points A, B, C, & D of Figure 4-4 (b) obtained for σ_0=1320 kPa, E=10MPa, v=0.49 considering elastic-plastic behavior.

5.3.3   Evolution of plastic zone

The evolution of the plastic mechanism is shown in **Figure 5-16**. The colored points represent the yielded points in the spatial domain at different stages of the unloading. The plasticization in the 2D model starts when RSLR equals to approximately 0.45, while in the 3D model, it started already at lowered RSLR (see also **Figure 5-12**). For increasing values of *RLSR*, the yielded volume progressively increases, not only in the advance core, but also in the soil surrounding the tunnel lining (**Figure 5-16i** and -**ii** considering -**a** and -**b**). At the end of the unloading, the plasticized domain seems to assume a hemispherical shape with a diameter approximately equal to *3D* for both the 2D and 3D FEM analyses.

(a) RLSR=0.4

(b) RLSR=0.5

(c) RLSR=0.75

(d) RLSR=1.0

(i)

RLSR=0.25   a)   RLSR=0.50   b)

RLSR=0.75   c)   RLSR=1.00   d)
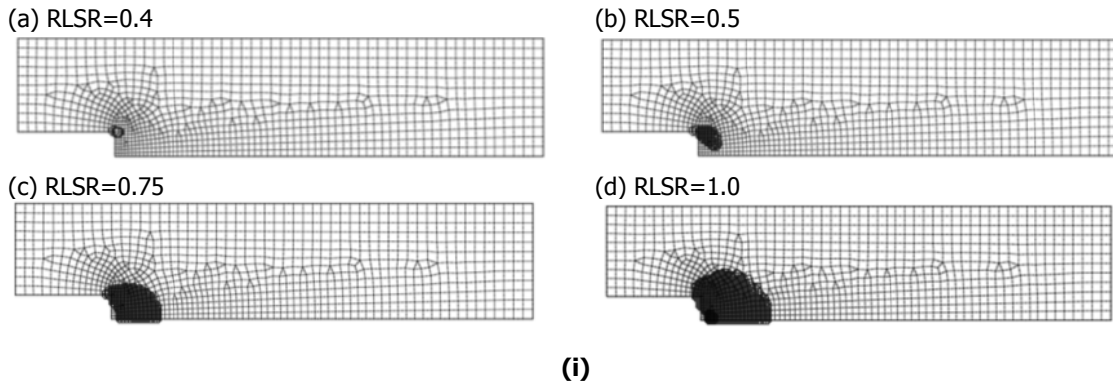
(ii)
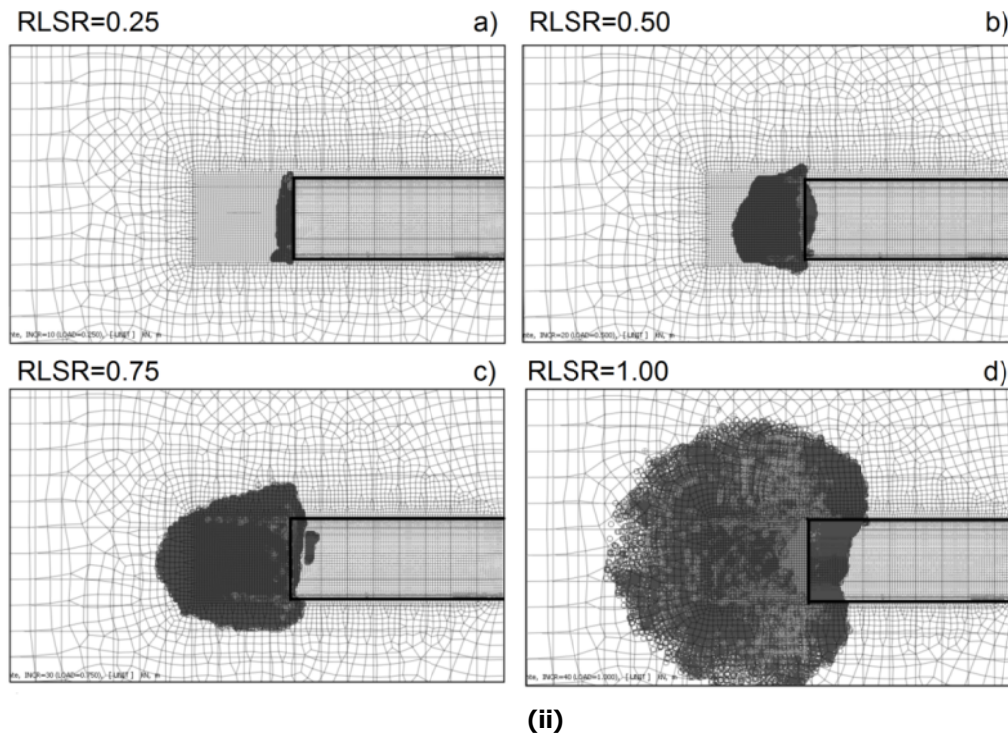
Figure 5-16 Evolution of the plastic zone around the front for different RLSR (i) the 2D FEM extrusion test (present study) and (ii) the 3D FEM tunnel (di Prisco *et al.*, 2015).

The absence of a horizontal asymptote in the elastic-plastic curve testifies a sort of "structural-hardening" strictly related to the variation in stress within the soil surrounding the tunnel lining progressively taking place during the test.

5.4 Front mother characteristic (FMC) curve

It was discussed that the characteristic curve in **Figure 4-6** of the face can be either totally linear or non-linear, according to geometrical and mechanical parameters characterizing the system. Furthermore, the normalized curve considering non-dimensional RLSR-u_σ (See **Equation 5-5** and **Equation 5-6**) plane was used in order to appreciate the plasticization of the material taking place in the system during the process of reduction in the stress on the face of the tunnel or extrusion chamber. In the end, a unique curve can be obtained when further normalization is carried out. This curve, namely front mother characteristic (FMC), had been already introduced (di Prisco *et al.*, 2015) as a convenient design chart as an useful tool for the geotechnical designer, since it allows the geotechnitian to provide a predictive evaluation of the residual displacements due to the front excavation once geometry of tunnel, height of overburden soil above the tunnel and soil parameters, *(E, Cu, γ* and *K₀)* are known. In this section, the reasoning to arrive at this unique curve is briefly described by considering the results of the 2D FEM extrusion test. Moreover, comparison between the results of the 2D FEM extrusion test and the 3D FEM tunnel (di Prisco *et al.*, 2015) is also included.

5.4.1 Effect of K_0

As it was discussed that in the standard triaxial test, the coefficient of pressure can be expressed as a ratio between the applied radial and axial pressure (**Equation 4-1**). Considering the undrained analysis, the failure criterion is governed by two-times of undrained strength, which is equals to the difference between applied axial and radial pressure. Therefore, any value of $K_0 \neq 1.0$ would effect on the results especially in the initial phase of the test as described in the following. Let consider the initial pressure, σ_0, of 60 kPa and the undrained strength, S_u, of 10 kPa. If $K_0 < 1.0$ ($\sigma_3 < \sigma_1$) where $\sigma_f = \sigma_1$, applying $\sigma_0 = \sigma_1 = 60\ kPa$ so that $\sigma_1 = 6S_u$ and considering **Equation 4-2**, therefore **Equation 4-1** becomes,

$$6S_u - 6K_0S_u = 2S_u \qquad \textbf{Equation 5-3}$$

From **Equation 5-4** we can define the lower limit of $K_0; lower = \frac{2}{3}$. Similar principle, if $K_0 > 1.0$ ($\sigma_3 > \sigma_1$), applying $\sigma_0 = \sigma_3 = 60\ kPa$ so that $\sigma_3 = 6S_u$ and considering **Equation 4-1** and **Equation 4-2** we get $K_{0;upper} = \frac{4}{3}$ from equation **Equation 5-4**.

$$\frac{6S_u}{k_0} - 6S_u = 2S_u \qquad \textbf{Equation 5-4}$$

So, theoritically the upper and lower value of K_0 that could be implemented in the extrusion trixial test are 1.33 and 0.67 respectively.

An attemp to check the limit of K_0 by means of the 2D FEM extrusion test has been carried out. A different curve to represent the result is introduce in order to include the effect on changing K_0. Different results of the 2D FEM extrusion by changing K_0 from 0.6 to 1.5 and considering the plastic zone are shown in **Figure 5-17**.
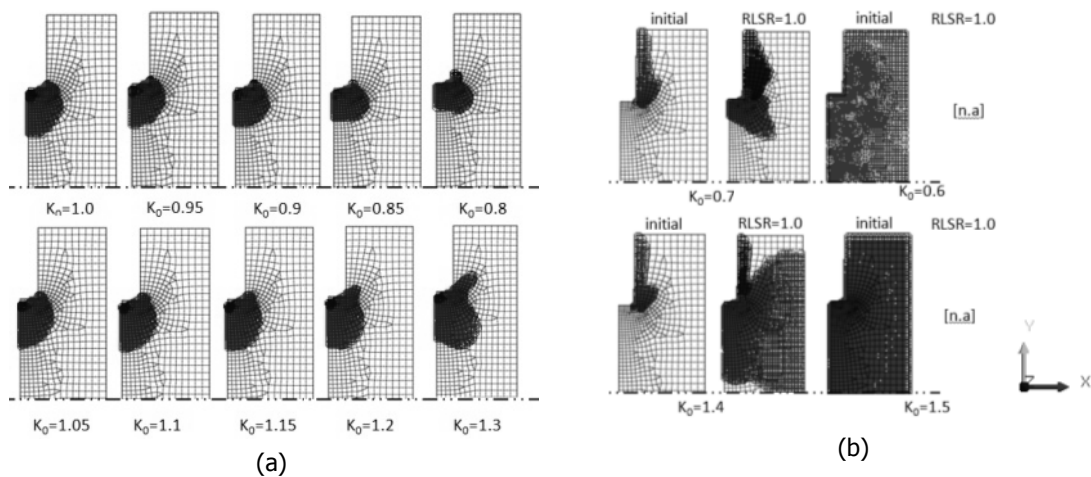
Figure 5-17 Plastic zone (grey) considering different value of K₀. (a) 'stable' (no plastic response in the initial phase) results considering K₀=0.8 to 1.3 in the last phase (RLSR=1.0) of analysis (b) 'unstable' results considering K₀<0.8 and K₀>1.3, since plastic respons already occured in the initial phase. σ₀/Sᵤ=6.0.

The results of the 2D FEM extrusion by changing K_0 from 0.7 to 1.3 (excluding the 'unstable' results) are plotted on a *RLSR.N* and u_σN plane as shown in **Figure 5-18**. Generally speaking, more plastic response and larger residual displacements occur when the value of K_0 is increased.
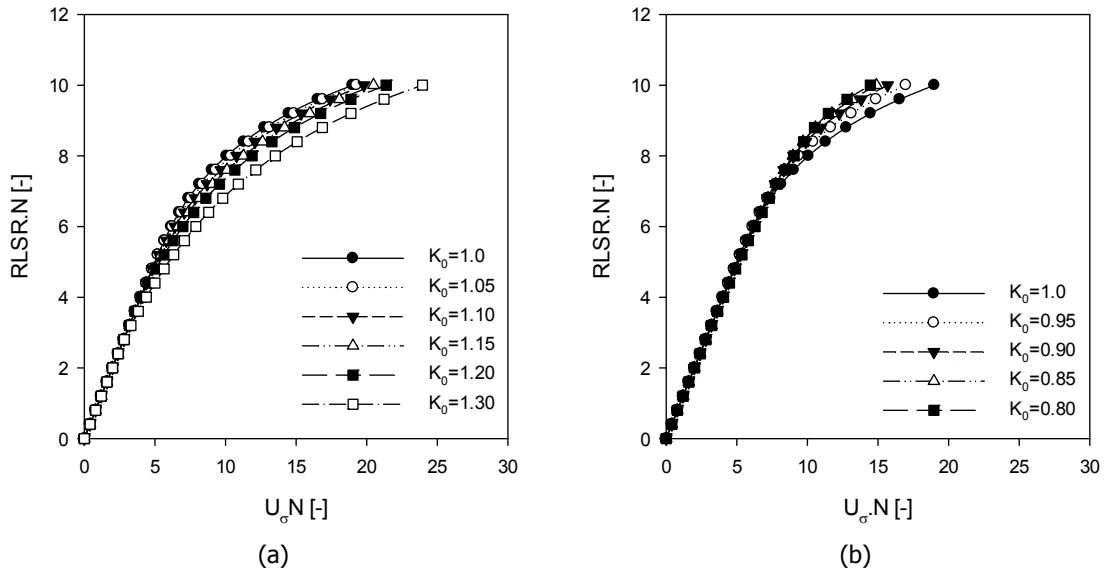
Figure 5-18 Results of the 2D FEM extrusion analyses for different values of K_0 plotted onRLSR.N −u_f.N plane. (a) $K_0 \geq 1.0$ and (b) $K_0 \leq 1.0$. $\sigma_0/S_u = 6.0$.

Front Mother Characteristic envelope (FMC) is represented in the non-dimensional *ALSR-s* plane, where

$$ALSR = RLSR \cdot N^*$$

Equation 5-5

is the Absolute Load Sharing Ratio, and

$$s = u_\sigma \cdot N^*$$

Equation 5-6

where the *N** instability ratio is defined as:

$$N^* = N \cdot K_0^a$$

Equation 5-7

Analogously, if all the characteristic curves, corresponding to the large variety of mechanical and geometrical parameters taken into consideration, are plotted considering ALSR-s plane a unique curve should be obtained. By multiplying both the x and y axis by the same value *N**, it causes a shrinkage for all the curves whichever are characterized by a small or large value of *N*. The non-dimensional coefficient *a* in **Equation 5-7**, to obtain the Front Mother Characteristic (FMC) envelope represented in **Figure 5-19**, has been assumed to be equal 0.50 and 0.65 for $K_0 < 1.0$ and $K_0 > 1.0$ respectively.
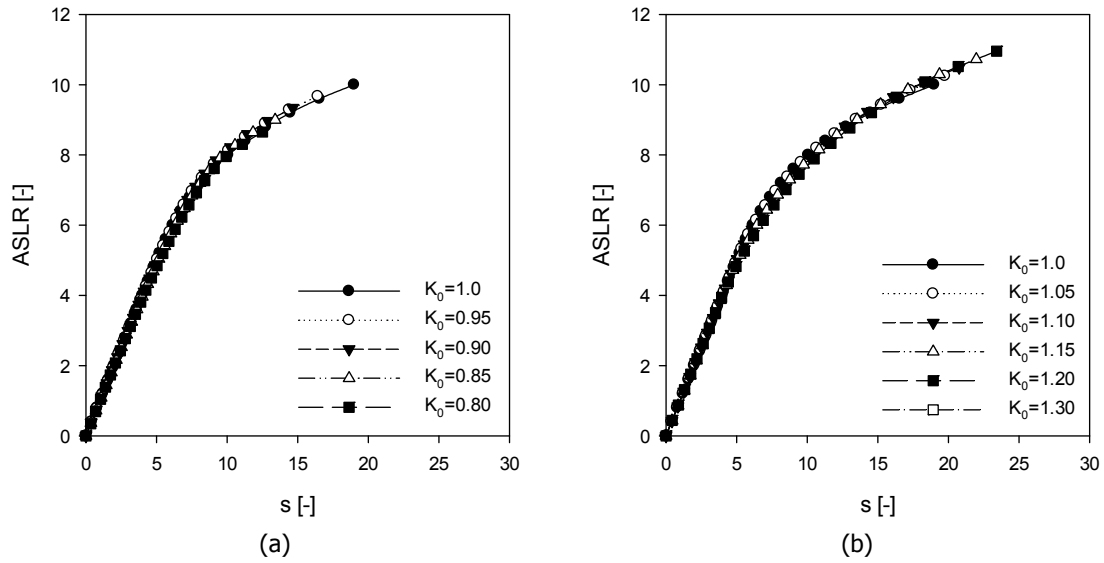
Figure 5-19 Results of the numerical elastic-plastic analyses in the ALSR-s plane. (a) K_0=0.8 – 1.0, with a=0.65 (b) K_0=1.0 – 1.3 with a=0.50. σ_0/S_u=6.0.

In general for $0.8 \leq K_0 \leq 1.3$, the non-dimension coefficient a is approximately 0.65 (**Figure 5-20a**). This value is bit lower with respect to the 3D FEM tunnel, which was 0.85 (di Prisco *et al.,* 2015). Moreover, we consider also the results of the parametric study (section 5.1) to be plotted in ALSR-s plane. In fact, all these curves are perfectly in superimposition as shown in **Figure 5-20b**.
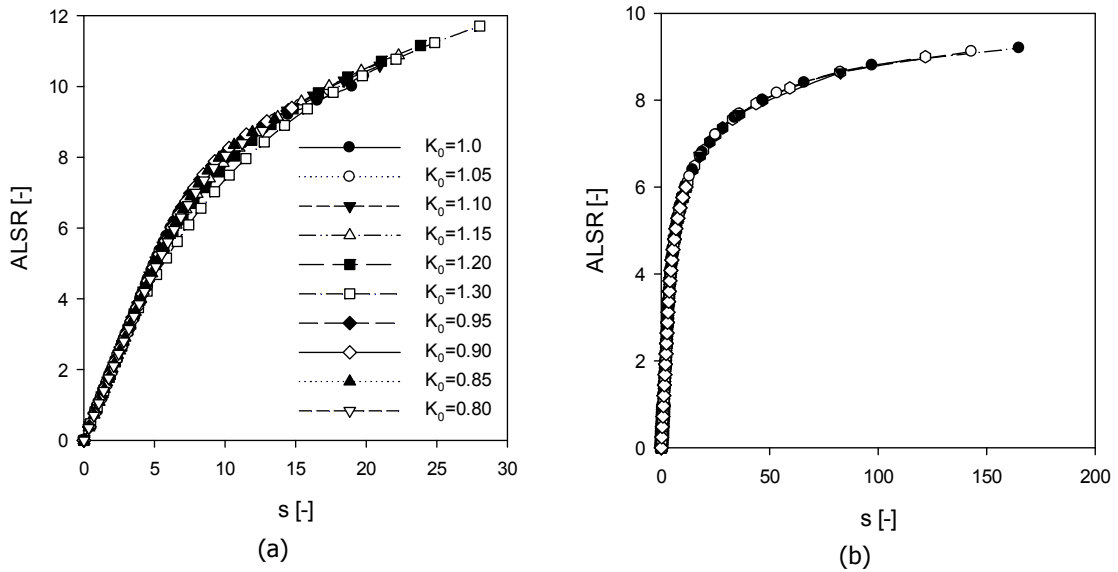
Figure 5-20 Results of the numerical elastic-plastic analyses in the ALSR-s plane. (a) considering 0.8≤K$_0$≤1.3 in Figure 5-18 with a=0.60 and (b) K$_0$=1.0 different parameters considering Figure 5-1, Figure 5-3, Figure 5-5 and Figure 5-7 for σ_0/S_u=6.0.

5.4.2   Limitation of the chosen dimension extrusion cell

In section 4.4.2, the characteristic curve for different geometry configuration had been defined by considering the ratio of σ_0/S_u up to 6.0. By considering similar cases, the ratio is now extended to higher value, e.g. the ratio σ_0/S_u up to 10.0, in order to see the response of each configuration. The results, as shown in **Figure 5-21**, are now plotted on ALSR-s plane.

In some cases, where one of the edges was to narrow, the plastic zone starts to develop and reach the edge. For example, in the case where ø/D=3.1 and H$_1$/D=0.5, the plastic zones propagates out

of the bottom plane, although the bottom boundary was constrained. This occurred when the ratio σ_0/S_u is approximately higher than 6.0. This respond occurs at the higher ratio (approximately higher than 7.0), when the ration of ø/D is increased up to 4.3. As concluded also in the previous chapter, the effect of varying edge H_1 do not affect so much on the mother characteristic curve. The results of this case are given in **Figure 5-21a**. The domain of the results of different geometry configurations is shown in **Figure 5-21d** (grey area). Big scattering in the domain implies that the results of FMC are highly dependent on the chosen geometry and the ratio of σ_0/S_u.
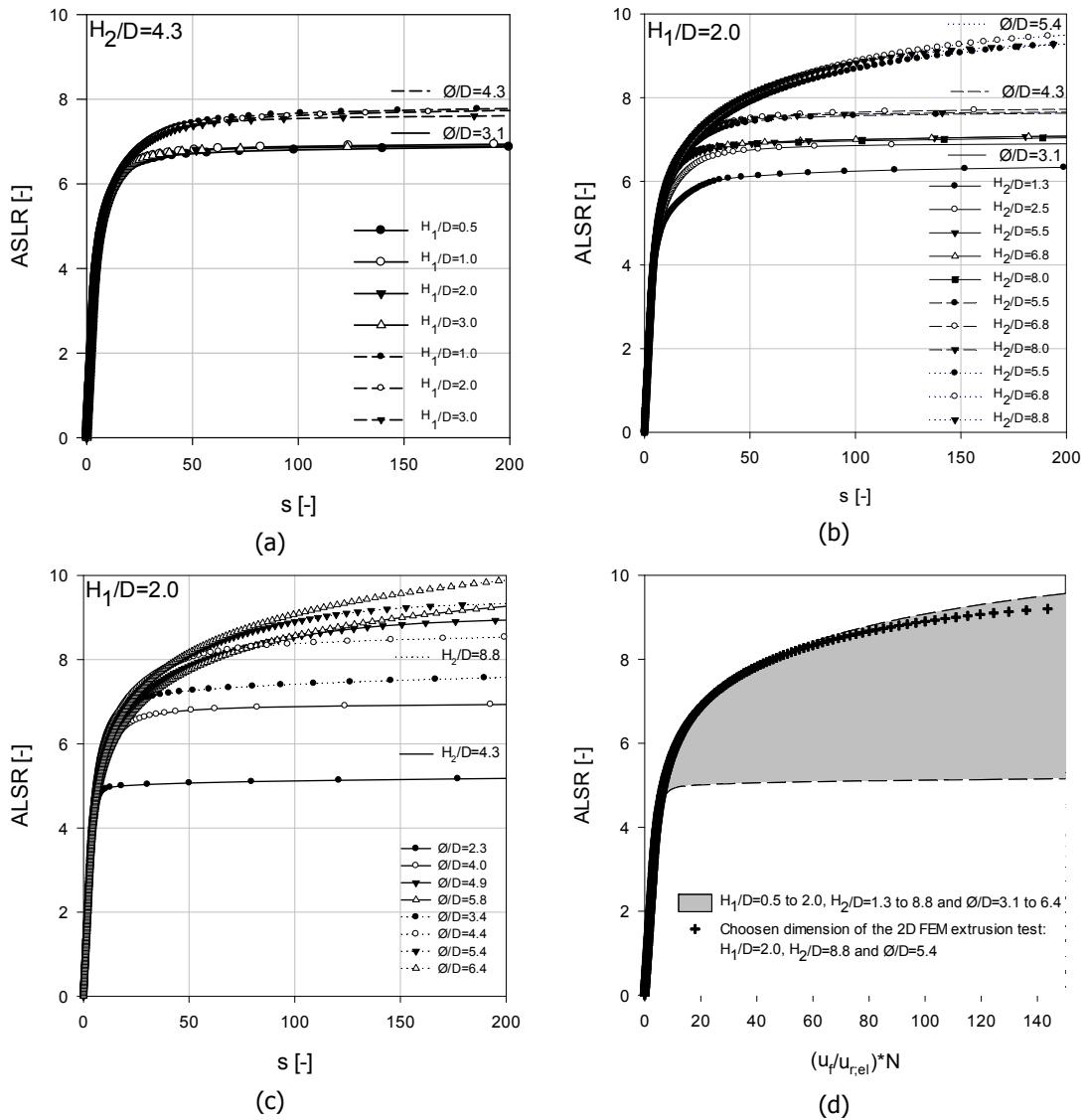
Figure 5-21 Front Mother Characteristic (FMC) curve for different configuration of geometry.

(a) $H_1/D=0.5 \div 3.0$, $H_2/D=4.3$ and ø/D=3.1 & 4.3;

(b) $H_1/D=2.0$, $H_2/D=1.3 \div 8.8$ and ø/D=3.1, 4.3 & 5.4;

(c) $H_1/D=2.0$, $H_2/D=4.3$ & 8.8 and ø/D=2.3 $\div$ 6.4;

(d) Domain of curve (a), (b) and (c) and the curve of the chosen dimension

A unique curve which corresponds to superimposition of the results of different mechanical parameters of the soil (section 5.1) is plotted also in the same figure in **Figure 5-21d** with a ('plus') marker. It must be noted that the results based on the chosen dimension (e.g. similar dimension used for the parametric studies (section 5.1)) would give proper results when the ratio of σ_0/S_u is lower than 8.5.

If we wish to consider σ_0/S_u higher than 8.5, higher ratio of ø/D should be used or to consider an extrapolation curve based on extrapolation of this data (section 5.4.3).

5.4.3   Interpolation curve and comparison with the 3D FEM tunnel

It was discussed that the results of the chosen dimension of the extrusion model were only valid (without any possible boundary effect) when the ratio of σ_0/S_u is lower than or equal to 8.5. Therefore, for the ratio of σ_0/S_u higher than 8.5, an approximated curve (bold dash line in **Figure 5-22**) can be considered. This extrapolation curve is simply derived based on the following formula used for the interpolation of the 2D FEM extrusion test for the results up to the ratio 8.5.

$$ALSR = (\beta s + \gamma)(1 - e^{-\frac{s}{\beta s + \gamma}})$$ **Equation 5-8**

α, β and γ are constant number and s is the reduction ratio of face pressure, $RLSR = 1 - \frac{\sigma_f}{\sigma_0}$ (**Equation 4-3**). This formula was analogously derived from the failure mechanism of the 3D FEM tunnel that was similiar to the very well known inverse circular foundation mechanism under undrained conditions (Eason and Shield, 1960) considering momentum equilibrium along the tunnel axis (di Prisco *et al.*, 2015).

3D FEM tunnel			2D FEM extrusion test		
α	β	γ	α	β	γ
1	0.024	5.7	1	0.024	6.9

Table 5-1 Values of non-dimensional parameters for interpolation: the 2D FEM extrusion test and 3D FEM tunnel.
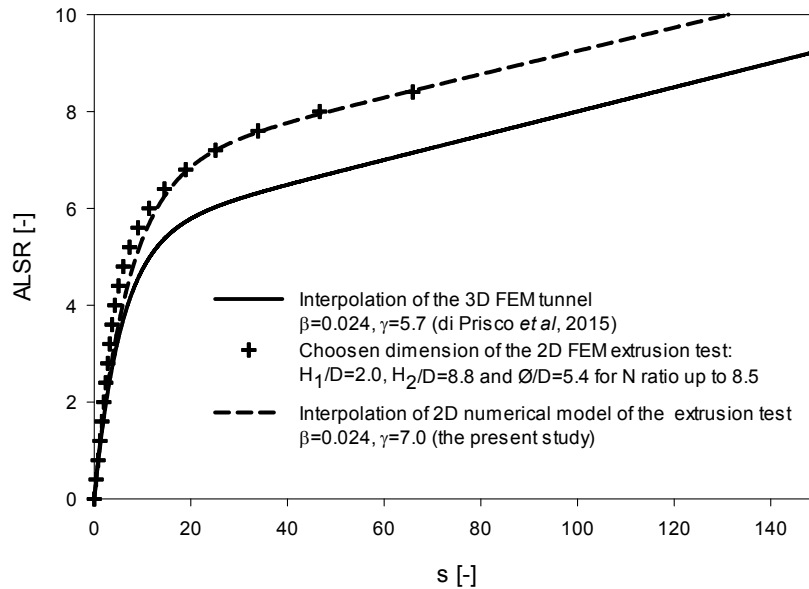
Figure 5-22 Interpolation of FMC for the 2D FEM extrusion (the present study) test and the 3D FEM tunnel (di Prisco *et al.,* 2015). Dash line: Inter- and extrapolation curve of the 2D model (the present study);Bold line: interpolation curve of the 3D model tunnel (di Prisco *et al. ,*2015).

Considering the interpolation curve, we are able to fit the curve. Care must be taken when this interpolation curve is being used, since 'the knee' (elastic-plastic range) of the interpolation curve is underestimation. Afterwards, the curve tends to be linear being in plastic zone. As it is shown in **Figure 5-22**, the interpolation curve is able to catch this plastic zone. In general the interpolation curve gave approximation with value of root-means-square error around 4%.

Although, the results have been already normalized considering FMC, the curve produced by the 2D FEM extrusion tests is again always higher than that of the 3D tunnel. The main reason of the difference was the evidence of reduction of the "destabilizing stresses" during the reduction of the pressure in the extrusion chamber. Hence, this condition reduced the radial displacement in the chamber (as discussed in section 5.3.1).

6. Conclusions and recommendations

6.1 Conclusions

In order to adopt the results of extrusion tests to study the real behaviour of stability surrounding tunnel face, some important aspects should be carefully considered. These aspects were related to the problems that are typical of studies performed in the laboratory scale. In this study, the results were focused on relationship between stresses and displacements or characteristic curve and the development of platic zone surrounding the face. The results were obtained numerically considering static analyses under undrained condition using an elasto-plastic Tresca constitutive model with axisymmetric model.

The first aspect was related to the possibility to have any possible scale effect. This effect was governed by dimension of specimens and material properties of the soils. The numerical results showed a strong dependency of the results on the chosen dimension of the specimens and the ratio between initial stress and the undrained shear strength. The study implied that the higher the ratio is the more the plastic response will be. For instance, the specimens that were used for the present study was the standard triaxial specimens whose ratio between diameter of extrusion and specimen is about 5.4. For this configuration, the effect of small scale was less significant if the ratio of the initial stress to the undrained shear strength was equal or lower than 8.5.

The second aspect was the limitation of extrusion tests to produce *in situ* condition of tunnel. The first limitation related to the distribution of initial stresses that was always uniform due to confining pressure applied in the extrusion tests. This might be not so significant in the case of deep tunnel. The second limitation concerned the boundary conditions. The bottom of the specimen of the extrusion tests must have a support, as it was done in the standard triaxial tests. This bottom boundary condition gave significant influence on the numerical results. The study revealed that there was significant reduction of stresses in the bottom boundary of the extrusion tests during the simulation (progressive release of the face pressure in the extrusion chamber). This reduction caused reduction in destabilizing loads and, hence, reduction of displacement at the face. This is the main reason why the characteristic curve produced by the extrusion tests was always higher than that of the 3D tunnel numerical analyses.

The present study also implied some particular conclusions for the extrusion tests as listed below:
(i) The elastic modulus, E, gave no effect on plasticity;
(ii) The numerical results showed peculiar response and effect when the K_0 condition was varied. It was shown that there were more plastic responce and larger residual displacements when higher value of K_0 is used. In the other hand, more confining response and lower residual displacement were expected when lower K_0 is considered;
(iii) The study showed that any asymptotic curves did not represent to any failure condition. In fact, they occured due to the scale effect, e.g. propogation of plastic zone reached outer boundary.

Although the present study showed quantitative discrepancy in the charatistic curves, it implied also conclusions that were valid (qualitatively) for the extrusion tests and the 3D tunnel analysis as mentioned in the following:
(i) Pincers effect occurs and is quantified as the stress migrates around the face: monotonically increase in elastic condition, while progressive reduction and migration of stresses in elasto-plastic condition;
(ii) By means of a suitable dimensionless plane, all of the numerical results are collapse into a unique curve (so called front mother curve (FMC)) even though the soil parameters are varied;
(iii) Although, the FMC of the extrusion tests is also always higher than that of obtained by the 3D tunnel (due to different boundary conditions), both models give similar responses: purely elastic in which no plastic development is expected, elasto-plastic and perfectly plastic with structural 'hardening' behaviour.

6.2   Recommendation for future research

It is essential to perform the real extrusion tests in order to calibrate the results of present study. In fact, we already proposed one of possible prototype of extrusion test on triaxial specimen as shown in **Figure 6-1**.
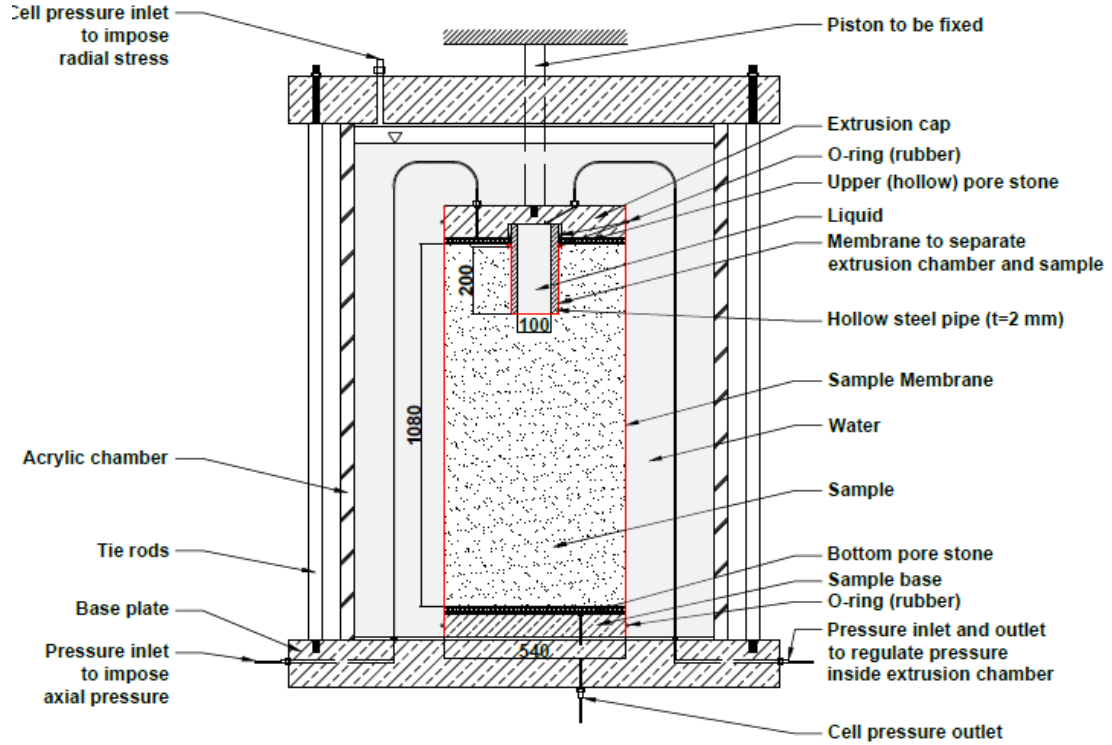

Figure 6-1 Proposed improvement of apparatus for extrusion test on triaxial specimen (ExTx_PoliMod_15)

The present study concerned only one specific type of material (cohesive soils under undrained condition). It would be also interesting to perform similar study for other type of materials, for instance for none cohesive soils under drained condition in case of excavation standstill.

7.   Bibliography

Anagnostou G. and Kovári K "Face Stability Conditions with Earth-pressure-balanced Shields" [Journal] // Tunnelling and underground space technology. - 1996. - Vols. Vol. 11, No. 2. - pp. pp. 165-173.

Anagnostou G. and Kovári K. "The Face Stability of Slurry-shield-driven Tunnels" [Journal] // Tunnelling and underground space technology. - 1994. - Vols. Vol. 9, No. 2. - pp. pp. 165-174..

Broms B. B. and Bennermark H. "Stability of Clay at Vertical Openings" [Journal] // Journal of the Soil Mechanics and Foundation Division. - 1967. - Vols. Proceedings of the America Society of Civil Engineers vol 93, No. SM1. - pp. pp. 71-94..

Burns C.A. "Shear Strength Correlations for Koalin/Water slurries: A Comparison of Recent Measurement with Historical Data" [Journal] // US Department of Energy. - 2010.

Chambon P. and Corté J. F Shallow Tunnels in Cohesionless Soil: Stability of Tunnel Face" [Journal] // Journal of Geotechnical Engineering, 120(7). - 1994. - pp. 1148-1165.

Coggan J. [et al.] 2012 [Journal] // Numerical modelling of the effects of weak immediate roof lithology on coal mine roadway stability.. - International Journal of Coal Geology, 90-91. - pp. 100-109.

Cox A.D., Eason, G and Hopkins, H. G. "Axially Symmetric Plastic Deformations in Soils" [Journal]. - 1961.

Daeman J.J.K., and Fairhurst C. "Influence Rock Properties on Tunnel Stability" [Journal] // Twelfth symposium on Rock Mechanics. - Missouri, 1970. - pp. 855-875.

Davis E. H. [et al.] "The Stability of Shallow Tunnels and Underground Openings in Cohesive Material" [Journal] // Géotechnique. Vol. 30, No. 4. - [s.l.] : Géotechnique. Vol. 30, No. 4,, 1980. - pp. pp. 397-416.

Deaman K.J.J. Technical report: "Tunnel support loading caused by rock" [Report]. - Nebraska : Department of the Army, Chief of Engineers, 1975.

Desai C. S., and Reese L. C. "Stress-deformation and Stability Analysis of Deep Boreholes" [Journal] // Proceedings of the second congress of the International Society for Rock Mechanics. - Beograd : Proceedings of the second congress of the International Society for Rock Mechanics, 1970. - pp. 475-484.

di Prisco C. [et al.] "Numerical and Theoretical Analysis of the Response of Tunnel Face Under Excavation Operations" [Journal] // Geotechnique (submitted for publication). - [s.l.] : Geotechnique, 2015.

Jing L. and Hudson J. "Numerical methods in rock mechanics" [Journal] // International ournal of Rock Mechanics and Mining Sciences 39. - 2002. - pp. 409-427.

Kirsch A. "On the Face Stability of Shallow Tunnels in Sand" [Journal] // Logos Verlag Berlin GmbH (Vol. 16). - 2009.

Lombardi G "Tunnel support (including " The problem of tunnel support")" [Journal] // Advance in rock mechanics. - 1974. - pp. 1518 - 1528.

Lunardi P "Design and construction of tunnels" [Book]. - Milano : Springer, 2008.

Lunardi P "The Design and Construction of Tunnels Using Approach Based on the Analysis of Controlled Deformation in Rocks and Soils" [Journal] // Tunnel and Tunneling International. - 2000.

Lunardi P and Kovári K "On the Observational Method in Tunneling" [Journal] // Rockmass.net. - 2000.

Mair R.J. "Tunneling and Geotechnics: New Horizons" [Journal] // Géotechnique 58, No.9. - 2008. - pp. 695-736.

Meguid M. A. , et.al "Physical Modelling of Tunnels in Soft Ground: A Review" [Journal] // Elsevier. - 2008. - Vol. Tunnelling and Underground Space Technology 23. - pp. 185-198.

MIDAS GTS NX Analysis reference [Report]. - 2014 version 2.1.

MIDAS GTS NX Verification manual [Report]. - [s.l.] : GTS, 2010 version 1.1.

Müller L and Fecker E "Grundgedanken und Grundsätze der "Neuen Österreichischen Tunnelbouweise" [Report]. - Claustal : Felsmechanik Kolloquium Karsruhe, Trans Tech Publ, 1978.

Shin J. H. [et al.] Model Testing for Pipe-reinforced Tunnel Heading in a Granular Soil [Journal] // Tunnelling and Underground Space Technology, 23(3). - 2008. - pp. 241-250..

Shin J. H., "Numerical analysis of tunnelling in decomposed granite soil" [Report]. - London : Imperial Collage, University of London, 2000.

Sousa L.S., PhD dissertation: "Risk Analysis for Tunnel Projects" [Report]. - [s.l.] : MIT, 2010.

Sterpi D. and Cividini A A physical and Numerical Investigation on the Stability of Shallow Tunnels in Strain Softening Media [Journal] // Rock Mechanics and Rock Engineering, 37(4). - 2004. - pp. 277-298.

van Langen H PhD dissertation: "Numerical Analysis of Soil-Interaction" [Report]. - Delft : [s.n.], 1991.

Wagner H. "The New Australian Tunnelling Method" [Journal] // The Technology and Potential of Tunneliling, The South African Tunelling Conference. - Johannesburg, 1970. - pp. 121-127.

Yeo Chong Hun "Stability and Collapse Mechanisms of Unreinforced and Forepole-reinforced Tunnel Headings" [Report] : PhD thesis. - Singapore : Department of Civil and Environmental Engineering, National University of Singapore, 2011.

Yoo C "Finite Element Analysis of Tunnel Face Reinforced by Longitudinal Pipe" [Report]. - [s.l.] : Computers and Geotechnics 29 (2002) 73–94, 2002.

8.   Appendix 1: Bearing capacity of circular footing

The goal of this paper is to study axisymetrical problem considering a simple analysis using Midas GTS NX. Two objectives of this study:

1. How to recover the mean yield-points pressure from the reactions due to any prescribed displacement;
2. In some particular cases considering soil-structure interaction, care must be taken due to any possible development of displacement singularities and zone of high distortion (Langen, 1991). In some numerical analysis model, interface elements can be used to model these zones. In Midas GTS NX, it was found that there is no need to use any interface elements. It was shown that the quality of the mesh around the point governed the severity of the distortion.

Two examples were chosen. The first example was referred to the solution for the mean pressure beneath rigid and smooth circular footings on frictional soil derived by Cox (1960). The second example was adapted to the solution of Langen and Vermeer (1991) for rough rigid punch penetrating into cohesive soil, shown in the following chapter.

Geometry

The geometry data for the rigid circular footing with radius of 3 m on a Mohr-Coulomb soil is shown in **Figure 8-2**.
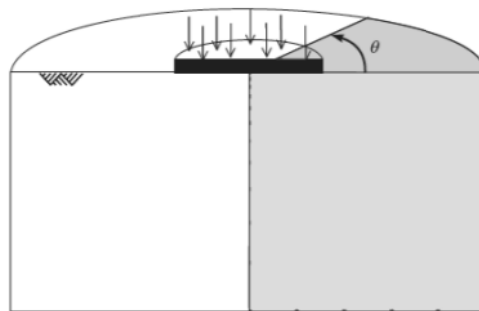

Figure 8-1 Problem geometry of smooth circular footings on frictional soil (after Plaxis).

The problem is analyzed by creating a model which consists of 150 elements.
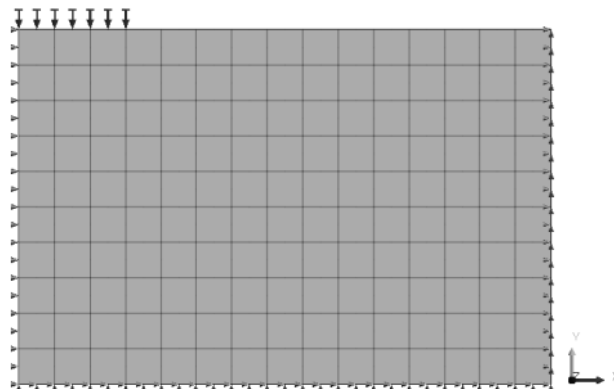
Figure 8-2 Model geometry, prescribed displacement over 3 meters and boundary conditions.

Axisymmetric:

The analysis is carried out using an axisymmetric model. A prescribed displacement is applied at the tope to simulate the penetration of the footing. For an axisymmetric calculation, the mesh represents a wedge of an included angle θ of one radian. Therefore, the calculated reaction force must be multiplied by 2π to

obtain the load corresponding to a full circular footing using the following formula:

$$q = \frac{2\pi \sum f_i^{(y)}}{\pi R^2}$$ **Equation 8-1**

where $f_i^{(y)}$ is the reaction force in the y-direction at footing node i and R is effective radius of the footing.

It must be kept in mind that the error in the bearing capacity is related to the indeterminacy in the apparent width of the footing. The mechanism shown in Figure 4 implies a displacement singularity at the ends of the footing as it was also anticipated by the work of Cox (1960). It is a fan radiating in different directions at corner point of footing. Such singularity cannot be modeled by a conventional finite element computation which involves regular displacements for all material points. It might need an interface material representing potential slip plane (Langen, 1991).
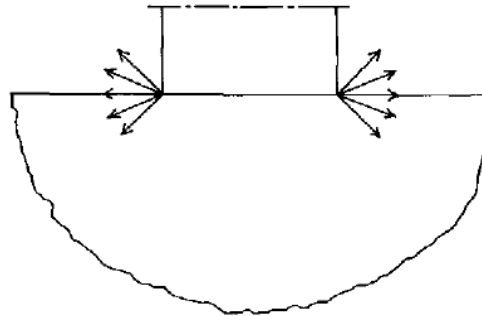

Figure 8-3 Singularity velocity at corner point of footing (Langen, 1991).

In these numerical simulations, it is no need to introduce any interface element. In fact the effect of the singularity is spread over the width of one element. The apparent position of the displacement jumps within that element and depends on the exact geometry of the velocity field that develops. The only small adjusting is that in deriving the mean pressure beneath the circular footing, it is assumed that the jump occurs half a zone width from the end of the controlled boundary segment.

Material:

The material behavior is represented by the Mohr-Coulomb model. Note that an associated plastic analysis is performed by considering, $\emptyset = \psi = 30°$.

	Problem no. 2	
Dimension	Width	15 m
	Height	10 m
Element	8-node quadrilateralaxisymmetricelement	
Material	Modulus of elasticity	E = 257143 kPa
	Possion's ratio	v = 0.286
	Saturatedweight	$\gamma = 20$ kN/m^3
	Yieldcriteria	Mohr-Coulomb
	Cohesion	c = 50 and 100 kPa
	Friction angle	$\varphi = 0°$
	Dilatancy angle	$\psi = 0°$
Boundarycondition	Left side	Constrain x
	Right & bottom ends	Constrain x & y
Load case	Prescribed displacement of 0.25 m at footing nodes	

Table 8-1 Parameters used to analyis smooth circular footings on frictional soil.

Calculations:

The initial stress distribution is generated in the initial phase by using the K_0 procedure, where the displacement was set to zero. In the next phase the prescribed displacements along the width of the footing is activated in a separate phase considering none-linear analysis.
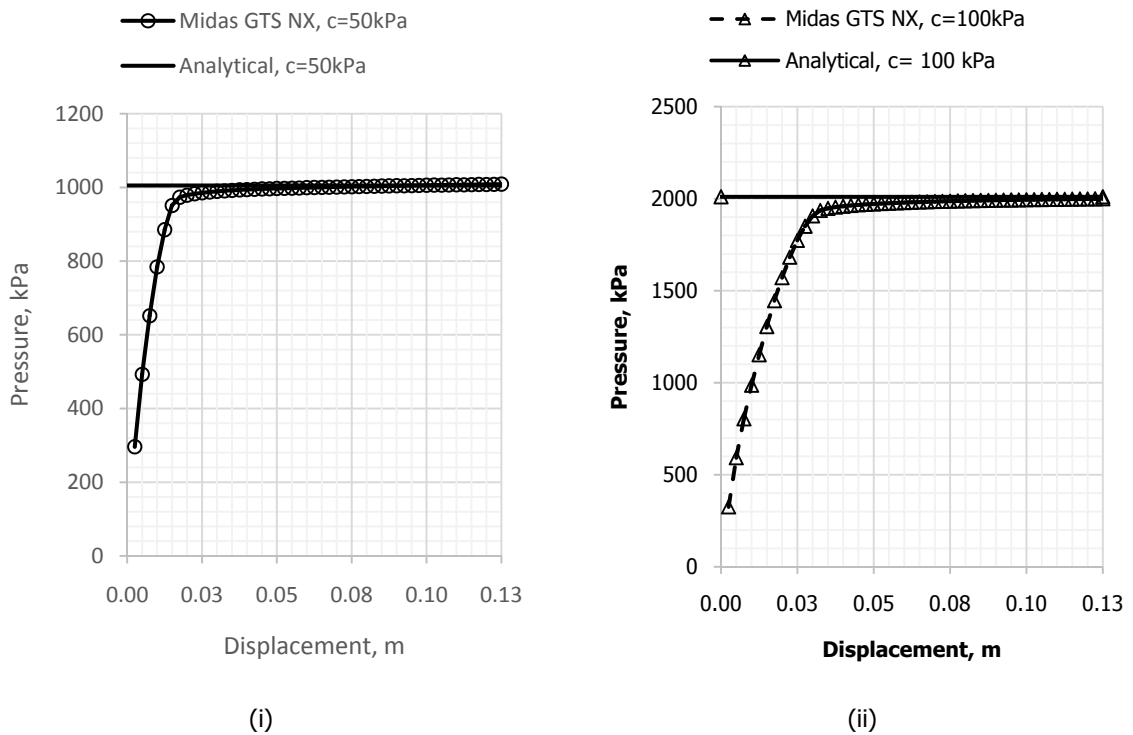
(i)	(ii)

Figure 8-4 Load displacement curve(i) c=50 kPa and (ii) c=100kPa for smooth circular footings on frictional soil.

Output:

As it was indicated that the effective radius of the footing is the radius to the point midway between the last node with an applied displacement (x = 3.00 m) and the adjacent node (x = 3.75 m), therefore, the effective radius of the footing is 3.375 m.

The calculated collapse load is kN/rad, which corresponds to an average vertical stress at failure, P_{mean}, with:

$$P_{mean;1} = \frac{36096}{\pi R^2} = 1008.7 \ kPa \qquad \textbf{Equation 8-2}$$

for problem no. 1.

$$P_{mean;2} = \frac{71545}{\pi R^2} = 1999.3 \ kPa \qquad \textbf{Equation 8-3}$$

Verification:

The exact solution (Cox, 1962) for the mean yield-point pressure at collapse for cohesion of 50 kPa and $\emptyset = 20°$ for the first problem is,

$$P_{mean;sol;1} = 20.1 * c_2 = 20.1 * 50 \ kPa = 1005 \ kPa \qquad \textbf{Equation 8-4}$$

while for the second problem, the semi-analytical value of the mean pressure over the footing at failure for a friction angle 20°, with cohesion of 100 kPa is found to be

$$P_{mean;sol;2} = 20.1 * c_2 = 20.1 * 100 \, kPa = 2010 \, kPa$$

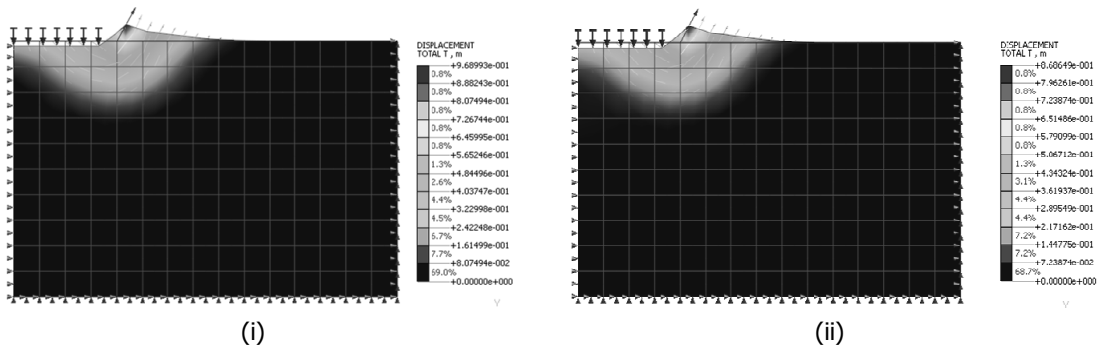(i)   (ii)

Figure 8-5 Displacement vectors beneath circular footing at failure (i) c=50 kPa and (ii) c=100 kPa for smooth circular footings on frictional soil.

The relative error of the results calculated with MIDAS remain within 1% for the given two problems,

	Analytical	Midas GTS NX	
Problem	Mean pressure at collapse (kPa)	Mean pressure at collapse (kPa)	Relative error (%)
1 (c=100kPa)	2010.0	1999.3	0.53
2 (c=50 kPa)	1005.0	1008.7	0.37

Table 8-2 Results and verificationfor smooth circular footings on frictional soil.

9. Appendix 2: Rough rigid punch penetrating into cohesive soil

The effect of singularity points becomes more sever when a buried structure in a soil mass, well-known problem of rigid punching as shown in the following figure.
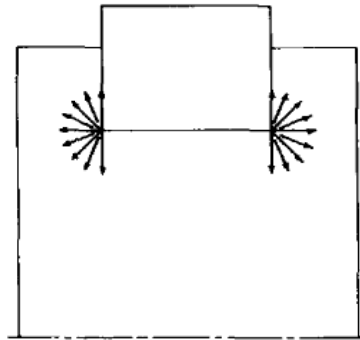

Figure 9-1 Singularity velocity at corner point of rigid buried structure in a soil mass.

In this example it is investigated the results when the possible distortion at the edge of the die might occur when the problem was modeled without any interfaces. In this example two models are introduced. The first model shows that there are eight elements under the punch, in which the corner of the edge was directly connected to the boundary condition of the vertical edge. The second model was tried to treat the corner by introducing one dummy element in order to have gradual application to reduce any possible oscillation closed to this corner.
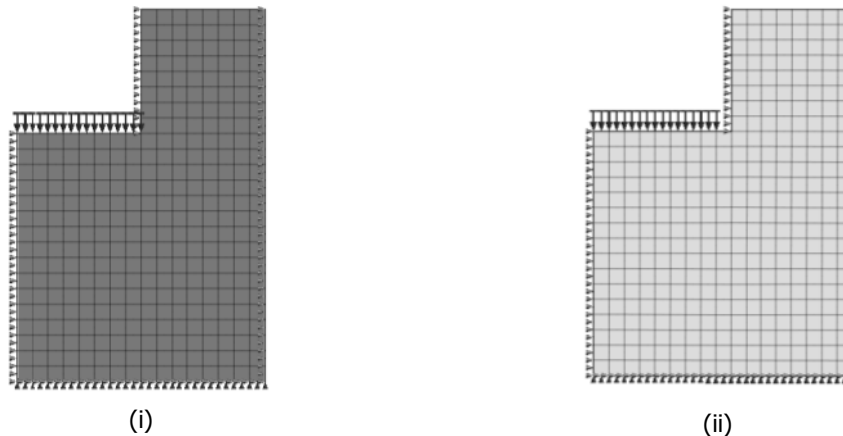

| (i) | (ii) |

Figure 9-2 Mesh for 8-node elements quadrilateral: (i) without any treatment and (ii) corner's treatment for rigid buried structure in a soil mass.

Material:

The material behavior is represented by the Mohr-Coulomb model. Note that an associated plastic analysis is performed by considering, $\emptyset = \psi = 0°$.

	Problem no. 2	
Dimension	Width	2 m (punch width=1m)
	Height	2 m
Element	8-node quadrilateralplanelement	
Material	Modulus of elasticity	E = 2500kPa
	Possion's ratio	v = 0.25
	Saturatedweight	$\gamma = 16kN/m^3$

	Yieldcriteria	Mohr-Coulomb
	Cohesion	c = 10
	Friction angle	φ = 0°
	Dilatancy angle	ψ = 0°
Boundarycondition	Left, right side and vertical edge	Constrain x
	Bottom ends	Constrain x & y
Load case	Prescribed displacement of 0.25 m at footing nodes	

Table 9-1 Parameters used to analyisrigid buried structure in a soil mass.

Result:

It must be noted that in model B, the width of the punch extends to one-half of one element at which the displacement jump occurs. It is now 1.0625 m. While in the case model A, it remains.
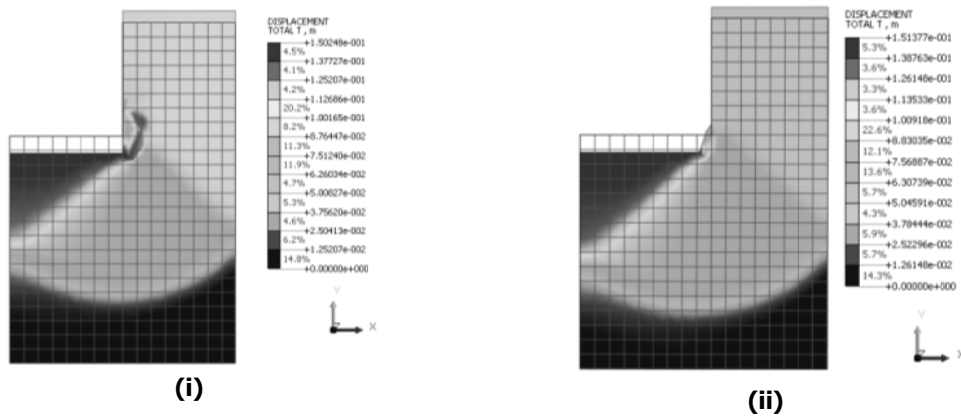

(i)

(ii)

Figure 9-3 Displacement field for 8-node elements quadrilateral at last step: (i) without any treatment and (ii) corner's treatment for rigid buried structure in a soil mass.

It was also observed that in model A where there is no additional element at the corner, the oscillation of the reactions occurred for the entire step giving a significant inaccurate result of the average pressure. When the model B is considered, the oscillation was limited giving more reliable result. In the following figure shows how the oscillation of the reactions occurs at the corner edge of the punch at model A while it was limited in Model B. Although this was for the last step of the simulations, the trend of the results was observed for all the time step of the simulation.
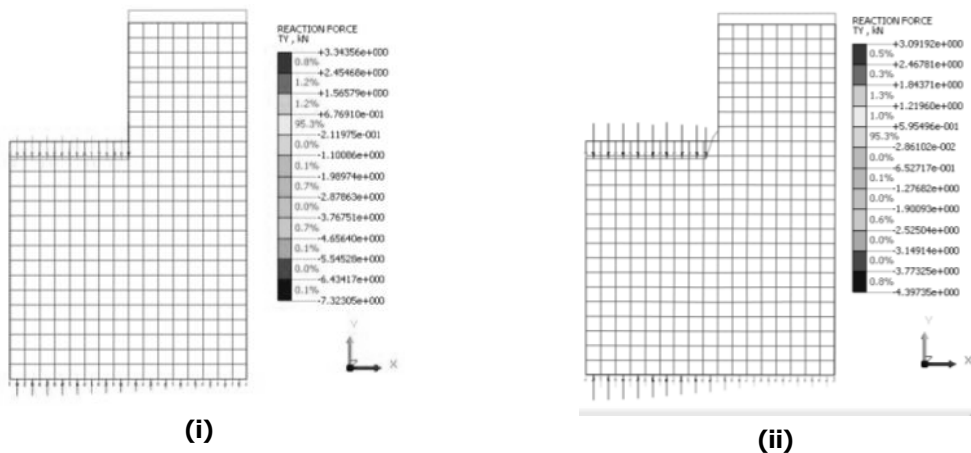

(i)

(ii)

Figure 9-4 Reaction at displacement-controlled point at last step: (i) without any treatment and (ii) corner's treatmentfor rigid buried structure in a soil mass.

The total pressure under the punch is computed by summing the vertical reactions on the displacement-controlled nodes and divided by the width of the punch. The load is then normalized by

dividing with the cohesion and the displacement is normalized by multiplying with the factor G/c.

In the analytical solution for the bearing capacity for punch problem is solved by Hill as follows:

$$\frac{q}{c} = 2 + \pi$$

Equation 9-1

where c is the cohesion of the material and 1 is the bearing capacity stress at failure.

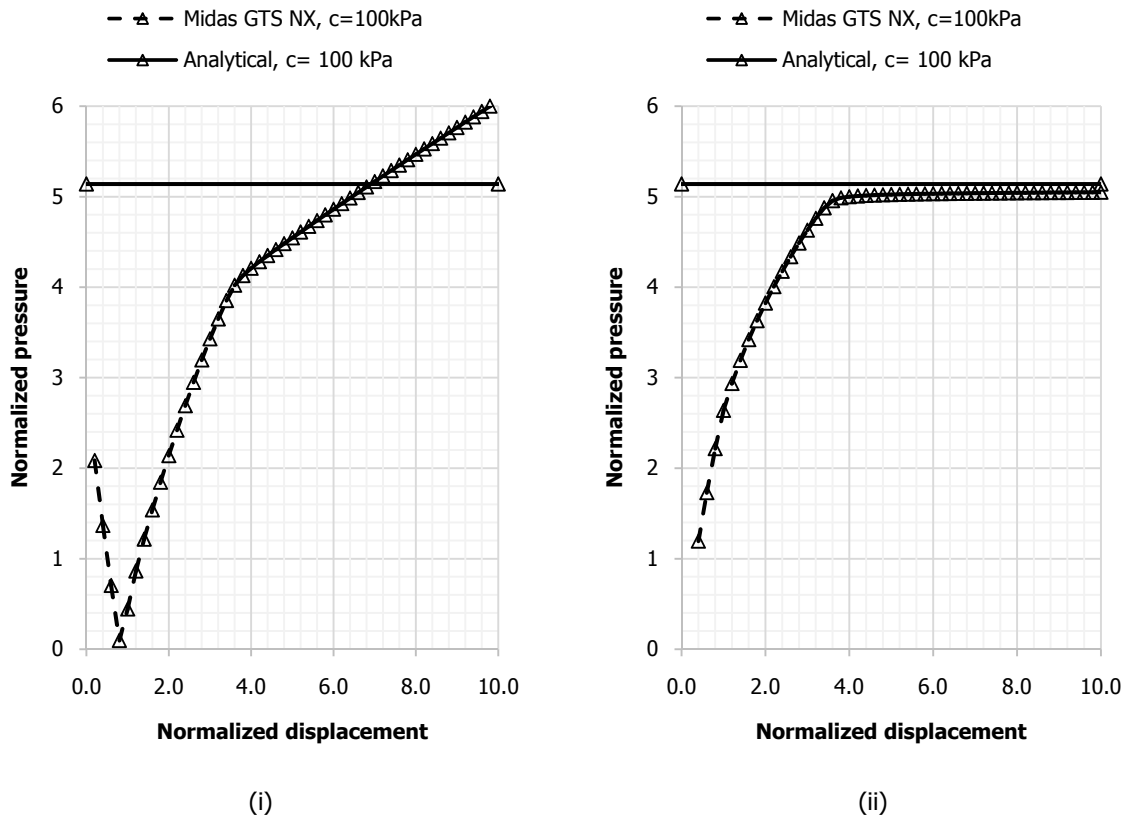In the following figures shown the result of the numerical simulations and analytical solution.

(i)   (ii)

Figure 9-5 Normalized pressure and displacement: (i) without any treatment and (ii) corner's treatmentfor rigid buried structure in a soil mass.

For Model B, the relative error of the mean bearing stress with respect to the analytical solution remains under 2 %.

Model	Analytical Mean bearing stress at collapse (kPa)	Midas GTS NX	
		Mean bearing stress at collapse (kPa)	Relative error (%)
A	5.14	n.a. (Osciallation too high)	n.a.
B	5.14	5.05	1.78

Table 9-2 Results and verification for rigid buried structure in a soil mass.